Rational Design of Electrode Architectures for Improved Performance of Li-metal and Li-ion Batteries

by

Kuan-Hung Chen

A dissertation submitted in partial fulfillment
of the requirements for the degree of
Doctor of Philosophy
(Materials Science and Engineering)
in the University of Michigan
2021

Doctoral Committee:

Associate Professor Neil P. Dasgupta, Chair
Associate Professor Jeff Sakamoto
Professor Donald J. Siegel
Professor Katsuyo Thornton

Kuan-Hung Chen

knhgchen@umich.edu

ORCID iD: 0000-0003-3879-8671

Dedication

This dissertation is dedicated to my parents, who have taught me how to love, how to enjoy little things in life, and how to always believe in myself.

Acknowledgements

First and foremost, I would like to express my sincere gratitude to my advisor, Neil. It has been a pleasure working with you over the past 5 years. You have been an excellent advisor and mentor to me, and I am glad that I had the opportunity to join your group as a master student back in 2015. Thank you for your tremendous support, guidance, and patience throughout the years on multiple exciting projects and publications. It has truly been a remarkable ride.

Second, I would like to thank my committee members for their insightful comments and suggestions throughout my doctorate study. In particular, I would like to thank Prof. Sakamoto and Prof. Thornton for being amazing collaborators over the years. It has been a huge privilege to work with you and your students. Without your expertise and insightful discussions, much of the work presented in this dissertation would not have been possible.

Third, I would like to thank all the previous and current members in the Dasgupta research group for their professional help and amazing companion throughout this long journey. I have enjoyed every discussion and brainstorming in our meetings, as well as casual chats we had inside and outside the lab. Thank you for being there for me over the years, and I will always cherish the memories and moments we spent together.

Fourth, this work would not have been possible without financial support provided by funding sources. Specifically, I would like to thank Ford Motor for funding the work in Chapter 4 under the Ford-University of Michigan alliance program. I would also like to thank the Office of Energy Efficiency and Renewable Energy at the U.S. Department of Energy for funding the work in Chapter 5 and Chapter 6 under Award Number DE-EE0008362.

Lastly, much of the data presented in this dissertation was collected using equipment at shared user facilities at the University of Michigan. These include the Michigan Center for Materials Characterization and the Battery Lab at the University of Michigan Energy Institute.

Table of Contents

List of Tables

List of Figures

Abstract

Vehicle electrification can have a significant impact on reducing greenhouse gas emissions and enabling increased use of renewable energy sources. To realize widespread adoption of electrified powertrains, a breakthrough in battery technology is needed. Particularly, improving energy density and reducing charging time are both critical for electric-vehicle-scale batteries. The primary goal of this thesis is to contribute to these metrics through the development of new fundamental understanding in lithium (Li) battery systems and designing novel electrode architectures for improved performance. This dissertation has two primary thrusts: (1) addressing the poor reversibility of Li-metal anodes in liquid electrolytes to realize next-generation batteries with high energy densities, and (2) enabling fast-charging of state-of-the-art Li-ion batteries with thick electrodes.

In Thrust 1, an improved mechanistic understanding of the morphological evolution of Li metal anodes during cycling is developed, which provides insight into the voltage, capacity, and failure of Li-metal batteries. It is shown that mass transport limitations arise as a result of dead Li accumulation at the Li metal electrode, which introduces a tortuous pathway for Li-ion transport. In Li-Li symmetric cells, mass transport effects cause a change in the voltage shape and an increase in cell polarization. The accumulation of dead Li is also conclusively shown to directly cause capacity fade of full cells containing Li metal anodes. In order to reduce dead Li formation, a three-dimensional (3-D) current collector composed of highly uniform vertically aligned Cu pillars is further developed. By rationally tuning geometric parameters of the 3-D architecture, the Li morphology can be controlled. In addition, deposition of an ultrathin layer of zinc oxide by atomic layer deposition on the current collector surface can facilitate initial Li nucleation, which dictates the morphology and reversibility of subsequent Li growth. This core-shell pillar architecture allows the effects of geometry and surface chemistry to be individually controlled to optimize the electrode performance in a synergistic manner. Using this platform, Li metal anodes are demonstrated with Coulombic efficiency up to 99.5%.

In Thrust 2, two approaches are demonstrated to improve the charge rate of Li-ion batteries with thick electrodes. In the first approach, a laser-patterning process is developed to produce 3-D graphite architectures with arrays of vertical pore channels through the electrode thickness, which enhance both through-plane and in-plane ionic transport. By applying the 3-D electrode design on industrially relevant pouch cells, it is shown that long-term fast-charge cycling (< 15 minute charging time) can be achieved with minimal capacity fade. The second approach addresses energy/power tradeoffs by fabricating hybrid anodes with uniform mixtures of graphite and hard carbon. By controlling the graphite/hard carbon ratio, it is shown that battery performance can be systematically tuned to achieve both high energy density and efficient fast charging. A detailed electrochemical analysis demonstrates that the enhanced performance is attributed to an improved homogeneity in reaction current distribution throughout the hybrid anode volume.

In summary, this thesis furthered the understanding and performance of Li-metal and Li-ion batteries through the development of new fundamental insight and novel electrode architectures. The implications of this work could aid in the development of not only the state-of-the-art Li-ion batteries, but also next-generation battery systems using Li metal anodes.

Chapter 1

Introduction

1.1 Motivation and Outline

Fossil fuels, such as coal, petroleum, and natural gas, have energized modern human civilizations and played a dominant role in global energy production and consumption. Although burning fossil fuels produces a huge amount of energy for humans, these resources are finite and not sustainable. Fossil fuel combustion generates excessive amounts of carbon dioxide (CO_2) and other greenhouse gases that have contributed to the observed global warming and climate change over the past few decades. Therefore, there is an urgent need to transition away from using fossil fuels and adopt renewable sources of energy.[1]

Figure 1.1 shows the United States (U.S.) annual energy consumption by energy source and use sector in 2019.[2] Three important messages can be drawn from the figure: (1) 80% of the total energy consumption comes from burning fossil fuels, with petroleum, natural gas, and coal accounting for 37%, 32%, and 11%, respectively. In contrast, renewable energy sources are used for only 11% of the overall energy consumption. (2) 37% of total U.S. energy consumption is used for transportation. Within the transportation sector, fossil fuels account for 94% of energy use. In contrast, renewable energy sources contribute 5%. (3) 56% of the consumed renewable energy is used to produce electricity for the electric power sector. However, the produced electricity provides less than 1% of the transportation sector's energy consumption.

It can therefore be inferred from these energy data that electrification of the transportation sector could have a significant impact on enabling more usage of renewable energy sources and reducing global greenhouse gas emissions.[3–5]

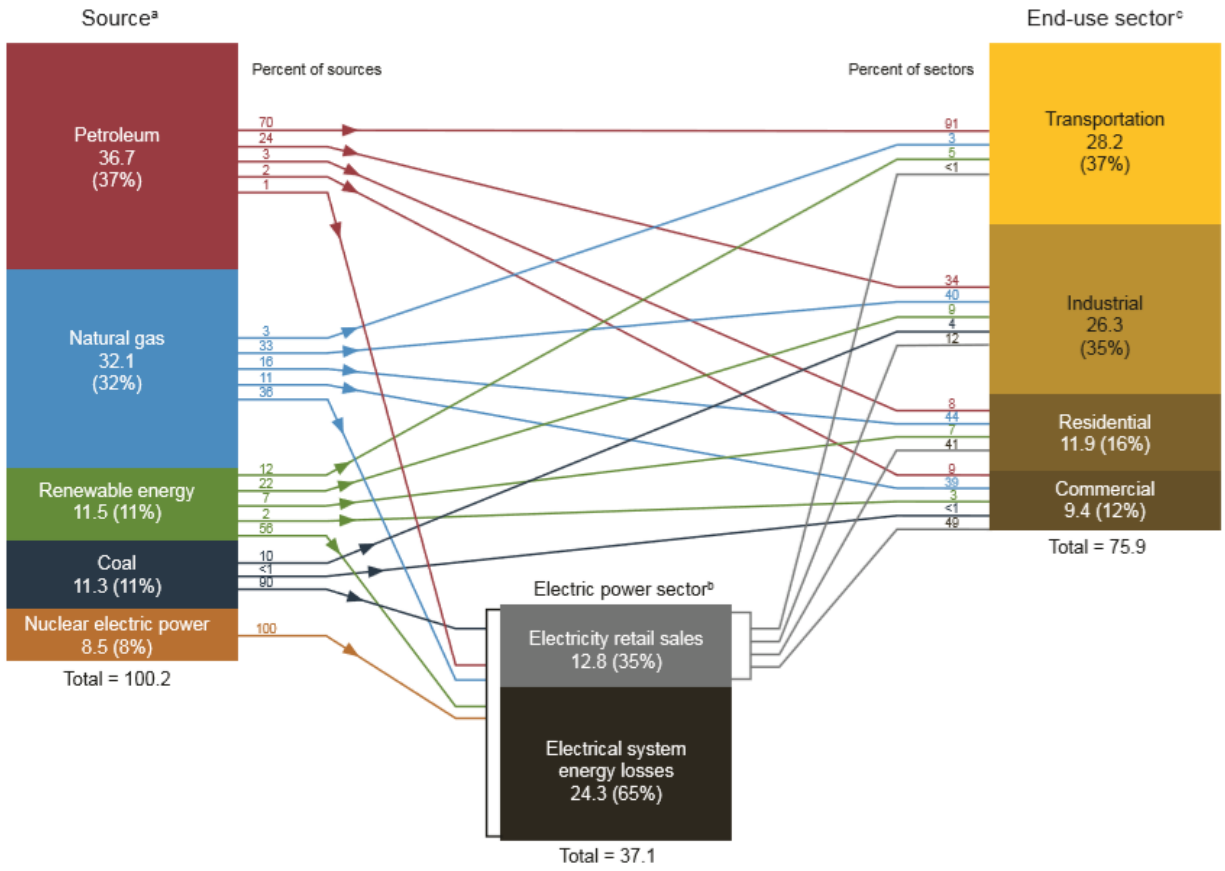

Figure 1.1. U.S. energy consumption chart in 2019 showing the types and amount of primary energy sources consumed (left), the amount of primary energy used by the electric power sector (bottom) and end-use sectors (right), and the amount of produced electricity used by the end-use sectors (bottom).[2]

To enable widespread adoption of electrified powertrains, the U.S. Department of Energy (DOE) has identified that a breakthrough in battery technology is needed.[6] In addition, the U.S. Advanced Battery Consortium (USABC) goals for electric vehicle (EV) batteries by 2023 are to reduce the cost of batteries to $75/kWh, increase energy density to 275 Wh/kg, and enable fast charging with less than 15-minute charging time.[7] The overarching goal of this thesis is to contribute to these targeted metrics through the development of new fundamental understandings in battery systems, and further applying this gained knowledge to design novel electrode architectures for improved cell performances.

Chapter 2 will first provide background knowledge on the basics of state-of-the-art lithium-ion batteries, advantages/disadvantages of using lithium (Li) metal electrodes, and challenges

associated with fast charging of Li-ion batteries. These concepts will then be used throughout the remainder of the thesis.

Chapters 3 and 4 explore next-generation Li metal batteries using Li metal anodes in liquid electrolytes to enable high energy densities. Chapter 3 provides mechanistic insight into the impact of the morphological evolution of Li metal anodes on battery voltage, capacity, and failure. Chapter 4 builds upon this improved understanding of Li metal anodes to rationally design three-dimensional (3-D) electrode architectures to achieve a desirable Li morphology during cycling and enhance the overall performance.

Chapters 5 and 6 focus on enabling fast charging of Li-ion batteries. It will be demonstrated that the challenges associated with fast charging of graphite anodes share similarities with the Li plating/stripping processes in Li-metal batteries. The insights and lessons gained from Chapter 3 and 4 will be applied to address poor performances and energy/power tradeoffs. Specifically, Chapter 5 describes the engineering of aligned macro-porosity in electrodes to achieve efficient fast charging. Chapter 6 will detail the design and development of hybrid electrodes to overcome energy/power density tradeoffs of Li-ion batteries.

Chapter 7 concludes the thesis by summarizing the main contributions of this work to the battery community, and presenting opportunities for future work to build upon the findings presented in this thesis.

1.2 Individual and Group Research Statement

The research work in this dissertation represents the efforts of not only myself but also all my collaborators and co-authors. A brief summary of contributions to the presented work is shown below.

Chapter 3 was adapted from Chen, et al. 2017.[8] Kuan-Hung Chen prepared all the samples, performed the electrochemical measurements, and analyzed the results. Kevin N. Wood assisted with the data analysis and manuscript writing. Eric Kazyak helped collect and process the *operando* video microscopy data. William S. LePage performed the scanning electron microscopy (SEM) imaging. Andrew L. Davis and Adrian J. Sanchez performed the COMSOL electrochemical modeling. Neil P. Dasgupta supervised the research and assisted with writing the manuscript and provided insights and guidance.

Chapter 4 was adapted from Chen, et al. 2019.[9] Kuan-Hung Chen developed the templated electrodeposition process for 3-D copper (Cu) current collector fabrication, performed electrochemical measurements, and analyzed the results. Adrian J. Sanchez performed the mechanical modeling for this work and designed and built the experimental setup for fabricating 3-D current collectors. Eric Kazyak performed the X-ray photoelectron spectroscopy (XPS) analysis and assisted with developing the zinc oxide (ZnO) atomic layer deposition (ALD) process. Andrew L. Davis built the sessile drop testing setup for molten Li and performed the associated measurements. Neil P. Dasgupta supervised the research and assisted with writing the manuscript and provided insights and guidance.

Chapter 5 was adapted from Chen, et al. 2020.[10] Kuan-Hung Chen and Min Ji Namkoong fabricated the electrodes and pouch cells used in this work. Kuan-Hung Chen performed material characterizations and analyzed the electrochemical results. Vishwas Goel, Saeed Kazemiabnavi, S. M. Mortuza, and Katsuyo Thornton developed and performed the continuum-scale modeling in this study. Vishwas Goel and Katsuyo Thornton participated in the manuscript writing process and provided insights and support. Chenglin Yang designed and built the laser processing setup for fabricating 3-D electrodes and prepared the patterned samples. Eric Kazyak assisted with the pouch cell fabrication and performed the 3-D optical microscopy imaging. Neil P. Dasgupta, Jeff Sakamoto, Katsuyo Thornton, and Jyoti Mazumder supervised the research, and assisted with writing the manuscript and provided insights and guidance.

For the work presented in Chapter 6, Kuan-Hung Chen performed all of the electrochemical measurements and associated data analysis. Vishwas Goel and Katsuyo Thornton developed and conducted the electrochemical modeling in this study and assisted with the manuscript writing. Min Ji Namkoong provided assistance throughout the electrode and pouch cell fabrication process. Simon Müller performed the synchrotron X-ray tomography measurements and worked with Markus Wied on the tomography data analysis. Neil P. Dasgupta, Jeff Sakamoto, Katsuyo Thornton, and Vanessa Wood supervised the research, and assisted with writing the manuscript and provided insights and guidance.

Chapter 2

Background

In 2019, the Nobel Prize in Chemistry was awarded for the development of Li-ion batteries.[11] John B. Goodenough, M. Stanley Whittingham, and Akira Yoshino, three of the scientists who made major pioneering work back in 1970s and 1980s, were awarded the Nobel Prize. Rechargeable Li-ion batteries have revolutionized our daily lives since they first entered the market in 1991. They have laid the foundation for portable consumer electronics, including mobile phones, laptops, cameras, etc. Years of research efforts have significantly improved the performance and reduced the cost of Li-ion batteries, making them the predominant technology-of-choice for the rechargeable battery market.[12] Ongoing scientific advances in Li-ion batteries and beyond Li-ion chemistry will continue to have substantial impacts on the human society. Before delving into more details, this background chapter will describe important concepts to understand the work to follow.

2.1 Basics of Li-ion Batteries

2.1.1 Principles of operation

Li-ion batteries are electrochemical devices that can convert chemical energy directly into electrical energy. A conventional Li-ion battery consists of three main components: an anode (negative electrode), a cathode (positive electrode), and an electrolyte. Both the anode and cathode are composed of particles of materials that are capable of hosting Li ions in their structures, thereby storing electricity in the form of chemical energy. A porous separator is placed in between the anode and cathode to keep the two electrodes apart, in order to avoid shorting. The entire cell is then flooded with a liquid electrolyte that infiltrates into the pore space within the electrodes and

the separator. The liquid electrolyte conducts ions, but does not conduct electrons. Therefore, it serves as the medium through which Li ions can travel between the anode and cathode.

During discharge, the voltage difference between the cathode and anode spontaneously drives Li ions to leave the anode particles, travel through the liquid electrolyte, and enter into the cathode particles (**Figure 2.1**). Since the electrolyte is an electrical insulator, electrons are forced to pass through an external circuit, generating a current that allows us to harness electrical energy.

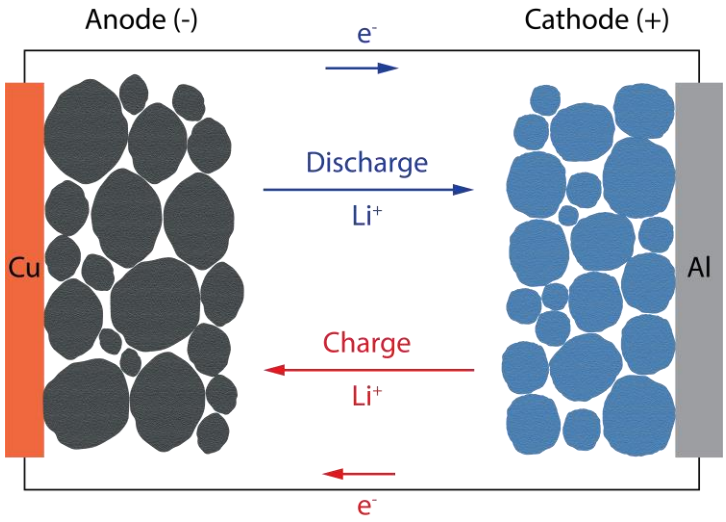

Figure 2.1. Schematic showing the movement of Li ions and electrons during charge/discharge of a Li-ion battery.

One of the key features of Li-ion batteries is their rechargeability. This is enabled by the development of electrode materials that can not only host Li ions inside of their crystallographic structure, but also allow Li ions to move into and out of the structures relatively quickly and reversibly. During the charging process, an external voltage is applied to the battery in order to drive the reactions in the opposite direction of that which occurred spontaneously during discharge. In this scenario, Li ions leave the cathode particles, pass through the electrolyte/separator, and enter into the anode particles (**Figure 2.1**).

The definitions of anode/cathode and negative/positive electrodes are different. Anode refers to the electrode where oxidation is taking place (electrons flow out), and cathode refers to the electrode where reduction is taking place (electrons flow in). On the other hand, the electrode with the higher potential is referred to as positive, and the electrode with the lower potential is referred to as negative. For a galvanic cell (a cell that produces electricity, such as batteries during

discharge), the anode is the negative electrode and the cathode is the positive electrode. During the charging process, however, batteries become an electrolytic cell (a cell that consumes electricity). Therefore, strictly speaking, the negative electrode becomes the cathode and the positive electrode becomes the anode during charge. However, to avoid the need for constantly switching terms during charge/discharge, the convention of the Li-ion battery community is to name the negative electrode as the anode and the positive electrode as the cathode, regardless of charging/discharging processes.

2.1.2 Key equations

The open-circuit voltage (V_{oc}) of a battery is determined by the difference in chemical potential between the cathode and the anode:

$$V_{oc} = -\frac{(\mu_i^+ - \mu_i^-)}{z_i F} \tag{1}$$

where μ_i^+ and μ_i^- are the chemical potentials of species *i* in the positive and negative electrodes, respectively, F is Faraday's constant, and z_i is the charge number of species *i*.

The chemical potential (μ_i) is defined as the change in the Gibbs free energy (G) of the system when an infinitesimal quantity of species *i* is added (while temperature and pressure are held constant):

$$\mu_i = \left(\frac{\partial G}{\partial N_i}\right)_{T,P} \tag{2}$$

The chemical potential of species *i* can further be expressed in relation to its standard-state chemical potential (μ_i^0) and activity (a_i):

$$\mu_i = \mu_i^0 + RT ln a_i \tag{3}$$

where *R* is the gas constant and *T* is the absolute temperature.

Combining Equations (1)-(3), the open-circuit voltage can thus be expressed as the following, which is known as the Nernst equation:

$$V_{oc} = \frac{-RT}{z_i F} ln \frac{a_i^+}{a_i^+} \tag{4}$$

The Nernst equation determines the open-circuit voltage of an electrochemical system when it is in thermodynamic equilibrium (zero current). However, any useful electrochemical system needs to operate at a non-zero current, thus deviating from open-circuit voltage conditions.

This voltage deviation includes both kinetics and transport losses, which represent voltage/energy penalties that need to be paid in order to drive a finite current.

For reaction kinetics, the Butler-Volmer equation can be used to describe the relationship between applied current and voltage loss under non-equilibrium conditions:

$$O + ne^{-} \rightleftarrows R \tag{5}$$

$$j = j_o \left[\frac{C_O}{C_O^*} exp\left(\frac{(1-\alpha)nF\eta}{RT} \right) - \frac{C_R}{C_R^*} exp\left(-\frac{\alpha nF\eta}{RT} \right) \right] \tag{6}$$

where j is current density, j_o is the exchange current density, C_O is the concentration of species O, C_O^* is the bulk concentration of species O, α is the symmetry factor, n is the number of electrons transferred in the electrochemical reaction, η is the voltage loss (overpotential), C_R is the concentration of species R, and C_R^* is the bulk concentration of species R.

Transport losses in batteries are mainly due to the transport of ions through the electrolyte by conduction and diffusion, which create gradients in electric potential and concentration, respectively. In one dimension, this is described by the Nernst-Planck equation:

$$J_i(x) = -D_i \frac{\partial c_i(x)}{\partial x} - \frac{z_i F}{RT} D_i c_i \frac{\partial \phi(x)}{\partial x} \tag{7}$$

where J_i is the mass flux of species i, x is the position, D_i is the diffusion coefficient of species i, c_i is the concentration of species i, and ϕ is the electrostatic potential.

It is noted that voltage losses associated with kinetics and transport are often coupled. For example, during charge/discharge of a battery, concentration gradients of ions are formed as a result of mass transport (Equation 7). These concentration gradients can further affect reaction kinetics as the concentration of reactants and products change at the electrode/electrolyte interface (C_O and C_R in Equation 6).

2.1.3 Electrodes

Electrode material development is one of the major breakthroughs that have enabled rechargeable Li-ion batteries. Specific capacity, voltage, and reversibility are three important criteria when it comes to the material selection. In addition, since both anodes and cathodes act as conductors for both Li ions and electrons during charge/discharge, electrode materials should be mixed conductors, meaning they can conduct both ions and electrons.

2.1.3.1 Anodes

Among various anode materials, graphite has been predominantly used in state-of-the-art Li-ion batteries due to its stable electrochemical performance and relatively high specific capacity.[13] Specific capacity, or the amount of charge that can be stored in the electrode per mass, is typically determined by the number of available structural sites that can host Li ions during cycling. Graphite has a layered crystallographic structure that allows for intercalation of Li ions between the graphene planes, forming graphite intercalation compounds.[14,15] At the fully charged state, six carbon atoms can host one Li ion, forming LiC_6.[16] This gives graphite a theoretical specific capacity of 372 mAh/g.[13]

In addition to its relatively high specific capacity, graphite displays well-defined voltage plateaus at low potentials (< 0.2 V vs. Li/Li^+) during charge/discharge. Low anode potentials are preferred because the full cell voltage can be maximized when the graphite anode is coupled with a cathode. Furthermore, graphite also exhibits high efficiency values during cycling due to low volumetric expansion upon Li intercalation and the formation of stable electrode/electrolyte interphase in carbonate liquid electrolytes (discussed further below).

The high specific capacity, low voltage, and high reversibility have therefore make graphite an attractive material to achieve high-performing Li-ion batteries. As a result, graphite anodes have been commercialized since the beginning of Li-ion industry and continue to play a critical role in EV battery technology.[17–19]

2.1.3.2 Cathodes

One of the most common state-of-the-art cathode materials is $Li(Ni_{1-x-y}Mn_xCo_y)O_2$ (also known as NMC), which has a layered transition metal oxide structure. NMC-based cathodes have been widely used in EV batteries owing to their desirable balance between specific capacity, voltage, and cost. Increasing nickel content in the NMC structure has been shown to increase specific capacity but reduce stability.[20] Adding manganese has the benefit of achieving lower internal resistance but reduces capacity.[20,21] Increasing cobalt content leads to an improved structural stability and high conductivity, but increases costs.[22] Therefore, tuning the ratio between these three metal elements in NMC materials can complement each other's merits. Particularly, $LiNi_{1/3}Mn_{1/3}Co_{1/3}O_2$ (NMC-111) and $LiNi_{0.5}Mn_{0.3}Co_{0.2}O_2$ (NMC-532) are two successful combinations of NMC that have been widely used in the battery market.[5,23,24]

Recently, there have been increasing research efforts focusing on minimizing the cobalt content (cobalt-free) and maximizing the nickel content in NMC to achieve low-cost and high-energy-density cathodes. However, these new materials can suffer from stability issues, and thus require further optimization before mass market penetration.

2.1.4 Electrolytes

The state-of-the-art liquid electrolytes for Li-ion batteries mainly consist of lithium hexafluorophosphate ($LiPF_6$) dissolved in the mixture of ethylene carbonate (EC) and linear carbonates selected from the group of dimethyl carbonate (DMC), diethyl carbonate (DEC), and ethyl methyl carbonate (EMC).[13,25] This family of compounds are commonly referred to as carbonate electrolytes.

One advantage of this salt/solvent combination is its wide electrolyte stability window, which is defined as the potential range within which the electrolyte species are thermodynamically stable and are neither reduced nor oxidized by the low and high potentials of the anode and cathode.[26] Carbonate electrolytes generally have a stability window of ~1.5-4.5 V vs. Li/Li^+.[13,25,27] This is advantageous as the state-of-the-art NMC cathodes are typically operated between 3.0-4.3 V in order to achieve both high energy and power output.[28]

However, the graphite anode potential reaches < 0.2 V during cycling of Li-ion batteries, which is below the thermodynamic stability window of the carbonate electrolyte. Under this circumstance, the organic solvents and Li salts can easily be reduced. Fortunately, during the initial lithiation of graphite anodes, carbonate electrolytes undergo chemical decomposition and form a thin passivation layer on the graphite surface, which can prevent further irreversible and parasitic reactions in the following cycles, while still supporting reversible Li intercalation/deintercalation in/out of the graphite structure.[29] This passivation layer is widely known as solid electrolyte interphase, or SEI, in the battery community. The SEI is a complex composite interphase that contains several different phases, whose composition depend on the electrolyte formulation.[29,30] Today's Li-ion battery electrolytes are highly optimized and consist of various additives to facilitate the formation of highly stable SEI during the first cycle, which in turn allows for long-term cycling of the batteries.[31]

2.1.5 Practical considerations

In order to maximize the electrochemically-active surface area and provide a well-balanced ionic and electronic conductivity throughout the electrodes during cycling, today's Li-ion battery electrodes are particle-based laminates.[32,33] These laminates are fabricated by first mixing active electrode materials with conductive additives and polymer binders in a solvent to make a homogeneous slurry. The slurry is then casted onto a foil current collector (typically copper for anodes and aluminum for cathodes) and is subsequently dried.[33] After casting and drying, the electrodes are roll-pressed (calendered) down to a desired porosity.[32]

It is worth noting that the electrode manufacturing process has benefitted from substantial knowledge from the prior magnetic tape industry, including both upstream steps (mixing, casting, and calendering) and downstream processes (slitting, rewinding, and packaging).[34] In fact, the successful commercialization of Li-ion batteries by Sony was made possible by bringing together technologies in both their magnetic tape and battery divisions.[19]

During charge/discharge, ions are transported inside the battery by permeating through the pore space in the porous electrodes and separator within the liquid electrolyte. In the context of porous electrodes and separators used in Li-ion batteries, the concept of tortuosity factor (τ) is often used as an geometric parameter for measuring transport properties, which is defined as the change in diffusion path length.[35] $\tau = 1$ corresponds to the absence of any barrier, and the diffusion pathway is parallel to the transport direction. On the other hand, $\tau > 1$ is representative of tortuous diffusion pathways through porous microstructures, such as electrodes and separators.[35–38] The effective diffusion coefficient of Li ions within porous microstructures can be described as:

$$D_{eff} = D_i \frac{\epsilon}{\tau} \tag{8}$$

where D_{eff} is the effective diffusion coefficient, D_i is the intrinsic diffusion coefficient, ϵ is the porosity, and τ is the tortuosity factor. To minimize transport limitations and accelerate Li-ion diffusion, lower tortuosity and shorter diffusion path lengths are preferred.

In addition to Li-ion diffusion in the liquid-phase electrolyte, the rate performance of Li-ion batteries is also affected by the diffusion coefficient of Li inside the solid-phase active material particles. A limited solid-state diffusivity will result in a particle-scale concentration gradient (ex. during lithiation the Li concentration at the particle edge can be higher than the particle interior).

This particle-scale concentration gradient will further cause increasing cell polarization in addition to the electrode-scale concentration gradient.

2.2 Li metal batteries

2.2.1 Motivations

While Li-ion batteries have been the most popular choice for portable electronics over the past few decades, their limited energy density has been an impediment towards long-range EV applications. One of the main reasons is that while graphite is a stable Li-hosting material, the majority of the mass in fully lithiated graphite (LiC_6) is associated with the host material (carbon) rather than the guest Li ions that contribute to the capacity and energy. Hence, the specific capacity of graphite anodes is limited to 372 mAh/g.

One strategy to improve the energy density of current Li-ion batteries is to replace the graphite anode with a Li metal anode. Li metal has been widely regarded as an ideal anode material because of its highly negative electrochemical potential and high theoretical specific capacity (3,860 mAh/g), which is 10 times greater than graphite. Thus, improving Li metal anode performance is widely viewed as a key bottleneck to enable next-generation battery systems beyond Li-ion.[39–41]

2.2.2 Challenges of Li metal anodes

Unfortunately, several disadvantages of Li metal anodes have restricted their development and commercialization to this date. These drawbacks include low Coulombic efficiency, poor cycle life, and safety concerns, which can ultimately be attributed to the high reactivity of Li metal and undesirable electrode/electrolyte interactions, resulting in a threefold effect.

2.2.2.1 Electrolyte decomposition

Due to their highly negative potential (-3.04 V vs. standard hydrogen electrode), charging and discharging of Li metal anodes occurs at a potential range that is outside of the electrochemical stability window for most of the commonly used liquid organic electrolytes. The immersion of Li metal into liquid electrolytes instantaneously results in SEI growth at the electrode/electrolyte interface, consuming both Li inventory and electrolyte species. In addition, unlike the kinetically-

stable SEI that can be formed on the surface of graphite during the first cycle, the SEI growth on Li metal surfaces proceeds continuously in a non-passivating manner, resulting in the formation of thick surface layers.[42,43] The uncontrolled SEI growth and electrolyte decomposition during cycling can therefore cause a dramatic increase in internal resistance and drying-up of the cell.[44–46]

2.2.2.2 Dendrite nucleation and growth

The uncontrolled SEI growth on the surface of Li metal has also been hypothesized to create inhomogeneities along the electrode surface, resulting in localized "hot spots" where Li preferentially nucleates during electrodeposition.[46,47] The localized nucleation leads to the formation of Li dendrites, which have a highly branching structure with high surface areas. Li dendrites can potentially cause internal short circuiting, possessing serious safety concerns.[48–50] In addition, dendrite growth results in dramatic volumetric changes of Li metal anodes and cause fractures in the SEI, leading to the creation of more hot spots, thereby exacerbating the problem.[43]

It is noted that dendrites of various morphologies (needle-like, mossy-like, or fractal-like) can grow under different cycling conditions.[43] Needle-like dendrites have a tendency to occur at low current densities (< 0.5 mA/cm^2 in carbonate electrolytes).[51] Mossy-like dendrites (or mossy Li) have been shown to grow at practical current densities (> 0.5 mA/cm^2 in carbonate electrolytes) and thus are the most commonly observed dendrite morphology in Li-metal batteries (**Figure 2.2**).[42,47] Fractal-like dendrites can grow under aggressive conditions where Li-ion concentration at the electrode/electrolyte interface reaches zero.[52]

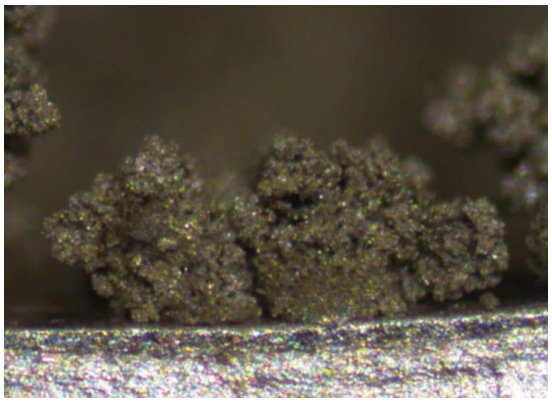

Figure 2.2. Cross-sectional optical microscope image showing the growth of mossy Li structures on a Li metal anode surface.[8]

2.2.2.3 Dead Li formation

During the electrodissolution process where Li is stripped from dendrites, large volumetric changes can cause the mossy Li structure to become physically detached from the bulk Li surface via fractures or mechanical failures. Li at the base of the dendrites can also be removed during the stripping process, leaving the rest of the structure electrically isolated by the insulating SEI. [42,53,54] Both of these inactive structures are referred to as "dead Li", which results in low Coulombic efficiency and depletion of the Li inventory, thereby preventing long-term cycling of Li metal anodes (**Figure 2.3**).[51,55–58]

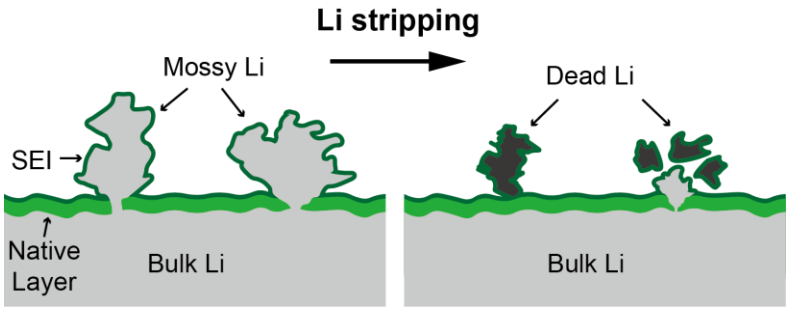

Figure 2.3. Schematic showing the formation of dead Li during Li electrodissolution, where Li is stripped from the mossy Li.

2.2.3 Addressing the root causes of poor Li metal reversibility

Many recent research efforts have focused on modifying the Li metal electrode, electrolyte, and electrode/electrolyte interface to mitigate the symptoms of the poor behaviors. These efforts include re-designing the electrolyte system to achieved desired Li plating/stripping morphology[59–62], applying surface coatings to suppress the nucleation/growth of dendrites[63–68], synthesizing 3-D scaffold materials to accommodate uncontrolled volumetric changes[9,69–73], etc.

In the literature, Li-Li symmetric cells have been widely used as a platform for evaluation of Li metal performance without the need to decouple cathode effects. Voltage vs. time profiles during galvanostatic cycling of Li-Li cells are widely reported, and changes in the voltage shape and magnitude have often been qualitatively related to electrode stability and failure.[74–77] These voltage variations depend strongly on current density, depth of discharge, electrolyte composition,

and other variables, yet their origins have often been overlooked. This can be attributed to a lack of fundamental insight into the dynamic evolution of Li metal anodes during cycling, which has also restricted research strategies aimed at addressing these problems. Thus, a more comprehensive understanding of how Li metal anodes dynamically evolve during cycling, and how this evolution leads to cell failure, is essential.

To address these limitations, our previous study provided a detailed framework of how Li metal anodes evolve during initial cycling.[42] A custom-designed visualization cell was developed to enable *operando* synchronized observations of Li metal morphology change and voltage behavior during cycling (**Figure 2.4**).[42]

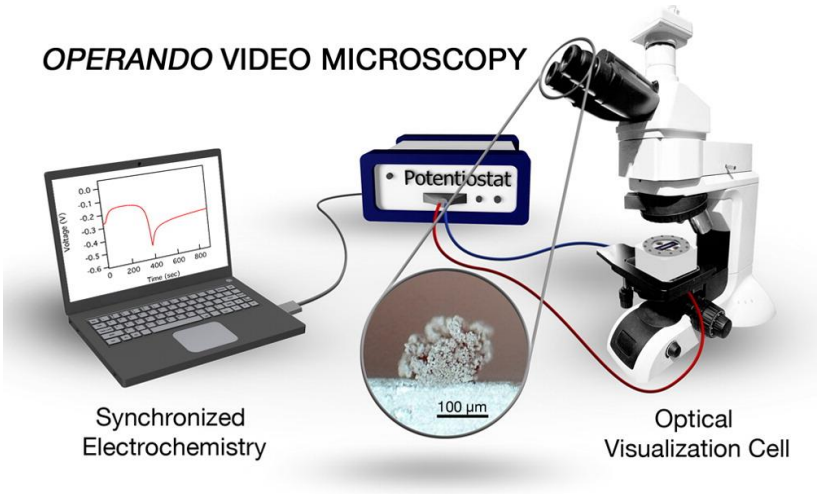

Figure 2.4. Schematic of the *operando* video microscopy setup.[42]

Through the use of *operando* optical microscopy, the morphological evolution of the electrode surface can be directly correlated to changes in cell polarization, as shown in **Figure 2.5**.[42] During the initial Li-plating half-cycle, inhomogeneous dendrite nucleation occurs on the Li metal anode surface. As mossy Li grows, the voltage response exhibits a characteristic voltage decay (**Figure 2.5a-b**), which is associated with the dramatic increase in surface area of the dendrites, and faster reaction kinetics of the freshly plated Li than the bulk surface. As a result of the faster reaction rate, subsequent Li deposition also preferentially occurs on existing dendrites rather than nucleation new dendrites.

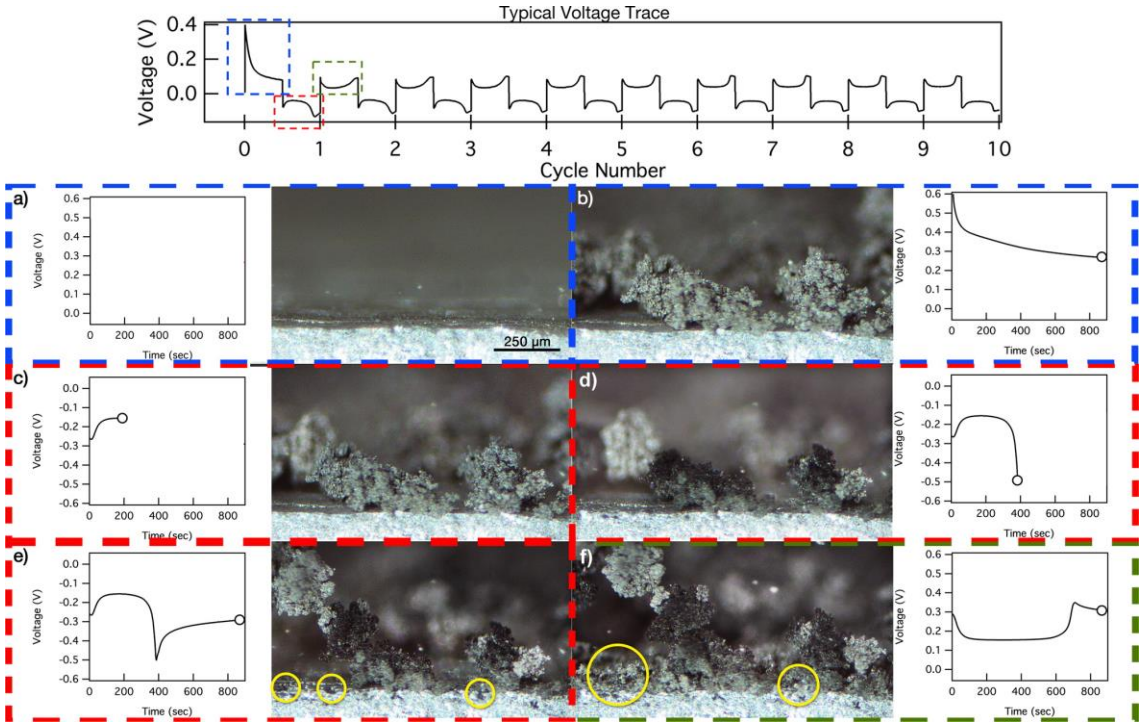

Figure 2.5. Still frames of an *operando* visualization cell (Li-Li symmetric cell) cycled at 5 mA/cm^2 showing both the electrode morphology and corresponding voltage trace at different points during initial cycling.[42]

Upon switching polarity (Li stripping), the dominant reaction pathway is the kinetically fast dissolution of mossy Li (**Figure 2.5c**). As the amount of active Li within the mossy Li approaches zero, a characteristic increase in cell polarization appears, which can be attributed a transition to kinetically slower dissolution from the bulk Li surface (**Figure 2.5d**). Further stripping from the bulk Li leads to the formation of surface pits. As the surface layers are fractured during the pitting process, new kinetically faster reaction pathways are formed. As Li stripping progresses, the surface area associated with pits continues to increase, resulting in decreasing cell polarization (**Figure 2.5e**).

Therefore, the formation of dendrites and surface pits during cycling of Li metal electrodes can be associated with transitions between kinetically fast and slow interfacial reactions (**Figure 2.6a**), which are spatially varying along the electrode surface.[42] The spatially varying kinetics thus dictate changes in voltage traces, resulting in a "peaking" shape in the voltage response of Li-Li symmetric cells (**Figure 2.5**). The initial portion of the voltage trace is dominated by the cathode (the electrode which Li plating occurs), as a transition occurs from dendrite nucleation to growth

(**Figure 2.6b**). After the minimum cell polarization is reached, the kinetics at the anode (the electrode which Li stripping occurs) begin to dominate the voltage trace, as the surface area of the kinetically fast dendrites decreases during Li stripping. This leads to a transition in reaction pathways from stripping from dendrites to stripping from the bulk surface, causing a cell polarization maximum (**Figure 2.6b**). Subsequently, the decrease in cell polarization is driven by increasing surface area of both pits at the anode and dendrites at the cathode.

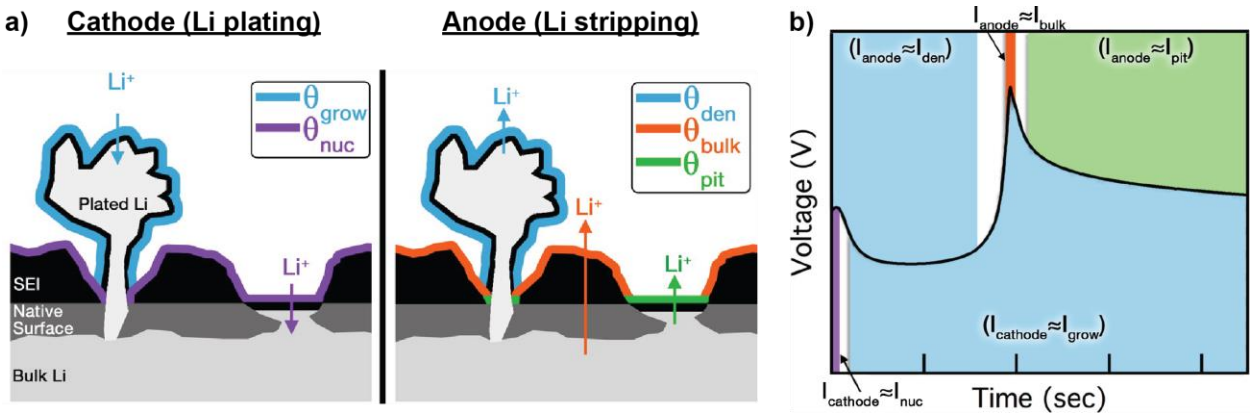

Figure 2.6. (a) Schematic showing the regions associated with the area fraction of each reaction pathway during Li plating (cathode) and stripping (anode). (b) The peaking voltage trace with shaded regions indicate dominant reaction pathways at the anode (above profile) and cathode (below profile).[42]

Analysis of voltage changes during initial cycling has provided insight into the dynamic morphological changes occurring inside of the cell, where we are typically "blind" to electrode dynamics.[42] Chapter 3 will build upon this understanding and explore the morphology evolution of Li metal electrodes during extended cycling, and its impact on cell performance. It will be shown that the accumulation of dead Li over long-term cycling plays a critical role in determining the cell voltage, capacity, and eventual failure. Chapter 4 will further apply the mechanistic understanding gained in Chapter 3 to design 3-D microstructures and interfacial chemistry that reduce dead Li formation/accumulation, thereby improving the cycling efficiency and lifetime of Li metal anodes.

2.3 Fast-charging of Li-ion batteries

2.3.1 Motivation

To accelerate the widespread adoption of EVs, increasing battery charging rates is important, in addition to improving energy densities.[17,78–80] In particular, enabling fast-charging Li-ion batteries without significantly impacting energy density, compromising safety, or increasing cost is believed to be an important factor needed to accelerate public acceptance of EVs by reducing range anxiety.[78,81,82] To address these technological challenges, the U.S. DOE has identified performance targets to realize batteries with > 180 Wh/kg specific energy within a 10-min charge time and demonstrate < 20% capacity fade over 500 cycles. In addition, the USABC goal for fast-charging EV batteries by 2023 is to charge 80% of the total cell capacity within a 15-min charge.[7]

Over the past decade, the major push for Li-ion batteries has been to maximize energy density. The most common approach to increase energy density while using state-of-the-art electrode materials (graphite anodes and Li-metal-oxide cathodes) is to use thicker electrodes with high mass loadings and low porosity, which increases the areal charge capacity. By doing so, the excess weight and volume associated with inactive components, such as current collectors, separators, and packaging materials, can be minimized.[83–86] Therefore, enabling fast-charging high-loading (> 3 mAh/cm^2) and dense electrodes is critical and relevant to the state-of-the-art batteries compared to low-loading and/or uncalendered electrodes.[87]

2.3.2 Energy/power density tradeoffs

Unfortunately, the adoption of thick electrodes intrinsically leads to a tradeoff between energy density and power performance. **Figure 2.7** shows a schematic of the typical electrode fabrication process. After casting, drying, and calendering, active material particles are densely packed, creating tortuous diffusion pathway for Li-ion transport. These mass transport limitations are further exacerbated with increasing electrode loading/thickness. As a consequence, significant concentration gradients develop through the electrode thickness, which result in a large cell polarization and significantly reduce the accessible capacity of the electrodes under fast-charge conditions.[79,83,84,88,89] In addition to ionic transport limitations in the liquid electrolyte phase, other physiochemical processes, including reaction and transport kinetics at the electrode/electrolyte

interface and solid-state Li diffusion in solid-phase particles, can also contribute to high cell polarization during fast charging.[90–92]

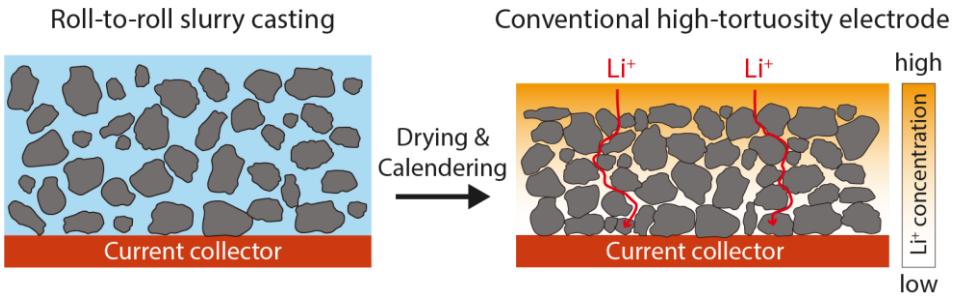

Figure 2.7. Schematic illustration of the electrode fabrication process showing slurry casting and calendered conventional high-tortuosity electrodes.[10]

2.3.3 Li plating during fast charging

Another major concern of fast-charging Li-ion batteries is the low potential of graphite anodes. Due to increased cell polarization during high-rate charging, regions of the anode can reach electrochemical potential values more negative than the thermodynamic potential of a Li metal anode (0 V vs. Li/Li^+). As a consequence, Li plating on the graphite surface becomes thermodynamically favorable. The formation of metallic Li dendrites on the anode surface is highly irreversible because the exposure of fresh Li to the liquid electrolyte results in continuous SEI growth and excessive electrolyte decomposition, as discussed in Chapter 2.2. Similar to Li metal anodes, the plated Li microstructures on graphite can also become mechanically or electrically disconnected from the electrode surface during repeated charge/discharge, resulting in the formation of dead Li. The irreversible dead Li formation and SEI growth cause permanent loss of Li inventory and low Coulombic efficiency, leading to significant capacity fade and eventual cell failure.[90,92–94]

There have been several modeling and experimental investigations on the feasibility of fast charging using conventional high-tortuosity graphite anodes (**Figure 2.7**).[78,79,91,95] Gallagher et al. quantified the physical limits of the energy-to-power-density ratio in thick graphite anodes (2.2-6.6 mAh/cm^2 areal capacity loading; 39% porosity), and demonstrated that Li plating is driven by a combination of electrolyte transport and interfacial kinetics.[79] It was concluded that an upper limit of 4 mA/cm^2 current density could be maintained before Li plating occurs. Another recent

report from Argonne National Laboratory also showed that graphite anodes with 1.5 mAh/cm^2 areal capacity loading can sustain 6C charging rates for over 300 cycles. However, when the electrode loading was increased to 2.7 mAh/cm^2, significant capacity fade (> 45%) was observed within the first 50 cycles at a 6C charge rate.[96] Therefore, achieving long-term cycling (> 500 cycles) of Li-ion batteries with high capacity loading (> 3 mAh/cm^2) under fast-charge conditions still remains challenging.

Chapter 5 and 6 will explore alternative electrode structure and material designs to address these challenges. Specifically, Chapter 5 will demonstrate a laser-patterning process to produce 3-D graphite structures with arrays of vertical pore channels thorough the electrode thickness. The aligned pore channels serve as diffusion paths for rapid ionic transport, thereby minimizing Li plating during fast charging. Chapter 6 will discuss the design of hybrid anodes consisting of uniform mixtures of graphite and hard carbon to overcome energy/power tradeoffs. By controlling the graphite/hard carbon ratio, it will be demonstrated that battery performance can be systematically tuned to simultaneously achieve high energy density and efficient fast charging.

Chapter 3

Mass Transport Effects in Li Metal Batteries

Adapted from K.-H. Chen, K. N. Wood, E. Kazyak, W. S. LePage, A. L. Davis, A. J. Sanchez, N. P. Dasgupta, *Journal of Materials Chemistry A* **2017**, 5, 11671 with permission from The Royal Society of Chemistry.[8]

As mentioned in Chapter 2.2, our previous study demonstrated that spatially varying kinetics associated with the formation of dendrites and pits on Li metal surface causes the peaking voltage shape of Li-Li symmetric cells (**Figure 3.1a-b**).[42] However, after extended periods of cycling of Li-Li symmetric cells, the voltage peaking behavior is observed to reduce, and the voltage shape resembles an arc, followed by a plateau (**Figure 3.1c**).[44,74–77,97] Prior to this study, the mechanistic origins of this shift from peaking behavior to an arcing voltage trace were not previously described. This lack of understanding limited our ability to interpret the dynamic evolution of the electrode during extended cycling, and how this eventually leads to cell failure. In a study by Lu et al., a similar arcing voltage shape also evolved during cycling of Li-NCA full cells, which correlated with a decrease in cell capacity. The authors proposed that the origin of dramatic cell capacity fade in Li metal full cells was not due to dendrite growth, but the formation of a highly resistive SEI on the Li metal anode.[98] Therefore, in order to rationally design solutions for improved performance, an improved understanding of the underlying physical phenomena that drive the evolution of voltage changes in batteries that contain Li metal anodes during extended cycling provided the motivation for the work in this chapter.

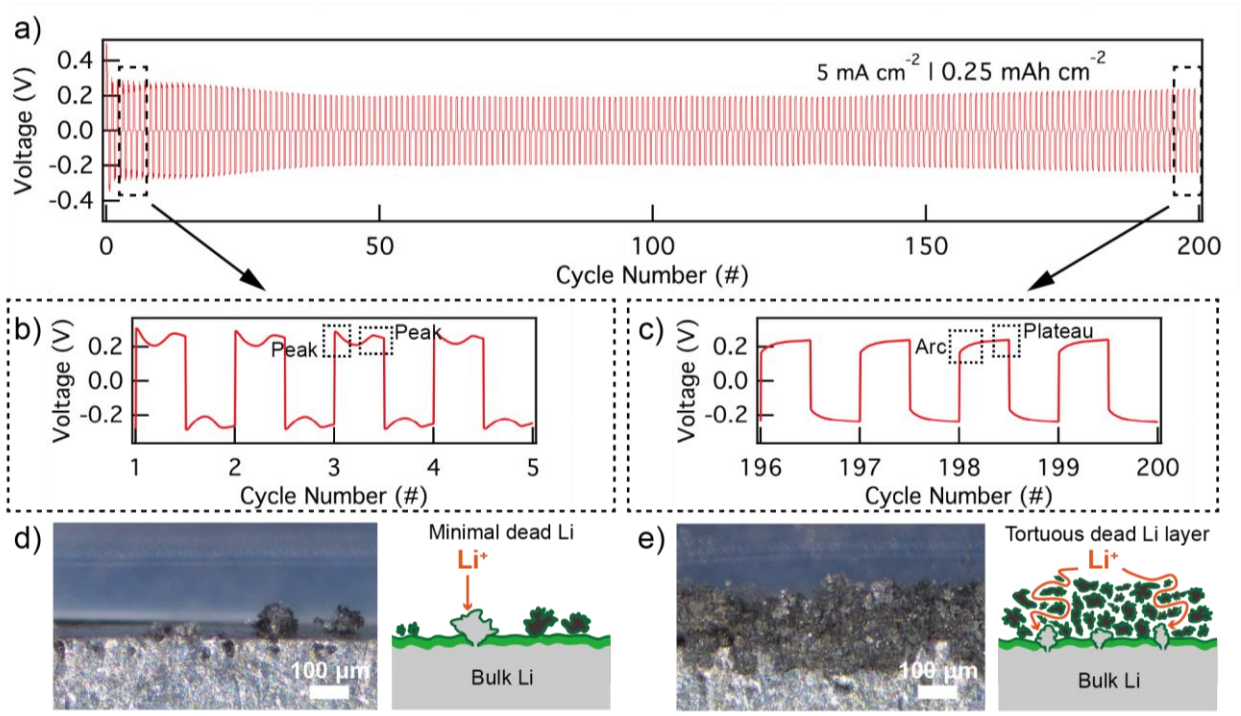

Figure 3.1. (a) Galvanostatic cycling voltage profiles for a Li-Li symmetric cell cycled at 5 mA/cm^2 (0.25 mAh/cm^2) for 200 cycles. (b) Cycles 1-5 exhibit peaking behavior during earlier cycles. (c) Cycles 196-200 exhibit arcing behavior at later cycles with a characteristic arc reaching a plateau at the end of each half cycle. *Operando* microscopy images and corresponding schematics showing Li-ion diffusion at (d) earlier cycles and (e) later cycles.

This chapter focuses on understanding: (1) the origins of the arcing voltage traces during long-term cycling of Li metal anodes in both half and full cell configurations, (2) the impact of the tortuous dead Li layer on mass transport during extended cycling, and (3) why the evolution of dead Li causes capacity fade and failure of full cells containing Li metal anodes. As a result of the tortuous interphases that arise from continuous accumulation of dead Li on the electrode surface (**Figure 3.1e**), we demonstrate that interfacial concentration gradients lead to significant electrode overpotentials. This study provides a detailed understanding of the effect of mass transport through these compact interphases on voltage, capacity, and failure of Li metal electrodes.

3.1 Results and Discussion

3.1.1 Voltage profile observations

Figure 3.1a shows the voltage profile of a Li-Li symmetric cell cycled galvanostatically at 5 mA/cm^2 for 200 cycles. A standard 1 M $LiPF_6$ in 1:1 EC:EMC carbonate electrolyte was used. The peaking behavior observed during the initial cycles (**Figure 3.1b**) can be attributed to transitions between different kinetic pathways at the electrode/electrolyte interphase.[42] At later cycles these double peaks gradually begin to fade and the cell starts to exhibit an arcing voltage profile. This arcing trace has a characteristic "arc", reaching a "plateau" toward the end of the half cycle (**Figure 3.1c**). This change in voltage trace implies that the voltage shape after extended cycling cannot be fully captured by morphology-driven reaction kinetics. We demonstrate here that mass transport effects must be taken into account to explain this shift.

To gain insight into how this transition in voltage profile after extended cycling takes place, cross-sectional *operando* optical microscopy images of a Li electrode surface are shown in **Figure 3.1d-e**. During initial deposition, Li preferentially plates as mossy dendrites on the electrode surface as a result of inhomogeneous nucleation and growth (**Figure 3.2a**).[42] Upon switching polarity, Li is initially stripped from the pre-existing mossy dendrites, since their surfaces represent lower-impedance pathways than stripping from the bulk (**Figure 3.2b**). As active Li is removed from the mossy dendrites, they decrease in size, which results in a larger impedance. As a result of large volumetric changes, mossy structures can mechanically detach from the bulk Li surface, and/or become electrically isolated, forming dead Li.[42,53,54] For subsequent Li dissolution, Li is thus preferentially stripped from the bulk Li, creating surface pits (**Figure 3.2c**). It is noted that upon switching polarity, Li preferentially nucleates on these pits as new mossy dendrites, rather than plating on the inactive dead Li (**Figure 3.2d**).

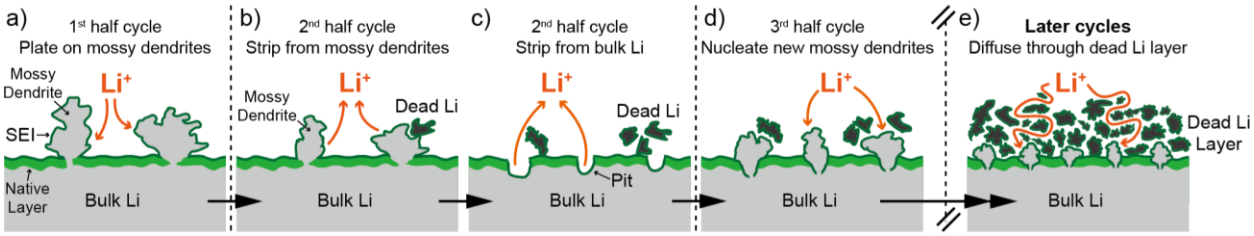

Figure 3.2. Formation of dead Li during initial cycles and the dead Li layer during later cycles. (a) First half cycle: Li is deposited as mossy dendrites on the surface. (b) Beginning of second half

cycle: Li is preferentially dissolved from mossy dendrites resulting in the formation of dead Li. (c) Once active Li in mossy dendrites is depleted, subsequent Li is dissolved from the bulk, forming pits. (d) Third half cycle: Li is nucleated in pits as new mossy dendrites rather than plated on the dead Li. (e) Later cycles: gradual accumulation of dead Li forms a tortuous interphase.

Due to cell stack pressure, dead Li is subject to large mechanical compressive stresses. The accumulated dead Li thus gradually evolves into a "compact interphase" layer between the bulk Li surface and electrolyte (**Figure 3.2e**).[46] The formation and accumulation these types of inactive Li structures have been previously observed through *operando* video microscopy[42] and scanning transmission electron microscopy (STEM).[99,100] While the formation of surface interphases on Li metal is often generalized as a single "SEI" layer in the literature, these microscopy studies demonstrate that the time-dependent decomposition of the electrolyte on the active Li metal surface (*i.e.* SEI) is distinct from the formation of the compact dead Li layer that forms as a tortuous interphase. Therefore, the SEI and the dead Li layer are treated as two separate entities in this work. As the dead Li layer continues to accumulate, the diffusion path length through the dead Li layer continues to increase. This accumulation of dead Li thus leads to mass transport limitations during cell cycling (**Figure 3.1d-e**).

To show that the evolution of the voltage trace shape from peaking to arcing is general, cells were cycled at different depths of discharge and current densities, ranging from 0.1-1.25 mAh/cm^2 and 1-10 mA/cm^2 (**Figure 3.3** and **Figure 3.4**). The transition from peaking to arcing behavior can be seen under a wide range of cycling conditions, demonstrating that the underlying electrochemical phenomena are nearly universal to Li metal in carbonate electrolytes. An increase in total cell polarization is also observed during extended cycling. Therefore, a mechanistic understanding of the origins of these voltage changes, and how they are related to the corresponding increases in dead Li is needed.

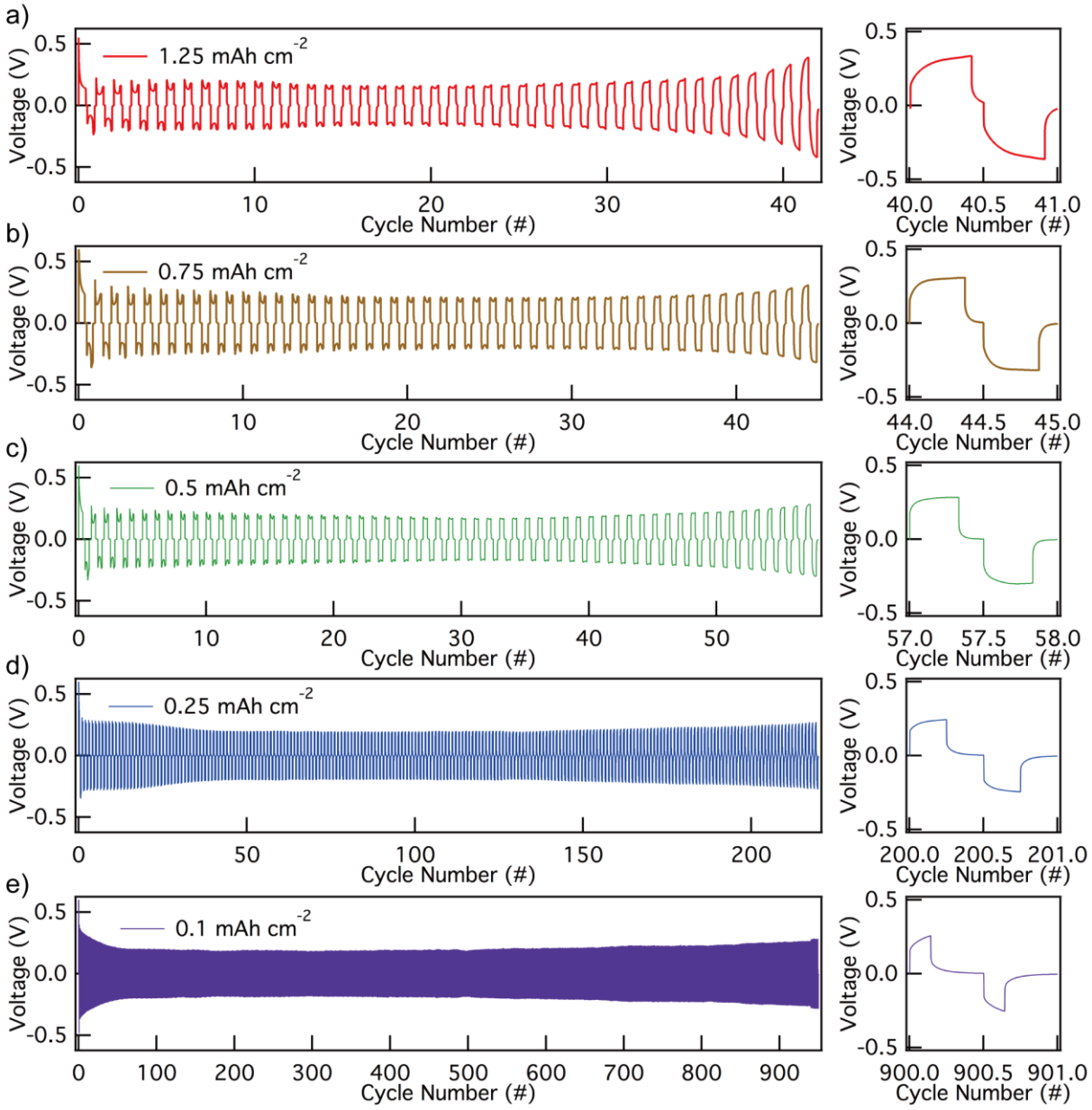

Figure 3.3. Voltage traces of Li-Li symmetric coin cells cycled at 5 mA/cm^2 at different depth of charge/discharge (a) 1.25, (b) 0.75, (c) 0.5, (d) 0.25, and (e) 0.1 mAh/cm^2.

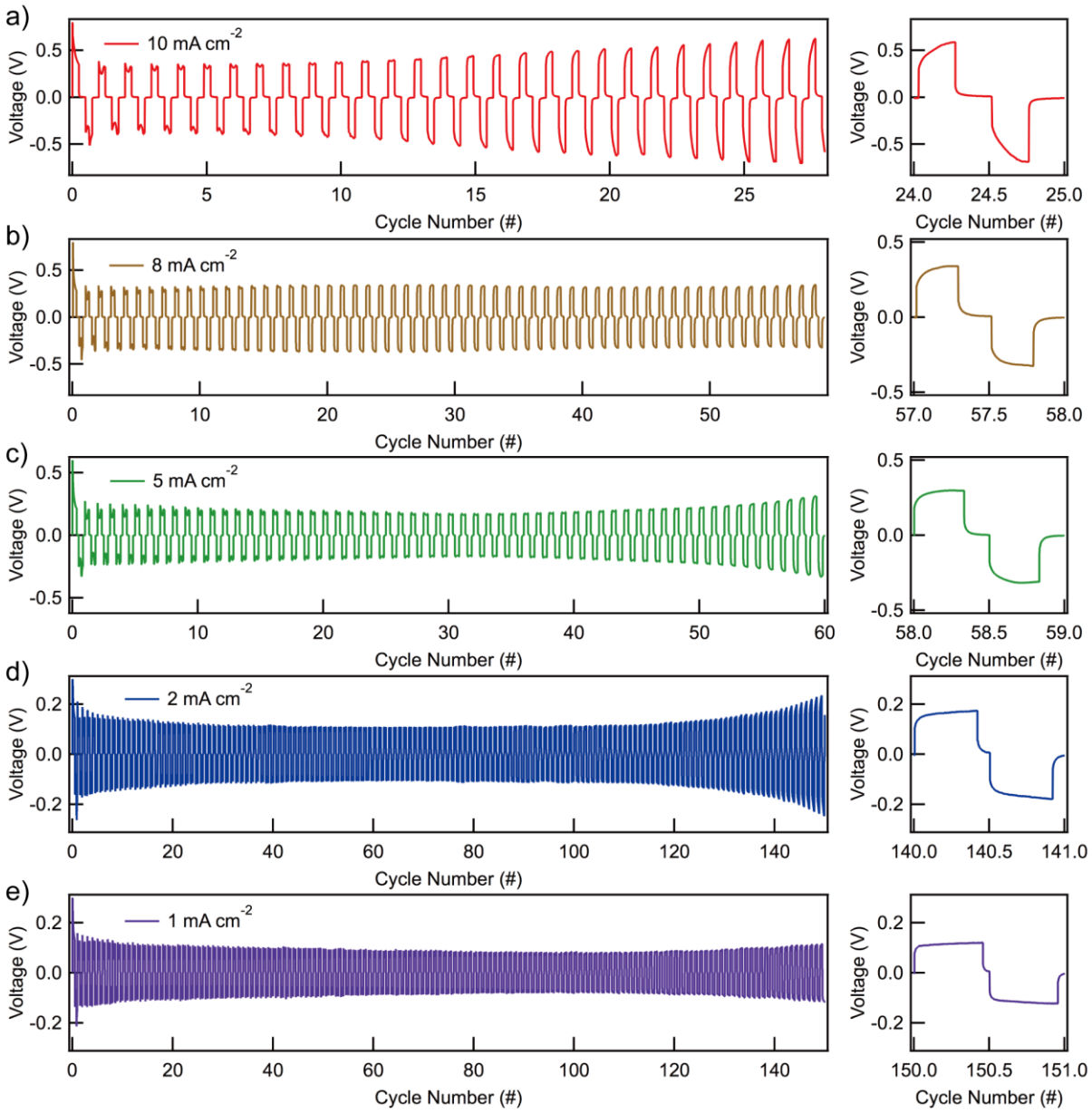

Figure 3.4. Voltage traces of Li-Li symmetric coin cells cycled at (a) 10, (b) 8, (c) 5, (d) 2, and (e) 1 mA/cm^2 at fixed depth of charge/discharge of 0.5 mAh/cm^2.

3.1.2 General framework

During cycling, cell voltage is directly affected by the concentration of Li ions across the electrolyte. In one dimension, neglecting convection, this is described by the continuity equation and the Nernst–Planck equation:

$$\frac{\partial c_i}{\partial t} = -\frac{\partial J_i}{\partial x} = \frac{\partial}{\partial x}\left(D_i \frac{\partial c_i}{\partial x} + D_i c_i \frac{z_i F}{RT}\frac{\partial \phi}{\partial x}\right) \quad (9)$$

where c_i is the concentration of the i^{th} species, t is time, J_i is the mass flux of the i^{th} species, x is the position, D_i is the effective diffusion coefficient of the i^{th} species, z_i is the charge of the i^{th} species, F is Faraday's constant, R is the ideal gas constant, T is the absolute temperature, and ϕ is the electrostatic potential.[42,101,102]

Solving this equation for concentration (c_i) reveals that under equilibrium, a linear concentration profile exists between the electrodes (**Figure 3.5a**, time = t_1). Once a current is applied, Li ions are consumed at the reducing electrode and generated at the oxidizing electrode, forcing the concentration to decrease at one end and increase at the other (**Figure 3.5a**, t_2). To clearly show this point, a schematic of the dynamic Li-ion concentration at the reducing electrode surface ($x = \alpha$) is plotted vs. time (**Figure 3.5**). As cycling progresses, a quasi-steady-state concentration gradient is established,[48,52,103] which is needed to drive Li-ion transport across the cell (**Figure 3.5a**, t_2-t_4). This dynamic evolution of concentration within each half cycle directly affects interfacial kinetics and leads to changes in cell polarization.[104]

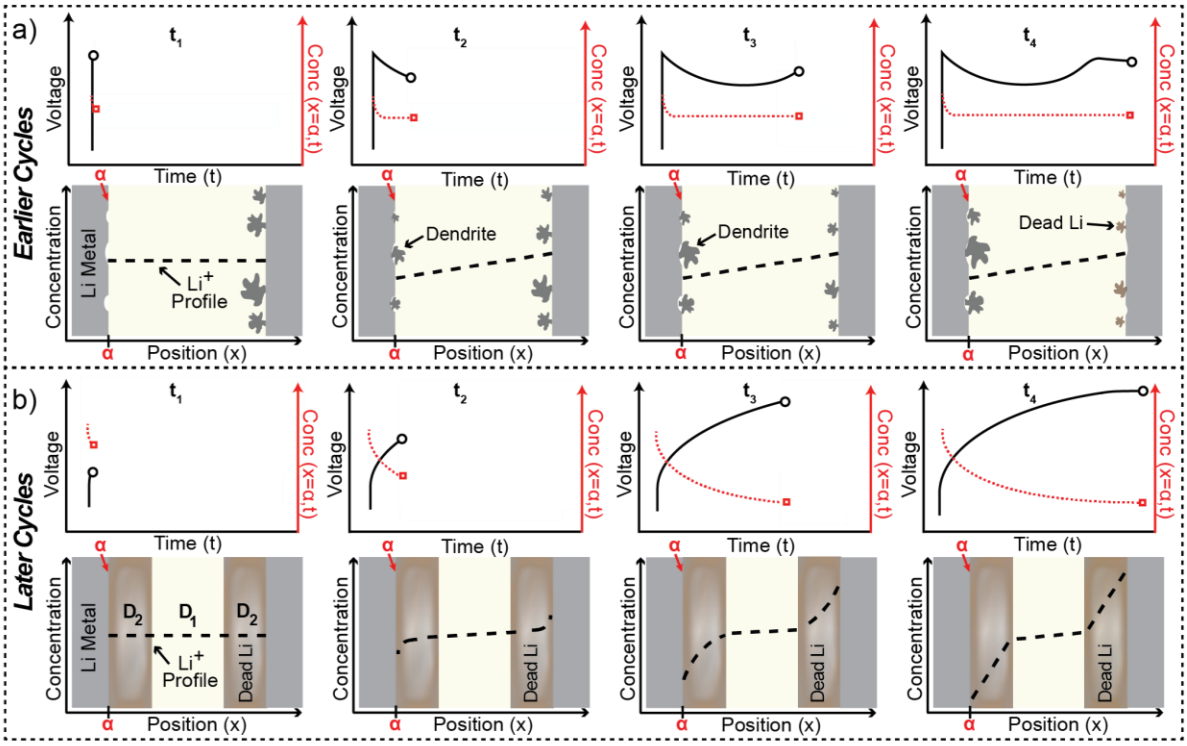

Figure 3.5. Schematic representation of voltage and Li-ion concentration profiles across the cell at (a) earlier and (b) later cycles. Voltage response and Li-ion concentration at the reducing

electrode surface (x = α) are plotted vs. time within different points in time (t_1, t_2, t_3, and t_4) in a half cycle (upper). Concentration vs. position across the cell is also plotted to show the dynamic concentration gradient (lower). D_1 is associated with the effective diffusion coefficient in the electrolyte, whereas D_2 corresponds to the effective diffusion coefficient in the dead Li layer.

The relationship between applied current and overpotential under non-equilibrium conditions is governed by the Butler–Volmer equation. Here, we employ the modified form of the current–overpotential relationship:[42]

$$j = j_o \left[c_{Li}\, exp\left(\frac{(1-\alpha)F\eta}{RT}\right) - c_{Li^+}\, exp\left(-\frac{\alpha F\eta}{RT}\right)\right] \quad (10)$$

$$j_o = \gamma F k^0_{eff} \quad (11)$$

where j is current density, j_o is the exchange current density, c_{Li} is the surface concentration of metallic Li, c_{Li^+} is the surface concentration of Li ions, α is the symmetry factor, η is the overpotential of the electrode, γ is a parameter that accounts for the roughness of the electrode surface, and k^0_{eff} is an effective heterogeneous rate constant that depends upon the morphology of the electrode.

From Equations 10-11, it is clear that the overpotential is affected by both a spatially varying rate constant (k^0_{eff}) and a time varying concentration of Li ions at the interface (c_{Li^+}). During the initial cycles, the surface of the Li metal electrode has a minimal amount of dead Li (**Figure 3.1d**), and ions can move relatively easily across the interphase. As a result, the Li-ion profile reaches quasi-steady-state conditions almost immediately after the half cycle begins, corresponding to the plateau of Li-ion concentration shortly after t_1 (**Figure 3.5a**, red line, t_2). This fast-forming concentration profile creates a relatively small gradient across the cell. Therefore, the time-dependent change in c_{Li^+} is negligible compared to changes in k^0_{eff}. During these initial cycles, the spatially varying rate constant along the electrode/electrolyte interphase is the determining factor in the shape of the cell polarization, creating a well-defined peaking voltage profile (**Figure 3.5a**).[42] This has been experimentally demonstrated by galvanostatic intermittent titration technique (GITT) experiments. GITT measurements allow for intermittent relaxation of the concentration gradients within each half cycle, so that surface reactions occur under nearly equilibrium conditions.[104,105] GITT measurements during these initial cycles show no change in

the peaking voltage profile, demonstrating that the peaking voltage shape is not due to mass transport.[42]

During later cycles, a significant amount of dead Li gradually accumulates on the surface (**Figure 3.5b**). This creates a tortuous pathway for Li-ion transport across the electrode/electrolyte interphase, thus creating regions of varying effective diffusion coefficients (Equation 8). The effective diffusion coefficient of Li ions in the dead Li layer (D_2) becomes smaller compared to that in the liquid electrolyte (D_1) as the dead Li accumulates. Therefore, to sustain the Li-ion transport across the dead Li layer, a greater concentration gradient has to be established. As interfacial concentration (c_{Li^+}) changes, the electrode overpotential increases, which corresponds to an arc in the voltage profile (**Figure 3.5b**, black line, t_2-t_3). Over time, the dynamic concentration gradient reaches its quasi-steady-state equilibrium, and a plateau in the voltage profile is observed (**Figure 3.5b**, t_4).[48,103] Due to the large difference in Li-ion concentration between the electrodes, mass transport now becomes the main factor that determines the shape of cell polarization.

As dead Li continues to accumulate during cycling, an increase in the radius of curvature of the arcs is observed. This occurs due to the large change in interfacial concentration of Li ions (c_{Li^+}) throughout the half cycle. The dead Li evolution impedes diffusion, requiring a longer period of time and greater overpotential to establish the quasi-steady-state concentration gradient. This phenomenon is thus regarded as a mass transport effect. The resulting effect is two-fold: (1) as more dead Li accumulates on the electrode surface, the peaking behavior associated spatially varying rate constant (k^0_{eff}) decreases and becomes obscured by dramatic changes in concentration (c_{Li^+}) occurring at the electrode/electrolyte interphase, and (2) as the arcs appear, their shape and size can then be used to ascertain, cycle-by-cycle, how dead Li is affecting the system.

3.1.3 Li-Li symmetric cell interpretation

Based on the discussion above, we can now analyze the changes in voltage profile due to mass transport effects that result from dead Li. To experimentally demonstrate the effects of mass transport on the evolution of the voltage profile shape, a Li-Li symmetric coin cell was cycled at 5 mA/cm^2 for 1.25 mAh/cm^2 per charge/discharge cycle (**Figure 3.6a**). After each half cycle, the cell was allowed to relax (no applied current) for 3 minutes. The peaking voltage behavior can be

seen in the initial phase of cycling, whereas an arcing voltage trace gradually becomes dominant as cycling continues. At higher cycle numbers, both the radius of curvature of the arc (at the beginning of each half cycle) and the final magnitude of overpotential become larger.

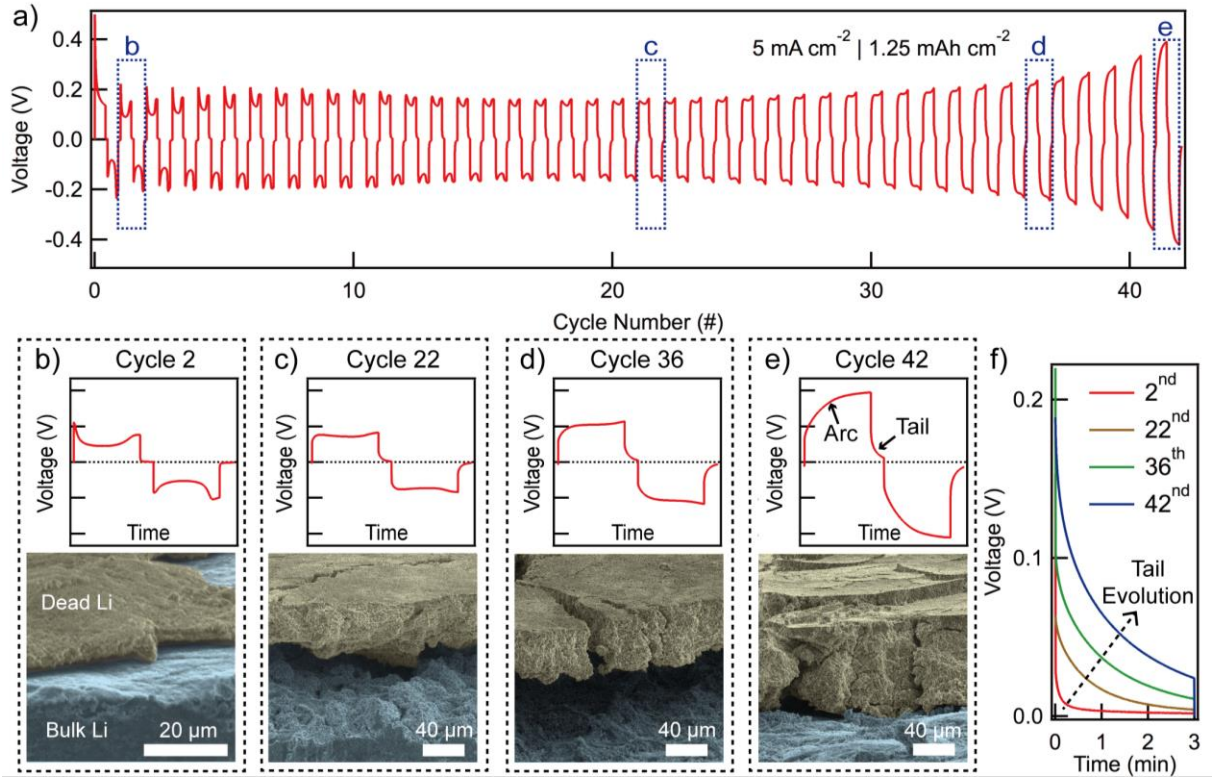

Figure 3.6. (a) Galvanostatic cycling voltage profiles for a Li-Li symmetric cell showing the transition from peaking to arcing behavior at 5 mA/cm^2 (1.25 mAh/cm^2). Voltage traces of (b) cycle 2, (c) cycle 22, (d) cycle 36, and (e) cycle 42 show the effects of extended cycling on the voltage shape and morphological evolution of dead Li layer under SEM. (f) The cycle-to-cycle evolution of voltage tails occurring during the 3-minute rest period demonstrates the time needed for the Li-ion concentration to relax back to equilibrium conditions become larger.

To help correlate the evolution of the voltage trace shape with the tortuous pathway for Li-ion transport through the dead Li layer, a series of high resolution voltage traces are shown with corresponding SEM images taken at the end of each cycle (**Figure 3.6b-e**). During the 2nd cycle (**Figure 3.6b**), the voltage trace exhibits a peaking behavior and the voltage relaxes back to open circuit almost instantaneously once the applied current is removed. The corresponding SEM image reveals a thin layer of dead Li with an average thickness of 4 μm formed on the surface. At this thickness, Li-ion transport through the dead Li layer is relatively unimpeded, and the impact of the

lower effective diffusion coefficient on cell polarization is minimal. At this point, the spatially varying reaction rates are the dominant factor determining the voltage shape, which has been previously shown to result in a peaking voltage profile.[42]

For the 22nd, 36th, and 42nd cycles, the voltage traces reveal a gradual evolution in the arcing behavior (*i.e.* more pronounced arcs and reduced peaking), as shown in **Figure 3.6c-e**. The SEM images show that as cycling proceeds, the thickness of the dead Li layer continues to grow, reaching 38 μm and 50 μm after the 22nd and 36th cycles, respectively. After cycle 42, a dead Li layer with an average thickness of 68 μm is observed, confirming the continuous accumulation of dead Li.

Similar to the arcs, the evolution of voltage "tails" that occur during cell relaxation (no applied current) can be related solely to the difference in Li-ion concentration between the electrodes. As seen in **Figure 3.6f**, as cycling continues, the tails associated with relaxation to the equilibrium concentration profile become larger and more pronounced, indicating the overpotential associated with mass transport becomes larger. These insights again confirm that the build-up of a tortuous dead Li layer impedes ion transport and is the reason for the arcing voltage trace.

3.1.4 Galvanostatic intermittent titration technique

To deconvolute the effects of reaction kinetics from mass transport during cycling, GITT experiments were conducted.[104] The galvanostatic current was periodically interrupted every 15 seconds during a half-cycle, with a 3 minute rest period in between applied current periods, as shown in **Figure 3.7d**. Since establishing a quasi-steady-state concentration gradient in the electrolyte is a time-dependent process, GITT can limit the effects of evolving concentration gradients on cell polarization. By depositing very small amounts of Li after long periods of relaxation, each Li-ion can be deposited at near static equilibrium conditions. Accordingly, each ion that is deposited will experience reduced effects from the depletion of ions in the electrolyte at the interphase. By selecting the appropriate period and rest time for current relaxation, GITT data can reveal an envelope voltage shape (constructed by connecting the maximum voltages of each interrupt) that occurs due to changes in reaction rate across the surface.

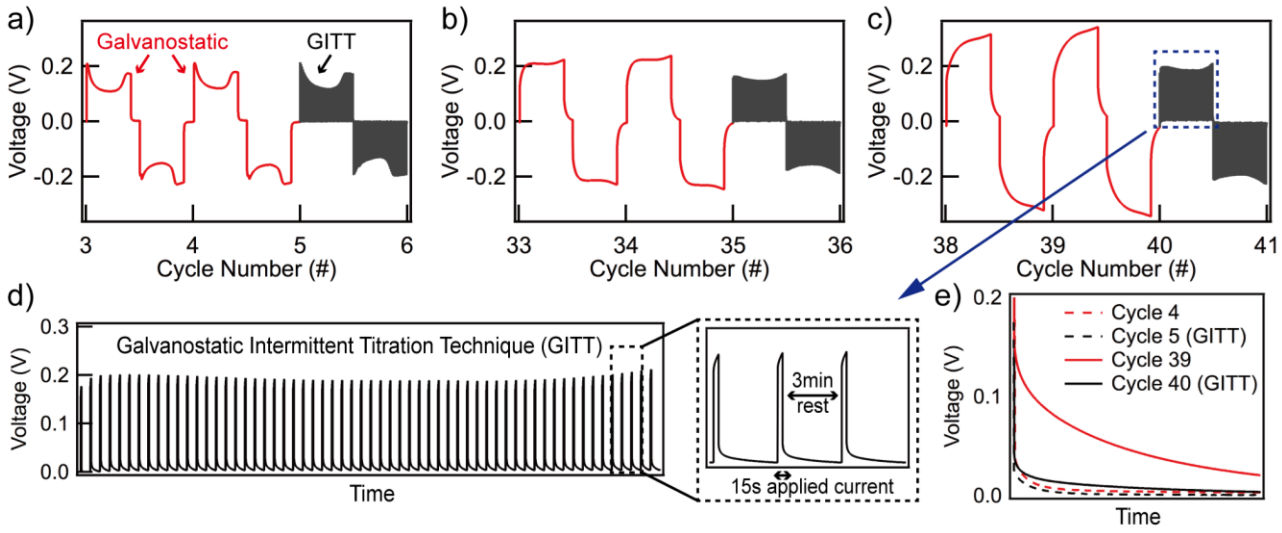

Figure 3.7. Voltage profile of GITT in Li-Li symmetric cells at (a) cycle 5, (b) cycle 35, and (c) cycle 40. (d) GITT was carried out by a sequence of cycling at 5 mA/cm^2 for 15 seconds followed by a rest period of 3 minutes. This sequence was carried out until the amount of charge under galvanostatic conditions was 1.25 mAh/cm^2. (e) The voltage tails under galvanostatic conditions at cycle 4 and 39 and the voltage tails of GITTs at cycle 5 and cycle 40.

As shown in **Figure 3.7a**, performing GITT in a reaction rate limited regime (during earlier cycles, before large amounts of dead Li have accumulated on the surface) reveals that the peaking shape of the voltage profile is not noticeably affected by relaxation. This verifies that mass transport negligibly affects cell polarization during the initial cycles.

During the transition between peaking and arcing regions of the voltage profile (**Figure 3.7b**), the GITT data begin to show a significant difference in shape when compared to the constant applied current of the previous two cycles. Here, the interrupted voltage profile exhibits peaking behavior, while the characteristic arc associated with mass transport limited behavior disappears, despite the significant accumulation of dead Li (as shown in a comparative cycle in **Figure 3.6d**). This demonstrates that the fundamental kinetic behavior responsible for peaking behavior (associated with formation of dendrites and pits) still occurs during extended cycling, but is "masked" by the dominant contribution of concentration limited mass transport to total cell polarization.

The GITT voltage profile has a significantly lower total overpotential compared to the uninterrupted galvanostatic voltage trace from the previous cycle. This demonstrates that the overpotential associated with mass transport is responsible for the increasing cell polarization at

this phase of cycling. Furthermore, comparing the difference between GITT profiles at cycle 5 and cycle 35, the amplitude of the peaking shape (difference between maximum and minimum overpotential during the half cycle) is lower for cycle 35. This indicates that while changes in the reaction kinetics remain present during extended cycling, these changes have a reduced effect on the overall shape of the voltage profile than in the initial cycles.

By cycle 40 (**Figure 3.7c**), the galvanostatic voltage trace has completely transitioned from peaking to arcing. However, the GITT data again demonstrate that the underlying effects of kinetics are present if large changes in concentration gradients throughout the half-cycle are limited. GITT measurements are thus a powerful tool to examine cell performance by revealing the underlying morphological changes that still occur on the electrode, even during half cycles that exhibit an arcing behavior.

The voltage tail shape during relaxation between half cycles is also affected by GITT. Similar to the results shown in **Figure 3.6f**, **Figure 3.7e** demonstrates that the time it takes for the voltage to relax back to equilibrium after an applied current is removed is much greater for cycle 39 (red solid line) than for cycle 4 (red dashed line). This increase in relaxation time is due to the large concentration gradient across the cell. By comparison, the voltage tails for the GITT measurements require a nearly identical time for relaxation for cycles 5 and 40. This further demonstrates that the origins of increasing voltage tails during cycling are also due to mass transport, which can be deconvoluted using GITT measurements.

3.1.5 Mass transport effect in full cells

To show the impact of dead Li on full-cell battery performance, Li metal anodes were coupled with Li cobalt oxide (Li_xCoO_2 or LCO) cathodes to make Li metal full cells, which were cycled at a 1C rate (1.5 mA/cm^2). Observation of the voltage profile shapes during charging steps shows a distinct transition from peaking to arcing upon extended cycling (**Figure 3.8a** and **Figure 3.8d**), demonstrating that the insights from Li-Li symmetric cell analysis are directly applicable to full cells.

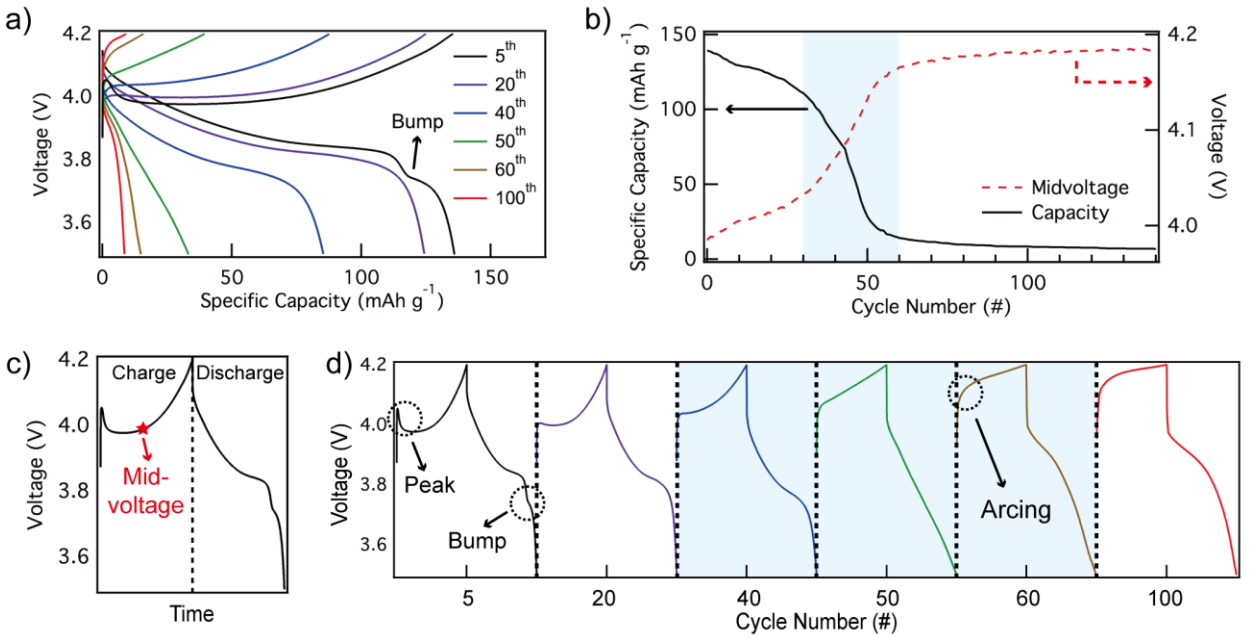

Figure 3.8. A Li-LCO full cell cycled at 1C-rate (1.5 mA/cm^2) between 4.2 V and 3.5 V (2-electrode), showing the effect of the dead Li on the full cell performance. (a) Traditional plot of voltage vs. capacity as a function of cycle number. (b) Discharge capacity and mid-voltage was plotted vs. cycle number, which shows the trend of decreasing capacity and increasing mid-voltage throughout cycling. (c) An example of the mid-voltage measurement (the halfway point in terms of total capacity for each charge cycle). (d) Voltage vs. cycle number showing how the voltage profile of the full cell changes during extending cycling.

Upon cycling at 1C, a peak associated with dendrite nucleation on the anode surface is observed in the charging voltage profiles, as shown in **Figure 3.8a** (cycle 5). Similarly, a bump in the discharge profile can be linked to the transition from dissolving mossy dendrites to removing Li from the bulk.[42] To clearly show that these voltage shapes are associated with the anode, three-electrode measurements were conducted, which decouple the variations in anode and cathode potential as a function of state-of-charge (**Figure 3.9**). This illustrates a very important point that is often neglected in analysis of cathode performance when a Li metal anode is used, where the potential of the two-electrode cell is often reported as voltage "*vs.* Li/Li$^+$", implying a thermodynamically reversible Li electrode that does not vary as a function of state of charge/discharge. This approximation is invalid at finite current densities, as there is a non-negligible contribution to total cell polarization from the dynamic morphological evolution of the Li metal surface and interphase, which affects electrode overpotentials and varies throughout cycling.

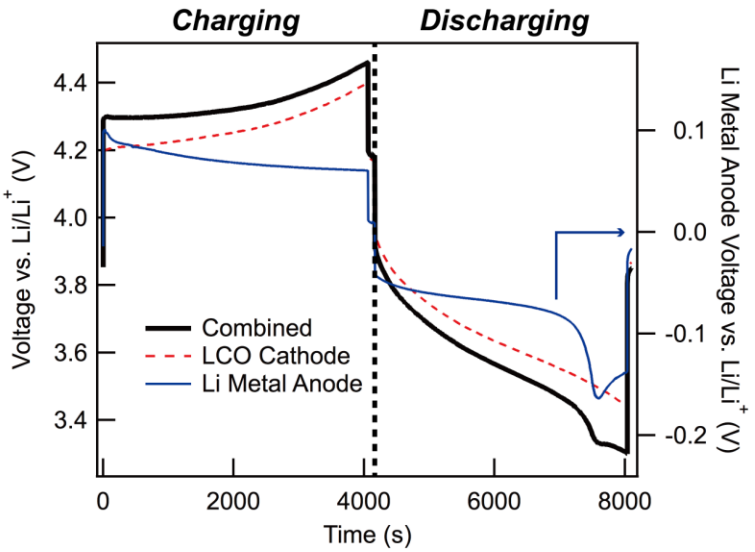

Figure 3.9. Three-electrode measurements of a Li-LCO full cell shows the cell polarization contributions from both the Li metal anode and LCO cathode during earlier cycles. For visual aid, Li metal anode voltage has been multiplied by -1 such that the total cell voltage (combined) = LCO Cathode + Li Metal Anode.

To clearly show how the voltage profile shape changes during cycling of full cells, a plot of voltage vs. cycle number is shown in **Figure 3.8d**. Plotting data in this manner, instead of the more traditional voltage *vs.* capacity (**Figure 3.8a**), enables a more clear observation of voltage shape changes. Using this data, it can be clearly seen that the peaking associated with dendrite nucleation gradually disappears over the first 40 cycles, and an arcing voltage trace associated with the accumulation of dead Li becomes continually more pronounced.

To illustrate how these changes in voltage can affect the measurement of cell capacity, the voltage value at the halfway point in time of each charge cycle (mid-voltage in **Figure 3.8c**) is recorded and plotted in the same graph with capacity *vs.* cycle number, as shown in **Figure 3.8b**. The mid-voltage value increases during the transition from peaking to arcing. By comparison, the cell capacity exhibits an almost perfect inverse relationship, demonstrating a sharp decrease in capacity between cycle 30 and cycle 60 (shaded region). This dramatic capacity fade has been previously reported for full cells cycled at high C-rates, and the sharp decrease in capacity is often considered "cell failure".[53,98,106,107] The strong inverse relationship between mid-voltage and capacity suggests that the evolution of the dead Li (associated with the increasing overpotential and the transition from peaking to arcing) is directly affecting the performance and failure of the full cell. SEM images were taken at different points of cycling to support this statement (**Figure**

3.10). Therefore, a discussion of how dead Li accumulation on the Li metal anode directly impacts the evaluation of full cell performance is warranted.

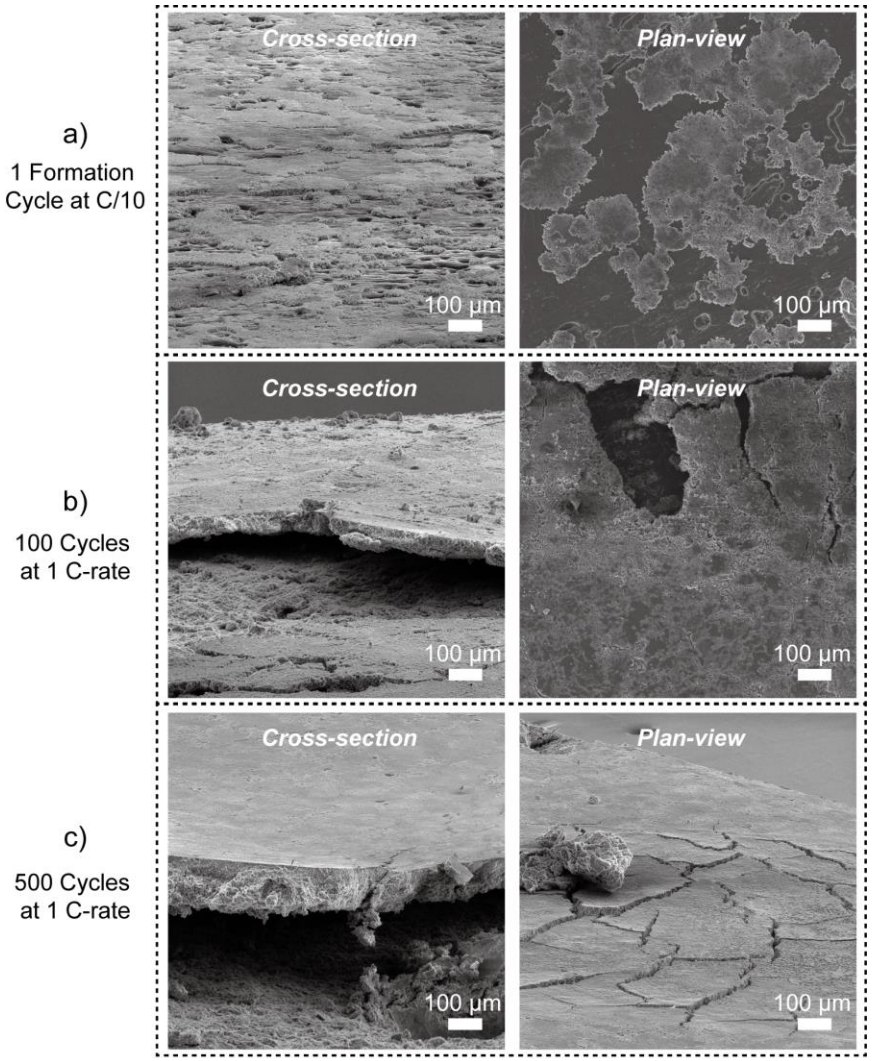

Figure 3.10. SEM images of Li metal anodes collected from Li-LCO full cells after (a) one formation cycle at C/10, (b) 100 cycles at 1C, and (c) 500 cycles at 1C.

3.1.6 Failure mechanism in full cells

In full cells, cut-off voltages are often set to avoid overcharging and other undesirable reactions. LCO (Li_xCoO_2) is considered fully delithiated (x = 0.5) at 4.2 V (vs. Li/Li^+), and fully lithiated (x = 1) at 3.88 V (vs. Li/Li^+).[108–110] However, during cycling, the measured cell voltage (V_{cell}) is the sum of overpotential of electrodes (η) and electrolyte (IR) in addition to the thermodynamic potential of the cell (open circuit potential, V_{oc}).

$$V_{cell} = V_{oc} + IR + \eta \quad (12)$$

Here, the *IR* drop remains stable under normal conditions, therefore the dramatic morphological evolution and accumulations of dead Li on anode surfaces cause η to vary significantly, and increase with extended cycling. It is noted that the accumulation of the dead Li at the anode causes large changes in interfacial concentration of Li ions on both reducing and oxidizing electrodes, even in a full cell. As a result, the overpotential of both anode and cathode increase due to the evolution of dead Li from the Li electrode. Since all consumer batteries are two-electrode instead of three-electrode, the voltage contribution from overpotential compared to the open circuit voltage unknown. Therefore, 4.2 V is typically set as a cut-off voltage for safety. As a result, during charging, although the cell (V_{cell}) is cut off at 4.2 V, the state of the LCO will not be fully delithiated. Similarly, during discharge, if the cell is cut off at 3.5 V, the LCO will not be fully lithiated.

To measure the true lithiated state of the cathode, open circuit voltages (V_{oc}) were measured by taking a 3 min rest period after each half cycle. During the relaxation, no current was applied and thus no contribution from overpotential is measured. A plot of V_{oc} measurements after each charge and discharge cycle is shown in **Figure 3.11a**. As can be observed in the figure, the difference between the potential of delithiated LCO ($Li_{0.5}CoO_2$) and charge V_{oc} can be correlated to the overpotential during charge cycles (η_{charge}). Likewise, the overpotential during discharging ($\eta_{discharge}$) is the difference between the potential of lithiated LCO ($LiCoO_2$) and discharge V_{oc}. The area between the charge V_{oc} and discharge V_{oc} is thus the "true" cycling voltage range (ΔV_{oc}). As the dead Li layer evolves (increasing η), the cell begins to be cycled between a much shallower voltage range, meaning the capacity of the cathode is not being fully utilized. Therefore, this leads to a dramatic drop in the measured cell "capacity".

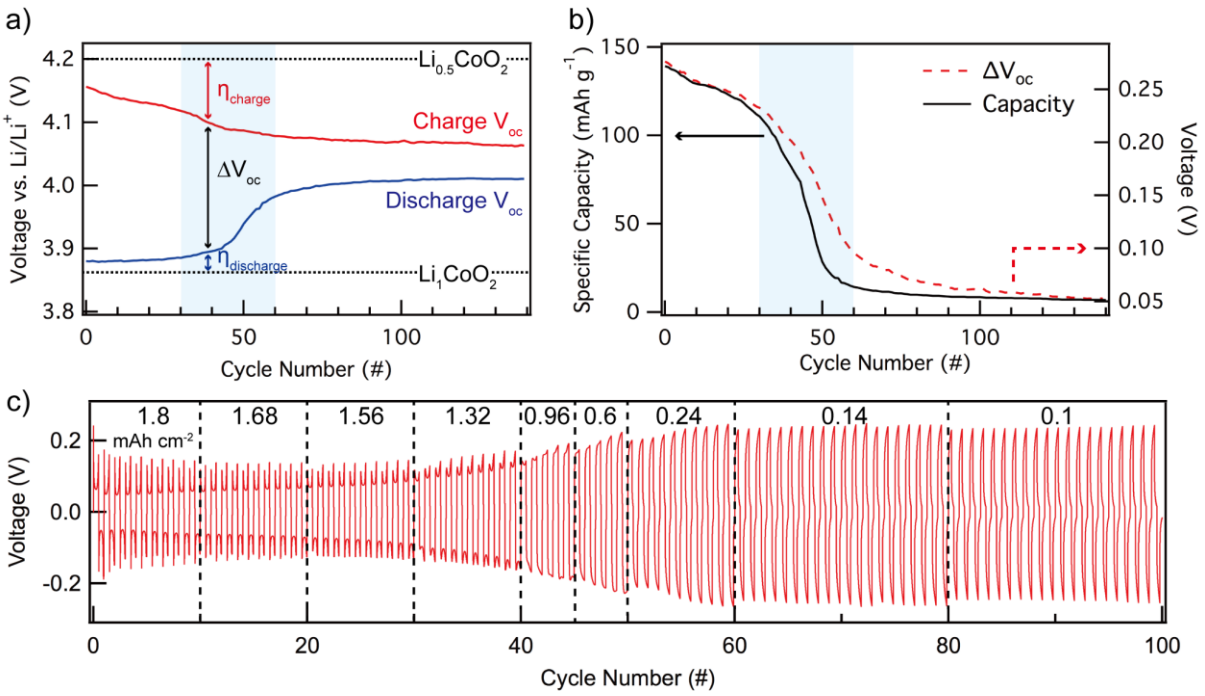

Figure 3.11. (a) Open-circuit voltage (V_{oc}) were measured after each charge/discharge cycle and plotted vs. cycle number. The LCO cathode is considered fully delithiated ($Li_{0.5}CoO_2$) at 4.2 V vs. Li/Li^+ and fully lithiated (Li_1CoO_2) at 3.88 V vs. Li/Li^+. (b) Discharge capacity and V_{oc} were plotted vs. cycle number throughout cycling. (c) A Li-Li symmetric cell cycled to mimic the decreasing depth of discharge for the full cell Li metal anode.

The way that this "true" voltage range changes during cycling can thus be directly linked to the capacity fade of the cell. As shown in **Figure 3.11b**, as ΔV_{oc} decreases between cycle 30 and cycle 60, a corresponding drop in capacity is observed. This further proves that the perceived rapid capacity fade and "failure" in the Li metal full cell batteries is due to the build-up of the dead Li at the anode rather than an effect of cathode capacity loss.

To further demonstrate that the cathode is not subject to significant capacity loss throughout cycling at these conditions, a coin cell that was cycled to "failure" was disassembled, and the LCO electrode from the cycled cell was collected and "re-cycled" in a cell with a fresh Li metal electrode without further treatments. A high discharge capacity of 124.8 mAh/g was obtained, suggesting that LCO is relatively stable during extended cycling vs. Li metal (**Figure 3.12**).

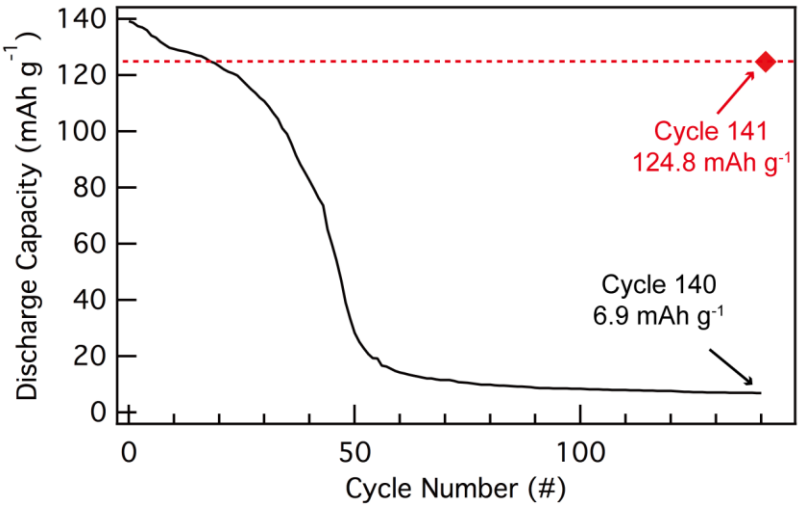

Figure 3.12. Discharge capacity vs. cycle number was plotted for both the original cell (cycle 1-140) and the newly assembled cell (cycle 141).

To demonstrate the powerful value of Li-Li symmetric cells in understanding the ultimate performance of full cells containing Li metal anodes, a symmetric cell was cycled (at the same current density and under a constantly changing depth of discharge) to mimic the changing capacity observed in full cells. The resulting voltage profile is shown in **Figure 3.11c**. As shown in the figure, the evolution of the growing overpotential during the transition from peaking to arcing behavior can be clearly seen in the voltage trace (cycle 30-60), which is the identical region that this transition was observed in the full cells.

It is also confirmed that short-circuiting due to dendrite growth is not the reason for failure of the Li-LCO cell. In the case of the full cell, a dendritic short would cause a large and nearly instantaneous drop in capacity instead of the fading capacity observed in **Figure 3.11b**. This is confirmed by the fact is that the Li-Li symmetric cell cycled under similar conditions to the full cell (**Figure 3.11c**) does not exhibit any erratic voltage behavior (fuse effect) or the ~0 V (actual short circuit) associated with dendritic shorting.[43,48,75,111]

3.2 Conclusions

This work demonstrates that voltage profiles during extended cycling can be correlated to the accumulation of dead Li on the electrode surface in both Li-Li symmetric cells and full cells containing Li metal anodes. This correlation has led to several key points of understanding:

(1) The tortuous interphase of accumulated dead Li impedes ionic mass transport, resulting in a lower effective diffusion coefficient. Therefore, to sustain Li-ion transport across cells under applied current, a greater concentration gradient has to be established. This requires a longer period of time for the concentration profile to reach quasi-steady-state conditions, and thus this is what limits the performance of Li metal anodes at extended cycles.

(2) At earlier cycles, a quasi-steady-state concentration profile is reached relatively quickly with a negligible concentration difference across the cell. This means that the voltage peaking behavior is limited by reaction kinetics, due to the evolving morphology. At later cycles, the accumulation of dead Li leads to large concentration gradients, which in turn causes the voltage behavior to be limited by mass transport. This leads to an arcing voltage trace. As the dead Li layer continues to grow, increasing mass transport limitations result in more pronounced arcs and tails and increasing overpotential.

(3) GITT can limit the effect of concentration gradient by depositing Li at near static equilibrium conditions. The observed peaking behavior during GITT analysis suggests that dendrite growth and surface pitting still occur even when the shape of the voltage trace is dominated by mass transport limitations. In addition, the GITT voltage profile has a significantly lower total overpotential compared to the uninterrupted voltage trace, indicating that mass transport is the reason for the increasing cell polarization at later cycles. Therefore, this technique can serve as an effective way to evaluate the kinetic behavior and morphological evolution of Li metal anodes without being convoluted by mass transport effects.

(4) The transition from peaking to arcing in voltage profile shape was also observed in full cells with Li metal anodes. This suggests that the failure mechanism of Li-metal batteries can be attributed to the build-up of dead Li on Li metal anode surfaces. The dead Li layer affects the interfacial concentration of Li ions, resulting in increasing overpotential of both electrodes. This can cause cells to reach cut-off voltages prior to the targeted cathode composition during lithiation/delithiation. Cycling between limited voltage ranges hence results in a perceived capacity loss and eventually leads to cell failure. Li-Li symmetric cells cycled at similar conditions exhibit increased overpotential and arcing voltage profiles at the same point in cycling. This demonstrates that the dramatic capacity fade often observed in Li metal full cells originates from dead Li, rather than dendrite shorting or electrolyte depletion. This underscores the need for reduced dead Li formation to enable improved performance in full cells.

(5) This work provides a detailed analysis of the transition from peaking to arcing in voltage profiles, and explains why the evolution of dead Li can be directly linked to the capacity fade and failure in full cells containing Li metal anodes. It is shown that electrode overpotentials should not be neglected when analyzing full cells due to the dynamic morphological evolution of the Li metal surface and interphase. Therefore, Li-Li symmetric cell analysis can serve as a powerful tool to observe how Li metal anodes dynamically evolve and understand the corresponding underlying physical phenomenon during cycling. The results from this study will enable researchers to more accurately evaluate the effectiveness of new methods that improve Coulombic efficiency and reduce dead Li formation based on interpretation of voltage traces, and rationally design solutions for improved anode performance in Li-metal batteries rather than relying on empirical observations.

3.3 Materials and Methods

All air sensitive materials were handled in an argon-filled glovebox (MBRAUN), with oxygen and moisture levels < 5 ppm. 1 M $LiPF_6$ (Soulbrain) in 1/1 EC/DMC was used as the electrolyte in this work, which contained < 7 ppm water.

3.3.1 Li-Li symmetric cells

Li-Li symmetric cells were assembled with CR-2032 coin cell shells, spacers, and wave springs (MTI Corp.), each having two Li metal electrodes, one Celgard 2325 separator, and 45 μl of the $LiPF_6$ electrolyte. Li foil (Alfa Aesar, 0.75mm thick) was punched into 1.6 cm^2 discs and were cleaned in pentane with a vortex mixer for 30 seconds prior to assembly into coin cells. A hydraulic crimping press was used to fabricate the coin cells. The electrochemical performance of the coin cells was evaluated by galvanostatic charge/discharge on a Landt 2001a battery testing station at room temperature.

3.3.2 Li-LCO full cells

The LCO cathode material was provided by the CAMP Facility at Argonne National Laboratory. LCO electrodes with a mass loading of 14.53 mg/cm^2 were punched into 1.6 cm^2 discs.

Full cells were assembled with one LCO cathode, one Li metal anode, one Celgard 2325 separator, and 45 μl of the $LiPF_6$ electrolyte. The electrochemical performance of the full cells was evaluated by galvanostatic cycling in the voltage range of 3.5–4.2 V. One formation cycle was initially conducted at C/10 prior to any subsequent cycling.

3.3.3 SEM characterization

Cycled Li metal electrodes were collected from coin cells for SEM characterizations. Cells were first uncrimped using a disassembly die in the same MTI crimping press and electrodes were removed and rinsed with fresh DMC for three times before drying in the glovebox. SEM images of the Li metal electrodes were obtained using a Tescan MIRA3 FEGSEM.

3.3.4 *Operando* video microscopy

Operando optical microscopy was performed in a custom-built visualization cell, as described in our previous study.[42] The entire assembly is air-tight with a quartz viewing window and O-ring seal so that it can be removed from the glovebox after assembly and placed under an optical microscope for viewing. Visualization cell experiments were carried out using a Biologic VSP potentiostat. The optical microscopy images were taken with a Nikon LV150N microscope.

3.3.5 Three-electrode measurements

Three-electrode measurements were conducted using a hermetically sealed glassware setup. The reference electrode was a scraped and cleaned piece of Li metal foil. The data was collected using the bipotentiostat capabilities of the Biologic VSP system, which can measure the potential of the counter electrode and working electrode vs. reference electrode simultaneously.

Chapter 4

Design of Current Collectors for High-Efficiency Li Metal Anodes

Adapted from K.-H. Chen, A. J. Sanchez, E. Kazyak, A. L. Davis, N. P. Dasgupta, *Advanced Energy Materials* **2019**, 9, 1802534 with permission from Wiley-VCH.[9]

One of the key conclusions from Chapter 3 is that there is a need to reduce dead Li formation on the Li metal anode surface in order to improve cell performance. This can be addressed by designing novel electrode architectures and modifying the properties of the electrode-electrolyte interface. In particular, current collectors play a critical role in determining the performance of Li metal batteries because their geometry and surface chemistry both influence the uniformity of Li plating/stripping during cycling.

Planar Cu foils have been widely used as a current collector/substrate for Li metal anodes owing to their relatively-good stability against Li metal and compatibility with roll-to-roll manufacturing. However, cycling under practical current densities leads to non-uniform Li deposition due to an inhomogeneous Li-ion flux along the electrode surface, resulting in the onset of mossy or dendritic Li growth.[43] The formation of high-surface area Li causes a significant reduction in Coulombic efficiency and prevents long-term cycling of Li metal anodes.[8] One consequence of these issues has been the need to incorporate excess Li, which can be pre-deposited onto the anode current collector to compensate for losses that occur over the life of the cell. This compromises energy density and complicates manufacturing. Therefore, suppressing the formation of high-surface area Li structures during cycling is essential to improve the overall cycle life and efficiency of Li metal batteries.

Recently, there has been a dramatic increase in the number of publications exploring the use of 3-D current collectors to address these problems.[70,72,73,75,112–116] Several studies have shown that by using micro- or nano-structured current collectors, the effective current density can be

reduced due to an increase in electro-active surface area, promoting more uniform Li plating/stripping during cell cycling.[70,113,117] In addition, 3-D structures can better accommodate the large volumetric changes that occur during Li plating/stripping, which reduces overall cell volume changes. While these studies have demonstrated the advantages of 3-D current collectors, they often compare a planar control electrode to a disordered 3-D structure[72,73,116], rather than rationally controlling geometric parameters in highly ordered structures to achieve an optimal performance. Furthermore, while disordered structures lead to significant increases in surface area, they also introduce significant tortuosity to the electrode, which can lead to mass transport limitations during Li plating/stripping at high current densities. In addition, the majority of these previous reports do not explore surface modifications of 3-D current collectors to further tune the interfacial chemistry for improved performance. While a few studies have included surface coatings[114,115], there is a general lack of mechanistic insight into the decoupled roles of geometry and surface chemistry in coated 3-D architectures.

This work first demonstrates a bottom-up fabrication process using templated electrodeposition of vertically-aligned Cu pillars as a current collector/substrate for Li metal electrodeposition and dissolution. Using the highly-ordered arrays of uniform pillars as a model platform, the morphology of Li plating/stripping upon cycling can be controlled by tuning the pillar diameter, pore spacing, and pillar length. Another advantage of the vertical pillar geometry is that tortuosity is reduced to approximately 1, as opposed to highly tortuous disordered geometries. In addition, deposition of an ultrathin layer of ZnO by ALD on the current collector surface is shown to further facilitate uniform Li nucleation, which influences the morphology and reversibility of subsequent Li plating/stripping. The resulting core-shell pillar architecture allows for the geometry and surface chemistry to be decoupled and individually controlled to optimize the electrode performance. Leveraging the synergistic effects of the optimized geometry and interface modification, we will demonstrate cycling of Li metal anodes with Coulombic efficiency of 99.5% at a current density of 0.5 mA/cm^2 and depth of discharge of 2 mAh/cm^2, and 99.4% at 1 mA/cm^2 and 2 mAh/cm^2, which are among the highest reported values in the literature.[59,68]

4.1 Results and Discussion

4.1.1 Fabrication and characterization of Cu pillar arrays

Vertically-aligned Cu pillar arrays were fabricated using templated electrodeposition, which has been previously used to synthesize metal nanostructures.[118,119] In this approach, a porous polycarbonate track-etched (PCTE) membrane is used as a template and the Cu is electrochemically deposited into the cylindrical pores with well-defined pore sizes (**Figure 4.1a**).

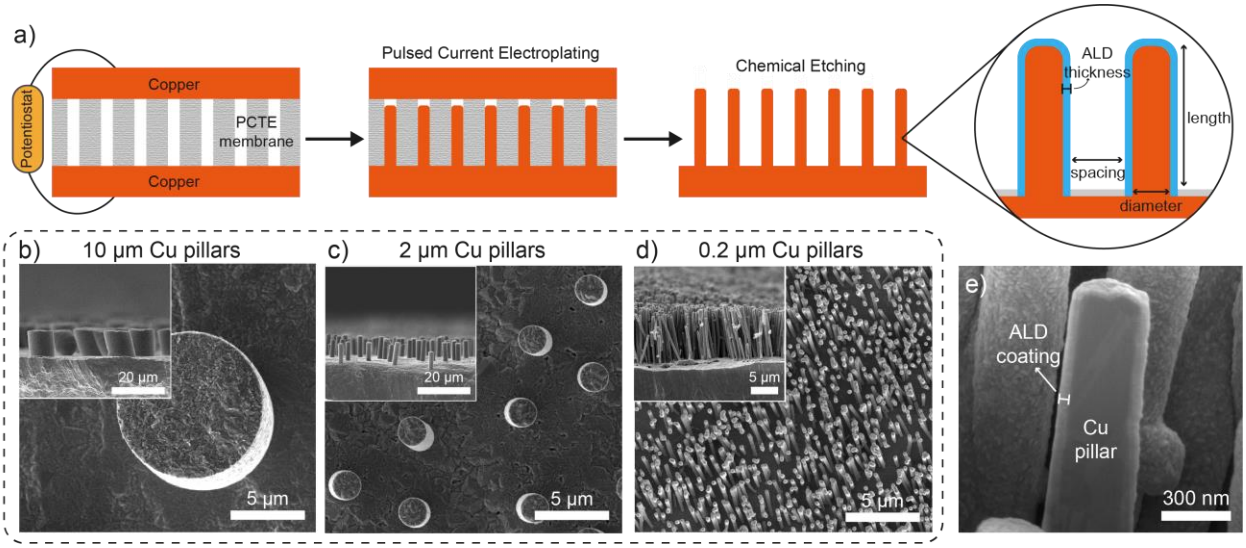

Figure 4.1. (a) Schematic illustration of the templated electrodeposition process for preparing Cu pillar arrays. Top-down and cross-section SEM images of the (b) 10 µm, (c) 2 µm, and (d) 0.2 µm Cu pillars. (e) Cross-section FIB-SEM image of the core-shell ALD-coated Cu pillar structure.

Unlike randomly textured synthesis methods, templated electrodeposition allows for facile tuning of pillar diameter, spacing, and length across length scales from 50 nm to 50 µm. This allows for rational design of current collector geometry, which can be used to identify tradeoffs between pore volume and spacing, electro-active surface area, electric field localization, and other geometric parameters, all of which affect Li metal morphology. In addition, the templated electrodeposition process can be applied over large areas, while at the same time maintaining high-throughput and cost-effective manufacturing. The compatibility with battery-grade thin Cu foil (18 µm) is also demonstrated here, which suggests that this process can be adapted to large-scale battery manufacturing.

Although potentiostatic conditions are commonly used in templated electrodeposition, Cu pillar arrays plated under constant potential resulted in a relatively large dispersion in the pillar length (**Figure 4.2a**). This can be attributed to diffusion limitations into the pores of the PCTE membranes, making it difficult to control the local ion concentration.[120] Such a variation in pillar length is not favorable, as it may introduce spatial inhomogeneities in the electrochemical performance of Li plating/stripping, especially near the current collector-separator interface. To avoid this geometric variation, pulsed current electrodeposition was adopted instead, in which the current was periodically interrupted to relax concentration gradients during the plating process.[120] By carefully tuning electrodeposition parameters, Cu pillar arrays with highly uniform length can be achieved (**Figure 4.2b**).

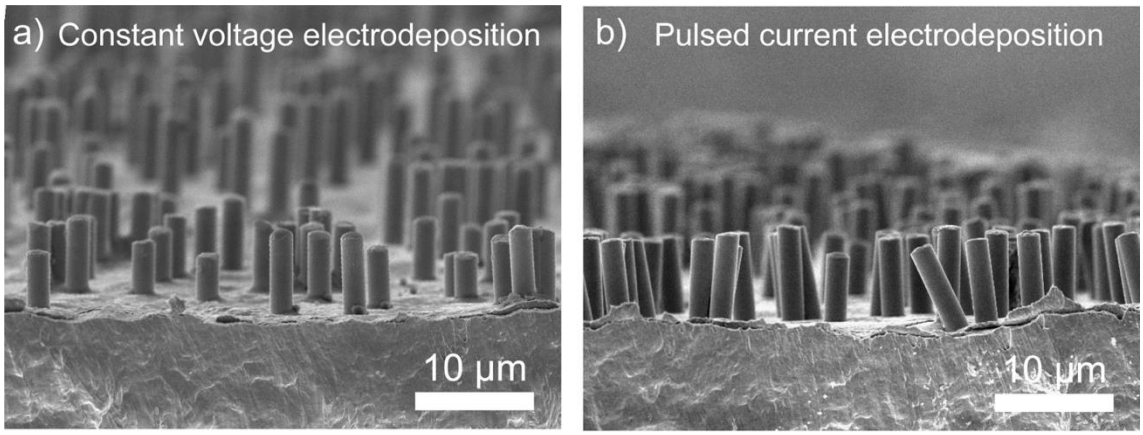

Figure 4.2. Cross-sectional SEM images of the 2 μm Cu pillars prepared using (a) constant voltage electrodeposition and (b) pulsed current electrodeposition.

Additional geometric parameters, including pillar diameter and pore spacing, can be rationally controlled through selection of the appropriate PCTE template. The pillar length is determined by the membrane thickness and/or the electroplating time duration. To demonstrate the tunable design of Cu pillar arrays as current collectors, PCTE membranes with pore diameters of 10 μm, 2 μm, and 0.2 μm were used in this work. The surface porosity (open area) of all membranes was fixed at 8% ± 2%, and the resulting Cu pillar length was initially controlled to be 10 μm ± 0.5 μm. **Figure 4.1b-d** show the SEM images of 10 μm, 2 μm, and 0.2 μm Cu pillar arrays, respectively. The cross-sectional SEM images indicate the good vertical alignment of the

Cu pillars on the planar Cu foil. Grazing incidence X-ray diffraction (GIXRD) analysis verified that the Cu pillars were crystalline without any traces of impurities (**Figure 4.3**).

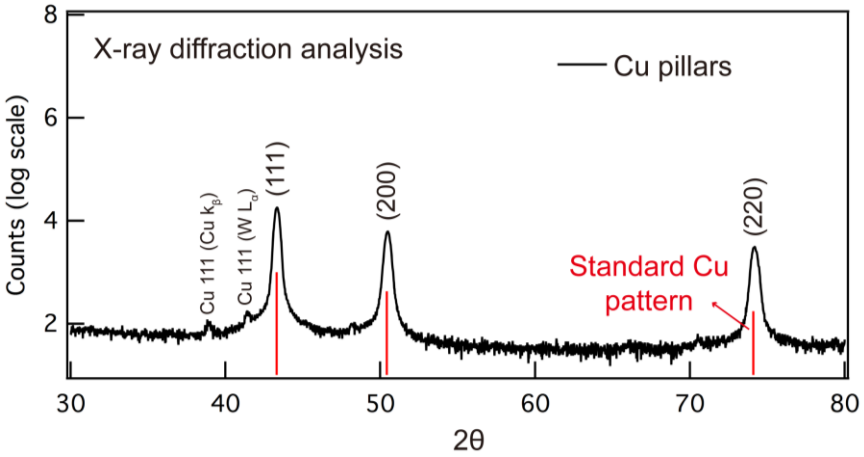

Figure 4.3. X-ray diffraction pattern of the electroplated Cu pillars showing crystalline Cu peaks.

4.1.2 Morphology analysis during Li plating and stripping

To investigate the behavior of Li plating/stripping on planar and 3-D Cu current collectors, Li-Cu cells were assembled and cycled galvanostatically at a current density of 1 mA/cm^2. 1M lithium bis(trifluoromethanesulfonyl)imide (LiTFSI) in 1/1 1,2-dimethoxyethane (DME)/1,3-dioxolane (DOL) with 1% lithium nitrate ($LiNO_3$) was used as the electrolyte. Cu pillars with diameters of 0.2 μm, 2 μm, and 10 μm were systematically studied. Since both the surface porosity of the membrane (8%) and pillar length (10 μm) were fixed, the available open volume for Li deposition was essentially identical for all three geometries, allowing for up to 2 mAh/cm^2 to be deposited within the open volume. Owing to the constant surface porosity, the average spacing between each pillar was fixed at ~2.5 times larger than the given pillar diameter (e.g. 2 μm pillar arrays have an average pore spacing of 5 μm).

Figure 4.4a-c shows the morphology of Li plating/stripping on a planar Cu electrode at various points in the cycle. After 0.5 mAh/cm^2 of Li deposition, spherical Li deposits with varying sizes were observed on the planar Cu surface with a non-uniform surface coverage (**Figure 4.4a**). This morphology is often attributed to an inhomogeneous Li-ion flux along the planar Cu surface. After 1 mAh/cm^2 of Li plating, the Li deposits branched out as elongated and needle-like dendrites (**Figure 4.4b**). After Li stripping, a large amount of "dead Li" and SEI residue were found to

remain on the electrode surface (**Figure 4.4c**), which can be attributed to the incomplete dissolution of dendrite structures, leading to their detachment and electrical isolation from the electrode surface.[8]

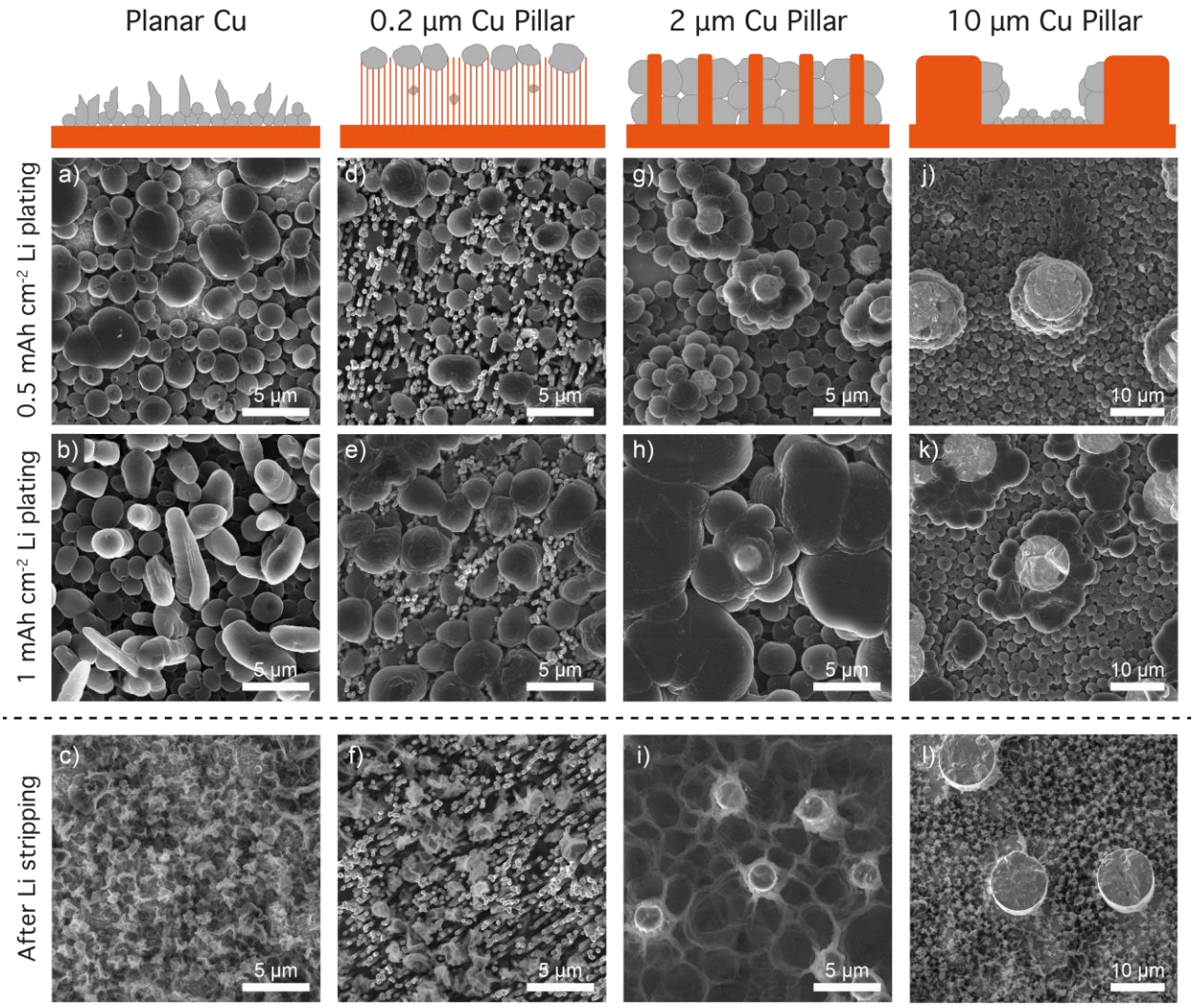

Figure 4.4. Schematics and SEM images of Li deposition and dissolution on the Cu current collectors. (a-c) planar Cu electrode, (d-f) 0.2 μm Cu pillars, (g-i) 2 μm Cu pillars, and (j-l) 10 μm Cu pillars upon 0.5 mAh/cm^2 of Li plating, 1 mAh/cm^2 of Li plating, and after Li stripping, respectively. The current density was fixed at 1 mA/cm^2.

In contrast, a drastically different Li morphology was observed on the 2 μm Cu pillar arrays (**Figure 4.4g-i**). Spherical Li deposits with identical size and uniform coverage over the whole electrode surface were observed upon 0.5 mAh/cm^2 of Li plating (**Figure 4.4g**). The improved Li morphology can be attributed to the reduced local current density and more homogeneous Li-ion

flux within the 3-D structure, which promoted uniform plating. Cross-sectional SEM analysis shows that the Li deposits filled into the void space between Cu pillars and deposited conformally along the side walls of the Cu pillars (**Figure 4.5**). Interestingly, these agglomerated deposits were confined to grow laterally within the pillar arrays rather than outward towards the counter electrode, which is another unique feature of the vertical pillar geometry. After 1 mAh/cm^2 of Li plating, Li spheres agglomerated and merged together as compact Li deposits (**Figure 4.4h**) with morphologies significantly different than the needle-like dendrites observed on planar Cu. As a result of a more compact morphology, less dead Li was observed after Li stripping (**Figure 4.4i**), exposing the clean Cu pillar surface. This reduction in dead Li indicates the 2 μm Cu diameter pillar arrays can improve the reversibility of cycling.

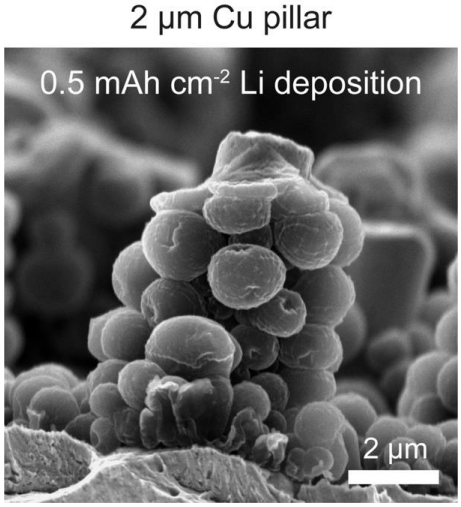

Figure 4.5. Cross-sectional SEM image of 2 μm Cu pillars upon 0.5 mAh/cm^2 of Li deposition (cross-sectional view of **Figure 4.4g**). The current density was fixed at 1 mA/cm^2.

To test the effect of further reducing the pillar diameter and spacing on Li deposition, 0.2 μm diameter Cu pillar arrays (with an average pore spacing of 0.5 μm) were used as a current collector. As shown in **Figure 4.4d**, Li deposits appear to grow on top of the pillar arrays rather than within the 3-D structure. Cross-sectional SEM analysis (**Figure 4.6**) confirmed that the deposits were almost exclusively formed on top of the pillars. After 1 mAh/cm^2 of Li plating, Li deposits continued to grow into larger spheres (**Figure 4.4e**). Three possible mechanisms can simultaneously contribute to this phenomenon, described below.

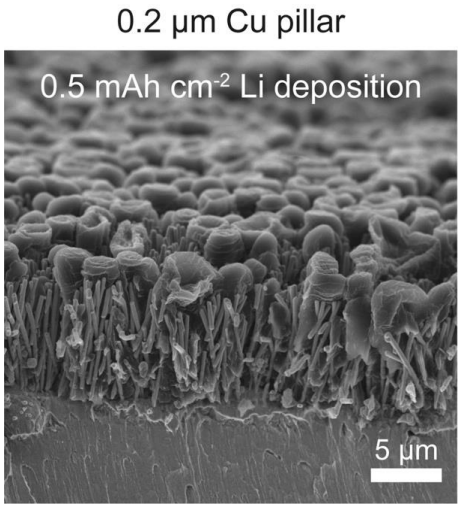

Figure 4.6. Cross-sectional SEM image of 0.2 μm Cu pillars upon 0.5 mAh/cm^2 of Li deposition (cross-sectional view of **Figure 4.4d**). The current density was fixed at 1 mA/cm^2.

First, the 0.2 μm pillar sample has an increase in electrode surface area by a factor of 10x compared to the 2 μm pillar geometry. This will reduce the local current density along the Cu pillar surface. It has been previously proposed that continually increasing surface area can promote an improved morphology. However, in the case of a planar Cu current collector, it has also been shown that decreasing current density favors more sparse nucleation and growth of larger diameter Li deposits to a lower driving force for nucleation at low current densities.[121] Therefore, since the pore spacing between the 0.2 μm pillar diameter arrays (0.5 μm) is well below the observed diameter of the plated Li deposits (> 1 μm)[121], this indicates that growth of initial nuclei on the top surface is favored compared to that of nuclei confined within the void space between pillars. This also illustrates the value of rational design of a 3-D current collector architecture, as increasing surface area and decreasing pore spacing can lead to competing effects.

Second, the 0.2 μm Cu pillars have an aspect ratio of 50, which can cause significant current focusing at the tips of the pillars, further promoting preferential nucleation at the top of the array. Third, the narrow and long void space can introduce diffusion limitations during plating. As the Li-ion concentration depletes toward the bottom of the pores, local Li deposition is suppressed.

As a consequence of both of these additional effects, the local current density at the tips is higher than along the sidewalls. Both of these two additional factors will couple with the first mechanism and further exacerbate the Li deposition on the top surface instead of within the 3-D structure. Combining these three mechanisms, we can conclude that:

(1) Nucleation density is a function of local current density.
(2) Larger deposits that would normally grow at lower current densities are constrained by the small pore diameter, suppressing their growth.
(3) Owing to the high aspect-ratio of the 0.2 μm pillars, the local current density is higher at the top of the electrode, enhancing Li nucleation and growth.

After stripping the Li deposited on the top surface of the 0.2 μm pillars, significantly more dead Li was observed, compared to the 2 μm geometry (**Figure 4.4f**). This illustrates the importance of optimizing the nucleation kinetics along the entire active surface of a 3-D current collector to facilitate reversible plating within the 3-D geometry. Furthermore, since these surface and volume effects are both dependent on geometry, this also motivates the ability to decouple surface kinetics from the geometric architecture, which will be demonstrated later in this chapter through the use of ALD surface modification.

To study the impact of increasing pillar diameter and pore spacing, Li plating was also tested on Cu pillars with a 10 μm diameter and an average pore spacing of 25 μm. Upon 0.5 mAh/cm^2 of Li plating, spherical Li deposits appear to uniformly cover the entire electrode surface (**Figure 4.4j**). As the deposition proceeded (1 mAh/cm^2), Li deposits agglomerated around the Cu pillars (**Figure 4.4k**). However, owing to the wide pore spacing between Cu pillars, Li deposition failed to merge into a compact layer. In particular, a significant fraction of Li plated on the bottom surface of the electrode, resembling the morphology of the planar electrode. After stripping, a large amount of dead Li was still observed, along the bottom surface (**Figure 4.4l**). This suggests that with increasing pore spacing, a significant fraction of the current collector surface resembles a planar electrode. It is therefore important to engineer the pillar spacing and electrode surface area to facilitate merging of larger Li deposits within the pore volume.

This knowledge gained from the highly ordered model system of vertical pillars provides valuable insight into the rational design of 3-D current collectors, which may also take alternate geometric form factors. For example, in this study, the total pore volume was maintained as a constant, allowing us to focus on the impact of varying electrode geometry for a fixed total volumetric capacity of the electrode. However, further optimization based on these observed trends can be applied to alternate geometries, depending on the battery application desired.

Another significant and unique benefit of the highly uniform vertical pillar geometry was the observation that despite the potential for strong electric field localization near the top surface

of the pillars, no Li deposition occurred on the pillar tips for the 2 and 10 μm diameter samples (**Figure 4.4g-l**). Instead, the Li deposition on the pillar surfaces occurred exclusively along their sidewalls.

A potential explanation for this phenomenon is that the separator is mechanically deformed when sandwiched against the Cu pillars, effectively masking off the top portion of the pillars from electrolyte. In other words, highly localized compressive strains can develop in the polymer separators as they deform around the pillar tips, which will likely reduce their local porosity. This reduction in local porosity can in turn limit the exposure of electrolyte to the top surface of the pillars and reduce the local ionic flux at the pillar tips during cycling. As the current will follow the path of least resistance, this would promote growth along the pillar sidewalls, which are not in contact with the separator.

To further support this hypothesis, a cell was assembled without a separator using the 2 μm diameter geometry. The SEM analysis shows that without the presence of the separator, Li deposition occurs uniformly along the Cu pillar surface, including the tops of the pillars (**Figure 4.7**), demonstrating the role of local compressive contact with the separator on protecting the tips.

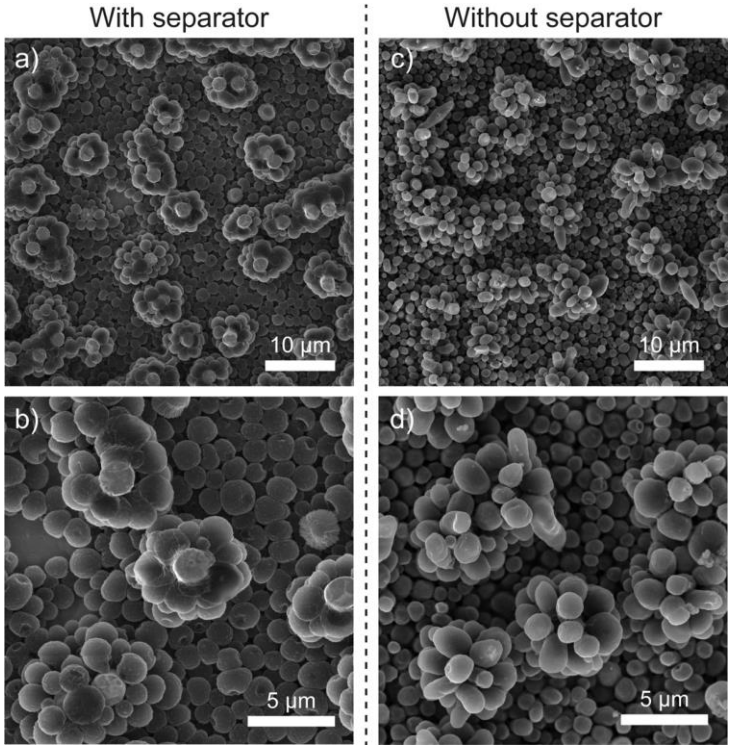

Figure 4.7. SEM morphology study of Li deposition on the 2 μm Cu pillars (a, b) with and (c, d) without the presence of the polymer separator.

The suppression of growth at the pillar tops is highly beneficial from a safety standpoint, as it reduces the probability of a catastrophic internal short circuit, which could otherwise be amplified by electric field focusing at vertical protrusions on a non-planar surface. Even if dendritic structures were to form, the growth of lateral structures within the pores would appear to drive them more towards compressive stress against nearest neighbor pillar sidewalls, leading to a more compact morphology as observed in the 2 μm diameter samples. In contrast, in highly disordered 3-D current collectors, including vertical pillars with non-uniform heights, this benefit would not be expected to play as significant of a role.

4.1.3 Electrochemical performance of Cu pillar arrays

To evaluate the cycling performance of the Cu pillar arrays, Li-Cu cells were assembled and characterized by their Coulombic efficiency (CE). A convenient method that is often used to determine the CE is to use exhaustive Li stripping for each cycle. In that approach, a given amount of Li is initially plated onto the Cu electrode (Q_P), followed by a stripping half cycle that ends when a cut-off voltage is reached (Q_S). This cut off indicates that all the removable Li has been stripped from the Cu surface.[122] While this method can provide a cycle-by-cycle efficiency (CE = $Q_S/Q_P \times 100\%$), the Li loss associated with side reactions between Li and Cu electrode cannot be avoided during Li deposition process. As a result, the measured CE is convoluted and highly dependent of the current collector material and surface conditions. Moreover, this method is not reflective of practical Li metal batteries that typically incorporate excess Li.

A more representative method of determining Li CE was proposed and systematically investigated by Adams et al.[122] In this method, the Cu electrode is first preconditioned with a single Li plating/stripping cycle, which leads to formation of a passivation layer that stabilizes the surface against further reaction with the Cu surface. Next, a Li reservoir (Q_T) is deposited, which is followed by several stripping/plating cycles with a fixed capacity of Li less than the initial Li reservoir ($Q_C < Q_T$). The remaining Li on the Cu electrode is then completely stripped to a cut-off voltage (Q_S). Using this protocol, an average value of CE can be determined using the following equation: $CE_{avg} = (nQ_C + Q_S) / (nQ_C + Q_T) \times 100\%$.[122] This method is more accurate since the initial surface passivation cycle reduces effects from initial side reactions between Li and Cu, and

it better reflects practical Li metal battery designs, in which a limited amount of excess Li is always present to account for Li loss during cycling.[123]

Using the method described above, the electrochemical performance of planar Cu and 3-D current collectors were compared. Specifically, the Cu electrodes were first conditioned by plating 2 mAh/cm^2 of Li and then stripping the deposit until a cut-off voltage of 0.5 V was reached. A Li reservoir of 2 mAh/cm^2 (Q_T) was then deposited on the Cu electrodes, followed by cycling for 10 cycles with a depth of discharge of 1 mAh/cm^2 (Q_C). The Li was then fully stripped from the Cu until the voltage reached the cutoff of 0.5 V to determine Q_S and the average CE (**Figure 4.8a**). In addition, long-term cycling was carried out to quantify the cycling lifetime (**Figure 4.8b**). It is noted that a fixed current density (e.g. 1 mA/cm^2) was applied throughout the cycling to ensure a consistent CE measurement.

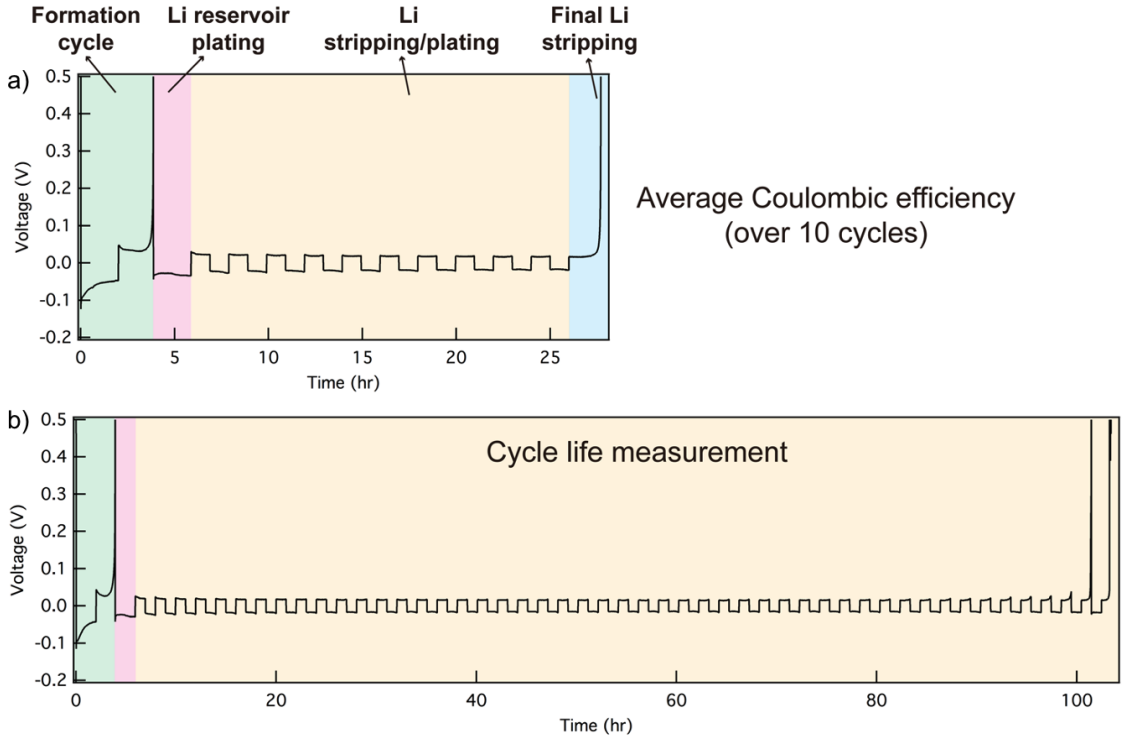

Figure 4.8. Voltage profiles of (a) average Coulombic efficiency measurement and (c) cycle life measurement. The formation cycle (green), Li reservoir plating (red), Li stripping/plating (yellow), and final Li stripping (blue) steps are highlighted in the figure. A fixed current density was applied throughout the cycling to ensure an accurate measurement.

Figure 4.9a shows the galvanostatic cycling of Li-Cu cells with 0.2 μm, 2 μm, and 10 μm Cu pillar arrays at a current density of 1 mA/cm^2. The cells were cycled until cell failure occurred, which is signified by a sharp increase in cell polarization. The 3-D current collectors all displayed an improved cycle life when compared to the planar Cu sample. However, the best performance was exhibited by the 2 μm Cu pillar arrays that had a cycle life of > 100 hr (50 cycles). This is almost double the cycle life of the planar specimen (60 hr; 28 cycles).

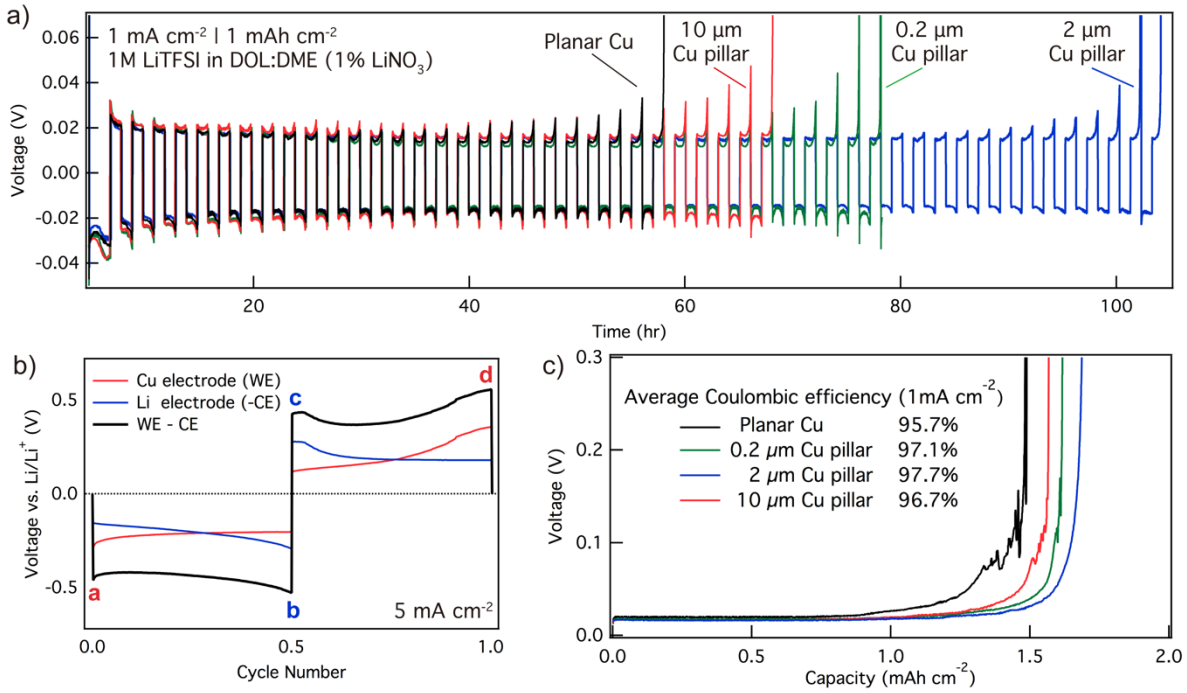

Figure 4.9. (a) Galvanostatic cycling of Li-Cu cells at 1 mA/cm^2 for 1 mAh/cm^2 on the planar Cu and Cu pillars of 0.2 μm, 2 μm, 10 μm diameters. (b) Three-electrode measurements showing the cell polarization contributions from the Cu working electrode and Li counter electrode. Counter electrode voltage has been inverted for visual clarity. (c) Voltage profile of the last Li dissolution from Cu showing remaining capacity after 10 cycles of Li stripping/plating. The average Coulombic efficiency for each configuration is provided in the inset.

To better understand the observed voltage variations during cell cycling and the failure mechanism, three-electrode measurements were performed to decouple the voltage contributions from Li and Cu electrode. **Figure 4.9b** shows the overall voltage profile of a full cycle (black) and the decoupled voltage traces from the Cu working electrode (red) and Li counter electrode (blue). It is clear that the initial peak in the first half cycle (peak a) can be attributed to Li nucleation

overpotential on the Cu electrode, whereas the peak toward the end of the second half cycle (peak d) was associated with stripping Li from Cu.[42]

Since the Li reservoir on the Cu current collector was continuously consumed during cycling as a result of the imperfect CE, the amount of available Li was gradually depleted at later cycles. A sharp increase in overpotential (trend in peak d in **Figure 4.9a**) was observed as a result of Li depletion on the Cu current collector, which was defined as the failure point to determine cycle lifetime. Similarly, as Li depletion on the Cu electrode progresses with each cycle, new Li deposits in the subsequent plating cycle must nucleate on the Cu surface to a greater and greater extent rather than grow on any residual Li. Consequently, a higher nucleation overpotential (peak a) was also observed as complete depletion of the plated Li is approached and the experiment is terminated. On the other hand, peak b and c can be attributed to the Li electrodissolution (peak b) and deposition (peak c) on the Li metal counter electrode.[42] Because an effectively "infinite" amount of excess Li was present, Li plating/stripping on the Li metal electrode exhibited a very stable cell polarization throughout the cycling (**Figure 4.9a**).

The three-electrode measurements confirm that the failure mode is due to Li depletion on the Cu current collector as a result of the continuous Li consumption during Li plating/stripping process. The poor performance of the planar Cu is therefore attributed to an undesirable Li deposition morphology causing excessive SEI and dead Li formation, which results in early depletion of the Li reservoir. On the other hand, the improved cycle life of the 2 μm Cu pillar arrays can be explained by the growth of agglomerated and compact Li deposits, which minimizes the formation of SEI and dead Li during cycling.

To quantify the average CE of the current collectors, a full strip after 10 cycles was performed respectively (**Figure 4.9c**). Under a current density of 1 mA/cm^2, the average CEs were: 95.7% for the planar Cu current collector; 96.7% for the 10 μm pillars, and 97.7% for the 2 μm Cu pillars and 97.1% for the 0.2 μm Cu pillars (**Figure 4.9c**).

The morphological and electrochemical analysis above demonstrate the impact of the rational design of 3-D current collector structures. By controlling geometric parameters, the Li morphology upon plating/stripping can be greatly modulated, which significantly affects the cycling efficiency and lifetime. It is shown that vertically-aligned Cu pillar arrays with adequate pore spacing (~5 μm) to accommodate the Li deposits exhibited improved performance compared to current collectors with either greater or smaller pillar spacing, as well as the planar Cu current

collector. The need for rational design in an ordered model system rather than using random and disordered structures as current collector is thus warranted. This also indicates a very important point that while several works have demonstrated enhanced performance of porous nanostructures, the geometries may not comprise the optimal dimensions.

4.1.4 Tuning interfacial chemistry by ALD surface modification

While the above analysis shows that using Cu pillar arrays as a current collector can boost the cycling efficiency and lifetime, there still exists a large nucleation peak during the initial Li deposition, indicating a substantial nucleation barrier (**Figure 4.10a**). This barrier represents the thermodynamic cost of forming critical Li nuclei, which is governed by the interfacial energy between the Cu current collector and Li metal. A recent study by Yan et al. reported that while some materials exhibit large nucleation overpotential upon Li deposition (Cu, Ni, C, etc.), others show a nucleation overpotential of nearly zero (Au, Ag, Zn, etc.).[124] The absence of a nucleation overpotential has been attributed to the reactions of "lithiophilic" materials with Li metal to form a buffer layer consisting of alloys and solid solution phases at the interphase of the substrate and the pure Li phase, which can eliminate nucleation barriers upon Li deposition.

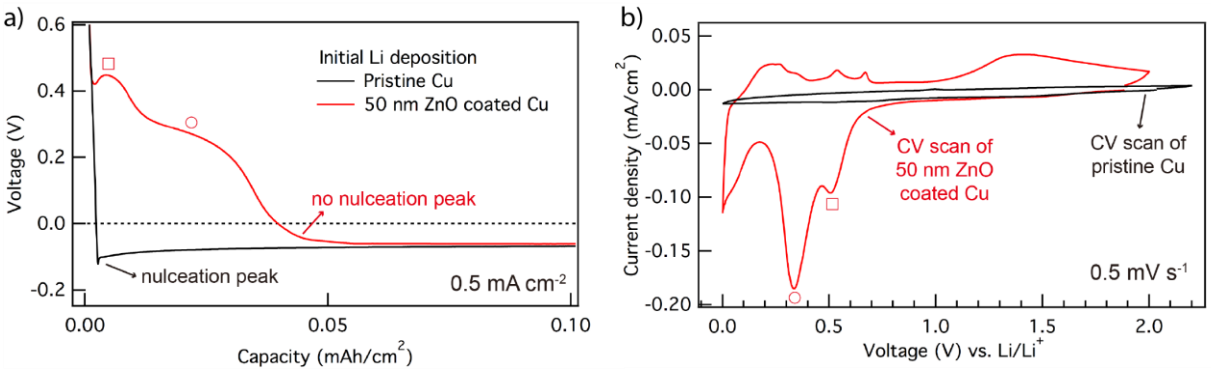

Figure 4.10. (a) Voltage profiles of the pristine and ALD ZnO coated planar Cu during initial Li deposition at 0.5 mA/cm^2. (b) Cyclic voltammetry scans of the pristine and ALD ZnO coated planar Cu at a scan rate of 0.5 mV/s.

In this work, we further apply this concept to modify the surface of the Cu pillar arrays to tune the interfacial chemistry. It is worth noting that while a few reports have previously explored surface modification of 3-D current collectors[114,125–128], the role of geometry and surface

chemistry in 3-D geometries has not been systematically decoupled and studied. This is partially due to the difficulty of applying a conformal coating over the porous microstructure surfaces in a controllable manner while preserving the 3-D structure. In order to address this issue, we used ALD to deposit a conformal coating on the surface of the Cu pillar arrays. ALD is a thin film deposition technique comprised of gas-phase surface reactions that are cyclically repeated to build up a uniform, conformal, and pinhole-free thin film.[129,130] Owing to its vapor phase precursors and self-limiting chemistry, ALD can deposit highly conformal thin films on high-aspect-ratio substrates with sub-nanometer thickness control.[131,132] Recent progress has demonstrated using ALD to deposit thin protection layers directly on Li metal anode surfaces can improve the cycling performance.[63–65] However, a systematic study of the CE of Li electrodeposition on ALD-modified planar and 3-D current collector architectures with rationally-controlled geometric parameters is lacking, which is necessary to decouple the roles of geometry and surface chemistry on Li plating morphology and reversibility.

In this study, ZnO is chosen as the coating material because the electrochemical reaction of ZnO upon lithiation results in the formation of Li_xZn alloy, which can serve as the buffer layer for the subsequent Li deposition. Previous research efforts have shown that the lithiation reactions of ZnO can be described as a two-step process involving a conversion reaction followed by alloying:[133–135]

$$ZnO + 2Li \leftrightarrow Zn + Li_2O \quad (13)$$

$$Zn + xLi \leftrightarrow Li_xZn \ (x \leq 1) \quad (14)$$

To test the electrochemical stability of the ALD ZnO, a thin layer of 50 nm ZnO was first deposited onto a planar Cu electrode. Cyclic voltammetry (CV) measurements were then performed in a potential window of 0-2 V (vs. Li/Li^+). **Figure 4.10b** shows the CV curve of the first scan. The initial cathodic sweep of the CV exhibited two characteristic peaks at 0.5 V and 0.33 V, which represent the conversion reaction where the ZnO is reduced by Li to form elemental Zn and Li_2O and the alloying reaction between Li and Zn.[136] Similarly, during the anodic sweep, the multi-step dealloying process of the Li_xZn alloy was represented by peaks between 0.25-0.65 V, whereas the peak centered at 1.4 V has been associated with the reformation of ZnO.[136,137] To further verify the effect of the ALD ZnO coating, a CV measurement was also performed using a pristine Cu electrode. As shown in **Figure 4.10b**, no characteristic peak was observed throughout the CV scan, suggesting no electrochemical reaction occurred on the pristine Cu surface.

Figure 4.10a further shows the voltage profile of ALD ZnO coated Cu electrode upon Li deposition under a current density of 0.5 mA/cm^2. Two characteristic plateaus are present in the voltage profile, which match the peaks observed in the CV cathodic scan. Upon further Li deposition, a smooth voltage trace was observed, without the presence of the nucleation peak that occurred on the pristine Cu (**Figure 4.10a**). This suggests that the Li nucleation overpotential on ALD ZnO is essentially zero. Therefore, even an ultrathin layer (50 nm) of ZnO on the Cu current collector can significantly change the interfacial chemistry. The formation of Li_xZn alloy during lithiation reactions of ALD ZnO can serve as a "buffer layer" to facilitate the subsequent Li nucleation and deposition on top of the ZnO surface once it is fully lithiated. XPS analysis was further performed to show that the plated Li formed on top of the buffer layer, without the presence of measurable Zn on the plated Li surface (**Figure 4.11**). Therefore, we show that the mechanism of the ZnO buffer layer is to facilitate an initially homogeneous Li flux into the ALD film, followed by subsequent Li plating on the fully-lithiated ZnO surface.

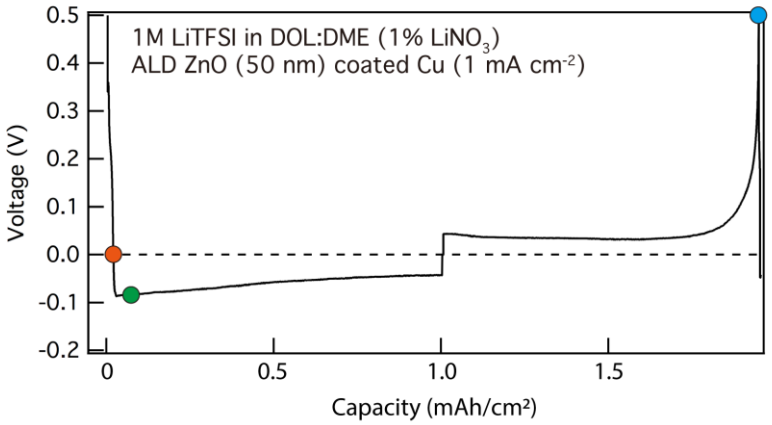

	Zn [%]	Li [%]	O [%]	C [%]
Lithiated to 0 V	3.4	55.4	34.4	3.6
Plated 0.1 mAh/cm² Li	0.0	58.7	26.7	3.7
Stripped to 0.5 V	1.3	54.8	32.7	5.7

10 min Ar sputter to remove adventitious film

Figure 4.11. XPS analysis of ALD ZnO coated planar Cu upon lithiation to 0 V (orange), 0.1 mAh/cm^2 of Li deposition (green), and Li stripping to 0.5 V (blue). Table of survey spectra quantification showing the presence of Zn upon lithiation to 0 V and after stripping, but no Zn signal was detected after 0.1 mAh/cm^2 of Li plating, suggesting Li plating occurred on top of the buffer layer.

To demonstrate the capability of ALD to deposit conformal films on the 3-D pillar geometry, 50 nm ZnO was deposited on the 0.2 μm arrays. As shown in **Figure 4.12a**, a conformal ZnO thin film with nanocrystalline grains from the as-deposited ZnO can be clearly observed. More importantly, the ALD coating perfectly preserve the pillar architecture, which allows for the geometry and surface chemistry to be decoupled and individually controlled to optimize the electrochemical performance. Transmission electron microscopy (TEM) analysis further confirmed the uniform thickness and core-shell geometry of the ALD film on the pillar surface (**Figure 4.12b**).

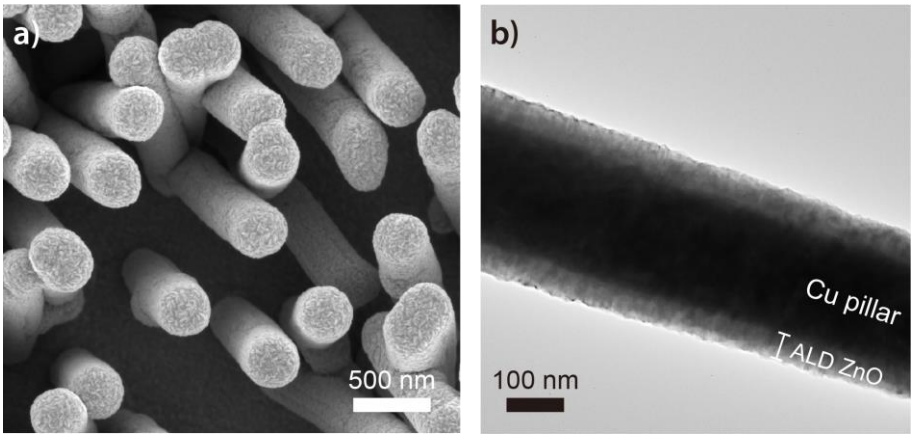

Figure 4.12. (g) SEM image of ALD-coated Cu pillars showing nanocrystalline ZnO grains. (h) TEM image showing the conformal ZnO coating (50 nm) on the 200 nm Cu pillar.

4.1.5 ALD surface-modified Cu pillar arrays during Li plating/stripping

To investigate the behavior of Li plating/stripping on ALD ZnO coated current collectors, Li-Cu cells were cycled galvanostatically at a current density of 1 mA/cm^2. A dramatically different Li morphology is observed when the planar current collector is coated with ALD ZnO (**Figure 4.13a-c**). Upon 0.5 mAh/cm^2 of Li plating, significantly larger Li deposits are formed on the electrode and packed in a more compact manner (**Figure 4.13a**). Further deposition (1 mAh/cm^2) leads to compact and agglomerated Li spheres without any trace of dendritic structures (**Figure 4.13b**). After Li stripping, a much "cleaner" electrode surface is revealed, indicating improved cycling reversibility and less dead Li formation. These results suggest that an ultrathin

thin layer of ZnO can effectively facilitate the initial Li nucleation, producing morphologies better suited for cycling.

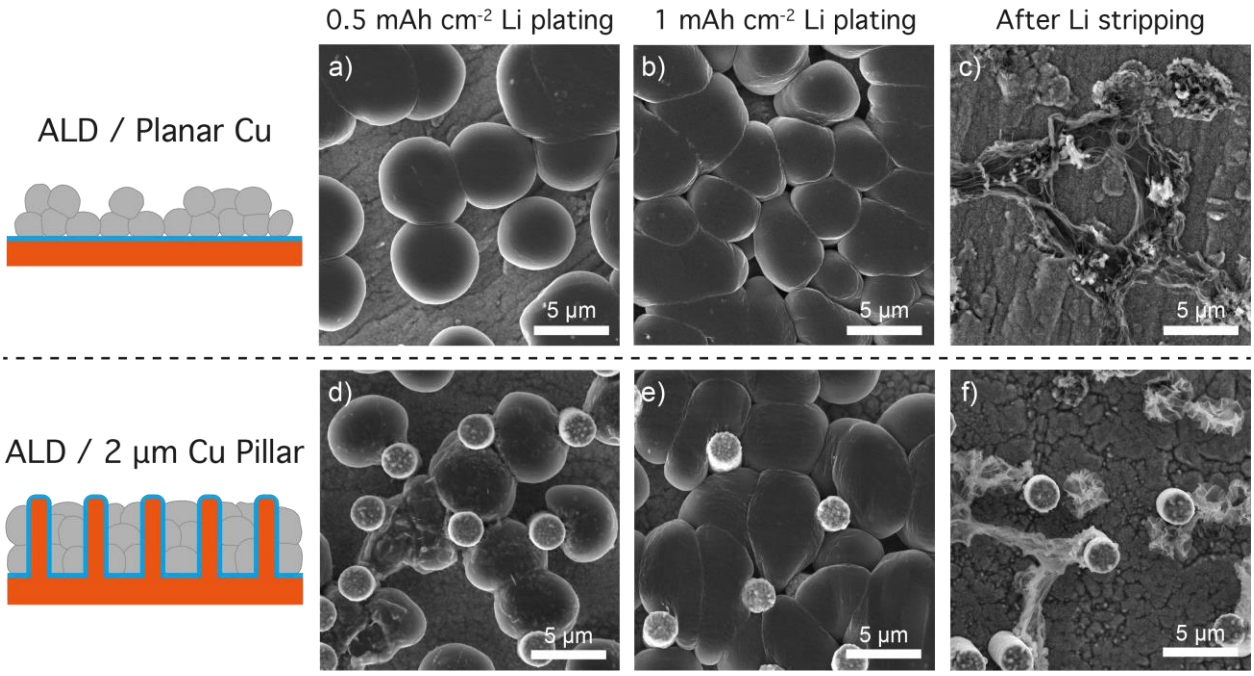

Figure 4.13. SEM analysis of (a-c) ALD-coated planar Cu and (d-f) ALD-coated 2 µm Cu pillars upon 0.5 mAh/cm^2 Li plating, 1 mAh/cm^2 Li plating, and after Li stripping. The current density was fixed at 1 mA/cm^2.

Figure 4.13d-f further shows the synergistic effect of ALD coating on the 2 µm Cu pillars during cycling. Larger Li deposits are again observed during Li deposition and also confined to grow within the void space between pillars, without coating the pillar tops (**Figure 4.13d-e**). After stripping, significantly less dead Li remained on the electrode surface (**Figure 4.13f**) than in the uncoated pillars (**Figure 4.4i**).

It is also noted that while Li deposition mainly occurred on top of the pristine 0.2 µm Cu pillars, ALD coated 0.2 µm pillars exhibited a dramatically different morphology, where the Li deposits appear to grow within the 3-D structure (**Figure 4.14**). This further demonstrates the importance of decoupling electrode geometry and surface chemistry effects on morphology and cycling in order to rationally design 3-D current collector architectures.

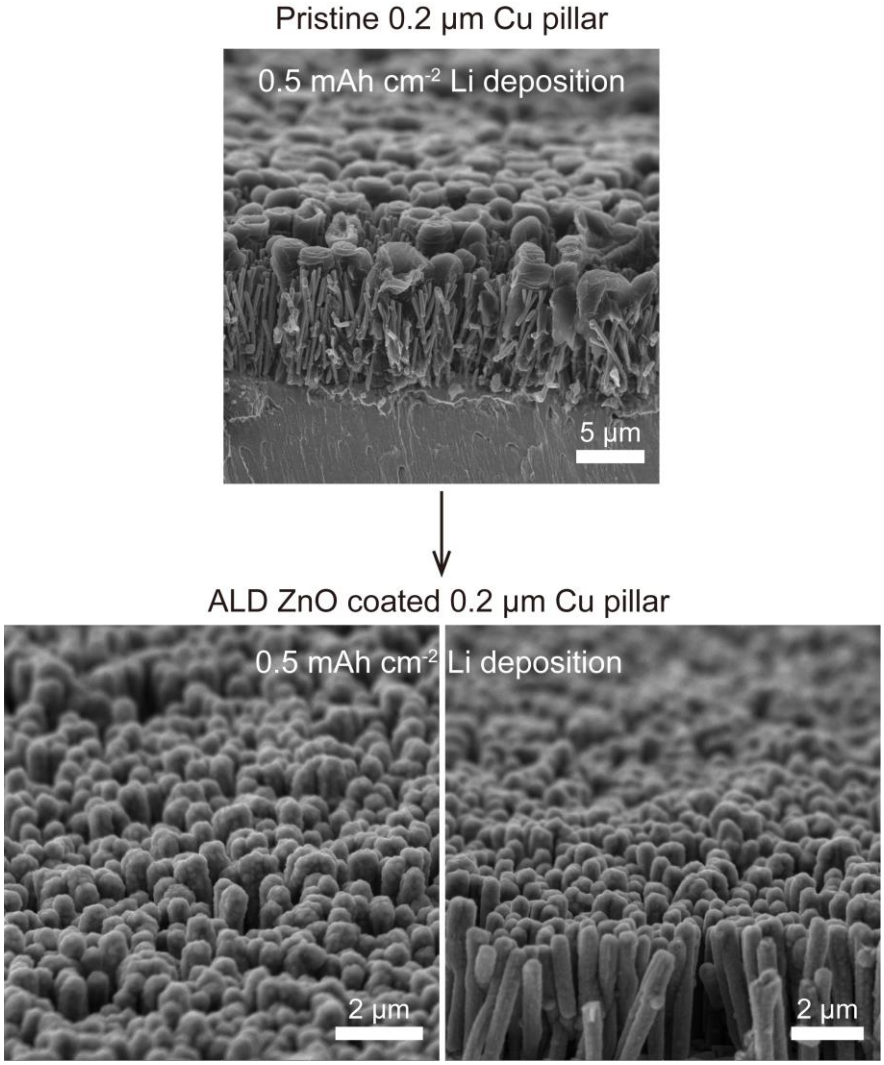

Figure 4.14. Cross-sectional SEM images of pristine and ALD ZnO coated 0.2 μm Cu pillars upon 0.5 mAh/cm^2 of Li deposition. The current density was fixed at 1 mA/cm^2. Li deposition was found to occur within the ZnO coated pillar arrays, suggesting the ALD coating can guide the Li plating into the 3-D structures.

4.1.6 Electrochemical performance of ALD surface-modified Cu pillar arrays

To demonstrate the synergistic effect of the ALD surface modification and 3-D geometry on electrochemical performance, Li-Cu cells with ALD coated planar Cu and 2 μm Cu pillar arrays were assembled and cycled. ZnO films of 10, 20, 50, and 100 nm were first deposited onto a planar Cu electrode and cycled to measure efficiency and cycle life (**Figure 4.15**). Similar cycling lifetimes and average CEs were obtained regardless of the varying ALD thickness. Therefore, 50

nm of ALD ZnO was chosen as the surface modification for further experiments using ALD coated pillar arrays.

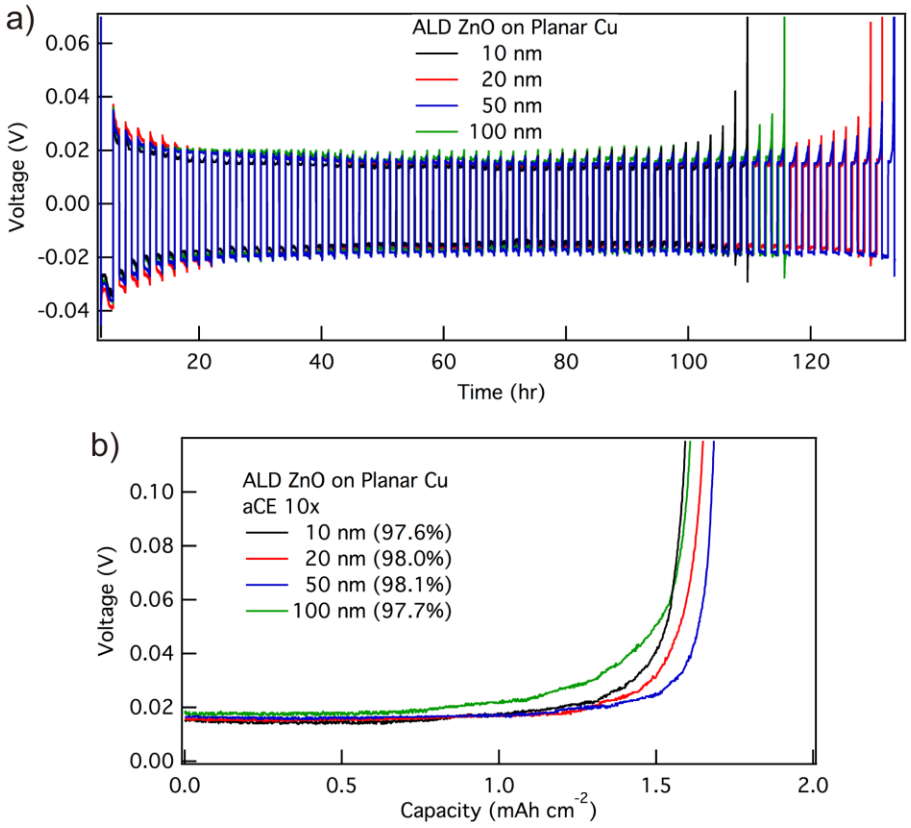

Figure 4.15. (a) Cycle life measurements of ALD coated planar Cu with 10 nm, 20 nm, 50 nm, and 100 nm of ZnO coating. (b) Corresponding average Coulombic efficiency measurements over 10 cycles. The current density was 1 mA/cm^2.

Figure 4.16a shows the voltage profiles of planar Cu, 2 μm pillars, ALD/planar Cu, and ALD/2 μm pillars upon cycling at a current density of 1 mA/cm^2. With the ALD ZnO surface treatment on the planar Cu, the cell exhibited stable cycling up to 120 hr (59 cycles), doubling the cycle life of pristine planar Cu (60 hr; 28 cycles). Furthermore, with the synergistic effect of ALD surface modification and optimized 2 μm pillar array structure, the cycling lifetime can be tripled (> 180 hr; 91 cycles).

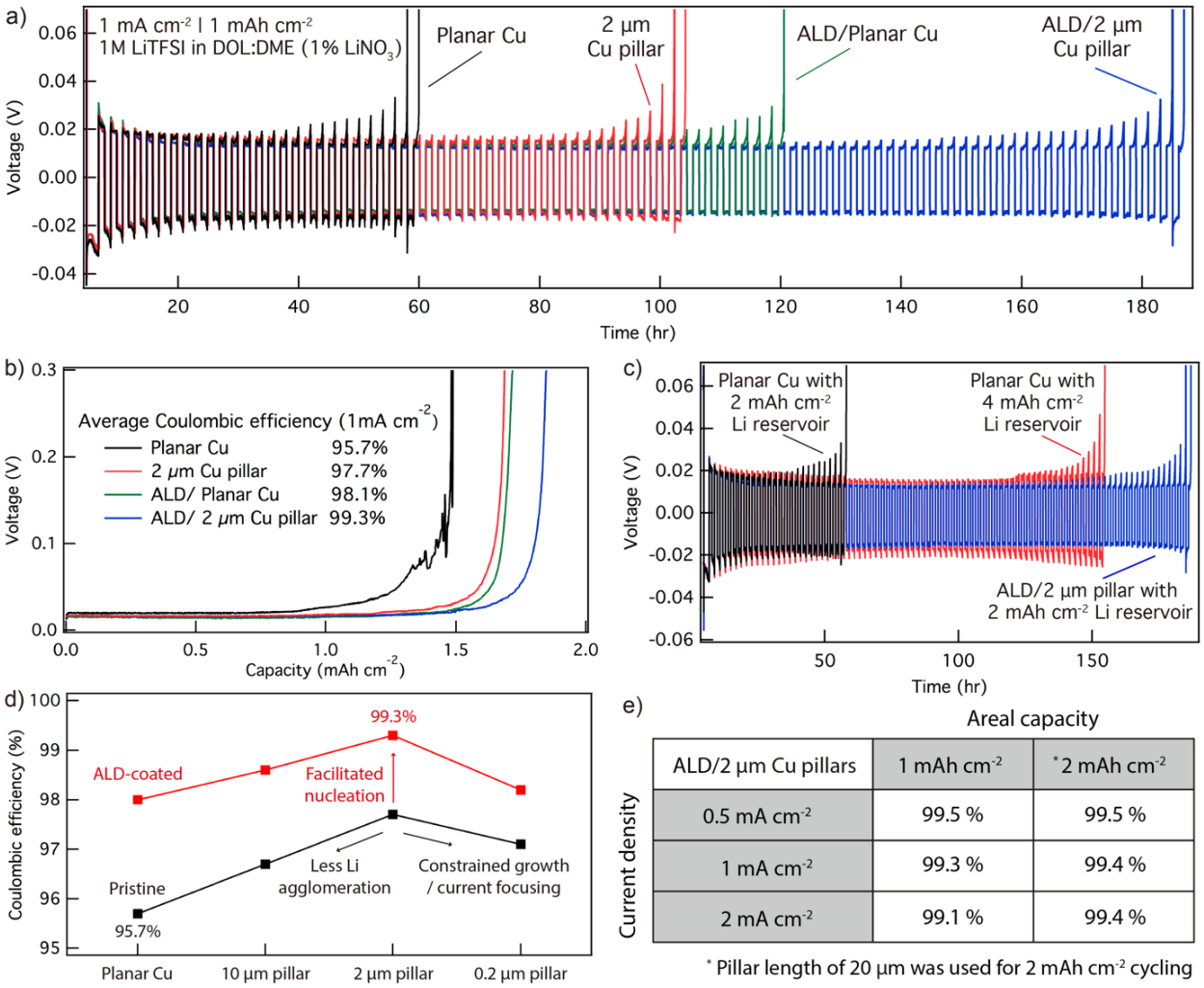

ALD/2 µm Cu pillars	1 mAh cm^{-2}	*2 mAh cm^{-2}
0.5 mA cm^{-2}	99.5 %	99.5 %
1 mA cm^{-2}	99.3 %	99.4 %
2 mA cm^{-2}	99.1 %	99.4 %

* Pillar length of 20 µm was used for 2 mAh cm^{-2} cycling

Figure 4.16. (a) Cycling performance and (b) average Coulombic efficiency of the pristine and ALD-coated planar Cu and 2 µm Cu pillars at 1 mA/cm^2 for 1 mAh/cm^2. (c) Cycling performance of the planar Cu (black) and ALD-coated 2 µm Cu pillars (blue) with a Li reservoir of 2 mAh/cm^2 and the planar Cu with a Li reservoir of 4 mAh/cm^2 (red). (d) Coulombic efficiency plot for both pristine and ALD-coated pillar arrays at 1 mA/cm^2 and 1 mAh/cm^2. (e) Average Coulombic efficiency of ALD-coated 2 µm pillar arrays under varying current densities and areal capacities.

Average CE measurements were also performed (**Figure 4.16b**). While the pristine planar Cu exhibited a low CE of 95.7%, an enhancement to 98.1% was observed with the addition of an ALD ZnO surface coating. Moreover, when the ALD ZnO coating was applied to 2 µm pillar arrays, a CE as high as 99.3% was achieved with a current density of 1 mA/cm^2 (**Figure 4.16b**). It is noted that ALD-coated 0.2 µm and 10 µm pillar arrays also displayed improved performance compared to uncoated pillars, yet the 2 µm pillar diameter remained the optimal geometry. The

Coulombic efficiency values for both pristine and ALD-coated pillar arrays are further summarized in **Figure 4.16d**.

Stable Li plating/stripping with higher per-cycle areal capacity can also be achieved through increasing the length of the Cu pillar arrays (**Figure 4.17**). Increasing length, while maintaining the same diameter and spacing of the template allows us to increase the total capacity of the electrode, and therefore cycle a larger volume of Li per cycle. **Figure 4.16e** summarizes the average Coulombic efficiency values of the ALD/2 μm pillars under varying current densities and areal capacities. As shown, increasing the pillar length (and therefore enabling larger depth of discharge) further increased the CE to 99.4% at 1 mA/cm^2 and 2 mA/cm^2 at 2 mAh/cm^2. These values are among the highest reported values in the literature, illustrating the benefits of the 3-D pillar architecture and ALD surface modification to systematically design optimized electrodes.

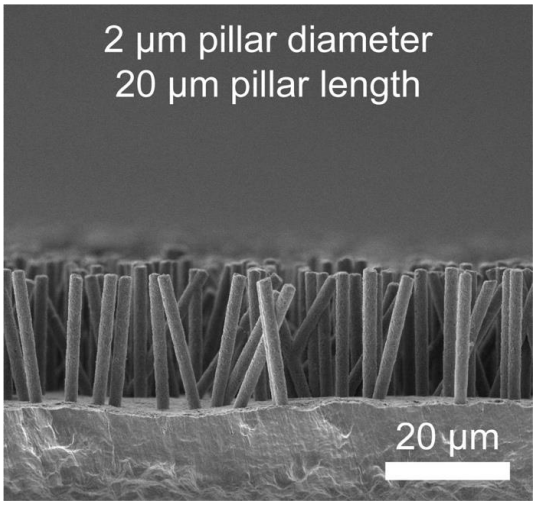

Figure 4.17. Cross-sectional SEM image of the 2 μm Cu pillars with 20 μm pillar length.

The above analysis has demonstrated the synergistic effect of both the 3-D current collector geometry and ALD surface modification to achieve high CE Li metal anodes, and decouple the mechanistic effects of each. The ALD coated 2 μm Cu pillar arrays not only exhibited a much higher CE of 99.3% compared to planar Cu (95.7%), but it also tripled the cycle life when galvanostatically cycled at 1 mA/cm^2. This enhanced electrochemical performance can reduce the amount of required excess Li metal loading in Li metal batteries, thus increasing the overall specific energy and energy density. To demonstrate this, an uncoated, planar Cu electrode with a

Li reservoir of 4 mAh/cm^2 (instead of 2 mAh/cm^2) was cycled, as shown in **Figure 4.16c**. In order to obtain a similar cycle life to the ALD coated 3-D current collector, the required amount of excess Li needs would need to increase by a factor of more than two.

4.2 Conclusions

This work demonstrates the fabrication of vertically-aligned and highly-uniform Cu pillar arrays on a Cu foil via templated electrodeposition for use as a 3-D current collector. With this highly-ordered model platform, we demonstrated that the rational design of 3-D current collector, combined with ALD surface modification, can be used to achieve improved Li plating and stripping morphology and CE. The results in this paper have led to several key points of understanding:

(1) The geometry of the 3-D current collector has a significant impact on the Li morphology upon Li plating/stripping, which affects the CE and cycle life. This emphasizes the critical need to rationally control the geometric parameters of 3-D current collectors in order to achieve the desired Li morphology. Cu pillar arrays of 2 μm pillar diameter and an average pore spacing of 5 μm exhibited compact and uniform Li deposition and displayed improved performance compared to both larger and smaller diameters and spacing. This can be attributed to a number of factors, including local current density, electric field focusing, ionic diffusion, and separator interactions. These variables in turn affect the nucleation density, average growth size and shape of deposits, and dead Li formation.

(2) The vertical pillar architecture can cause local deformation of separators when compressed against the Cu pillars, which appears to block Li-ion flux on the tops of the pillars and causes Li deposition to preferentially occur within the pores rather than on top of the pillar arrays. This minimizes the risk of hazardous short circuiting of the battery, as Li growth occurs in the void space between the pillars, rather than outward towards the counter electrode. However, if the diameter and spacing of the rods becomes too small (as in the 0.2 μm sample), this effect is insufficient to overcome the driving force for preferential growth at the top surfaces

(3) ALD ZnO surface modification can be further applied to the Cu pillar arrays to tune the interfacial chemistry, which is a powerful technique to deposit highly conformal thin films on high-aspect-ratio Cu pillars with precise thickness control. An ultrathin layer (50 nm) of ALD ZnO

appears to facilitate more homogeneous Li nucleation, resulting in larger and more densely-packed Li morphologies, as well as more reversible Li plating/stripping. With the synergistic effect of the 3-D geometry and surface modification, the ALD coated 2 μm pillar arrays exhibited a high CE up to 99.4% under a current density of 1 mA/cm^2 and 99.5% under a current density of 0.5 mA/cm^2.

(4) This study has shed light on several important parameters for designing and manufacturing optimized 3-D current collectors. The model system of highly-ordered and uniform pillars allows us to decouple input variables that have been previously coupled in the vast majority of studies of 3-D current collectors for Li metal anodes. The insights gained from this work can therefore be further applied to rational design of alternate 3-D architectures.

4.3 Materials and Methods

4.3.1 Fabrication of vertically aligned Cu pillar arrays

Cu pillar arrays were fabricated by templated electrodeposition on battery-grade Cu foils (18 μm thick, Oak Mitsui Inc.). The electrolyte bath was consisted of 0.6 M copper sulfate ($CuSO_4$, Sigma-Aldrich) and 30 mM sulfuric acid (H_2SO_4, Sigma-Aldrich) to increase the solution conductivity (pH 1.8). A customized setup was designed where a PCTE membrane (47 mm diameter, Sterlitech Corp. and EMD Millipore) was sandwiched between two Cu foils. A piece of cellulose filter (Whatman) was immersed into the electroplating solution and then placed between the PCTE membrane and the counter Cu electrode to avoid short circuiting during electrodeposition. The setup was kept under a stack pressure by using clamps and was then connected to a potentiostat to perform Cu electrodeposition.

Electrodeposition of Cu was achieved using pulsed current technique to relax the concentration gradient within the small pores during the plating process. A repeated sequence of three steps was used: (1) A current pulse of 25 mA/cm^2 is applied to the cell for 50 ms; (2) A current pulse of 2 mA/cm^2 is applied to the cell for the next 250 ms; (3) The cell is rested for 600 ms. The pulse sequence was repeated until the targeted pillar length was reached.

After the electrodeposition, samples were immersed into dichloromethane (Sigma-Aldrich) for 2 hr at 35 ^oC to dissolve the PCTE membrane, followed by O_2 plasma cleaning to remove organic residue and acid etching to remove surface oxides. The samples were subsequently rinsed

with deionized water and isopropyl alcohol, before being transferred into an argon-filled glovebox to prevent oxidation.

4.3.2 Atomic layer deposition of ZnO

Ultrathin ZnO films were deposited by ALD in a glovebox-integrated Savannah S200 (Veeco/Cambridge Nanotech Inc.). Diethylzinc and deionized water were used as the precursors with a pulse time of 1.0 s and 0.02 s, respectively. A carrier gas flow rate of 10 SCCM ultra-high purity argon was used during purging. The purge time after each pulse was 30 s. The chamber temperature was kept at 150 ^{o}C throughout the deposition process.

4.3.3 Coin cell assembly and testing

All air sensitive materials were handled in an argon-filled glovebox (MBraun) with oxygen and water levels < 5 ppm. Li-Cu cells were assembled using CR-2032 coin cell cases, spacers, and wave springs (MTI Corp.). Celgard 2325 was used as the separator. 75 μL of electrolyte (Soulbrain) was used for each cell. The electrolyte was 1M LiTFSI in DOL:DME (1:1 volume ratio) with 1 wt.% $LiNO_3$. Li metal foil (750 μm thick, Alfa Aesar) was used as the counter electrode against the Cu working electrode, where both of them were punched into 1.6 cm^2 discs prior to cell assembly. The electrochemical performance of the coin cells was evaluated using a Landt 2001a battery testing station.

4.3.4 Electrochemical measurements

Cyclic voltammetry experiments were scanned between a voltage range of 0-2 V (vs. Li/Li^+) at a scan rate of 0.5 mV/s using a Biologic VSP system. Three-electrode measurements were performed using a hermetically sealed glassware setup in the glovebox. The reference electrode was a scraped piece of Li metal foil. The data was collected using the bipotentiostat capabilities of the Biologic VSP system, which can measure the potential of the counter electrode and working electrode vs. reference electrode simultaneously. The cell assembled without presence of the polymer separator was also used the same setup.

4.3.5 Materials characterization

Cycled electrodes were collected from coin cells for SEM analysis. Cells were first uncrimped using a disassembly die in the same MTI crimping press and electrodes were removed and rinsed with fresh DMC for several times to remove electrolyte residue. SEM images were obtained using Tescan MIRA3 FEG SEM and FEI Helios 650 Nanolab SEM. TEM imaging was performed using JEOL 3011 HREM.

A Kratos Axis Ultra was used for XPS analysis. A monochromated Al source was used with 160 eV pass energy. An argon-ion source with 4 kV accelerating voltage and 200 μA extractor current was used for sputtering off surface films.

Chapter 5

Efficient Fast Charging Enabled by 3-D Graphite Anode Architectures

Adapted from K.-H. Chen, M. J. Namkoong, V. Goel, C. Yang, S. Kazemiabnavi, S. M. Mortuza, E. Kazyak, J. Mazumder, K. Thornton, J. Sakamoto, N. P. Dasgupta, *Journal of Power Sources* **2020**, 471, 228475 from Elsevier.[10]

As discussed in section 2.3, enabling fast-charging, high areal loading, and dense electrodes are all critical to improve state-of-the-art Li-ion batteries with high energy densities. In order to improve the transport limitations through thick electrodes, one strategy is to modify the diffusion pathways for ionic transport by engineering 3-D electrode architectures. Several previous studies have incorporated macro-pores or extra voids within electrodes to promote ion transport.[84,85,138–140] For example, Sakamoto et al. designed highly-ordered macroporous electrode structures by incorporating sol-gel and self-assembled templating to prevent electrolyte concentration polarizations.[138] Chiang and coworkers fabricated electrodes with pore channels by co-extrusion and magnetic alignment.[84,139,140] Introducing vertical macro-pores has also been explored at the coin-cell level to improve accessible charge/discharge capacity at slow rates and low-temperature operations.[83,141] Furthermore, Smith and coworkers have modeled and predicted that structured electrodes containing electrolyte-filled macro-pores can enhance ion transport and accessible capacity compared to unstructured electrodes at the same porosity.[85] While improved electrochemical performances have been reported in these studies, in order to achieve the U.S. DOE goals for EVs, demonstrating large-format Li-ion batteries capable of charging in 10-15 minutes while maintaining a high energy density and Coulombic efficiency over extended cycling is critical.

In this work, we apply a laser patterning process to precisely introduce pore channels into post-calendered graphite anodes. This process results in a highly ordered laser-patterned electrode (HOLE) architecture consisting of arrays of vertical channels through the electrode thickness (**Figure 5.1**). These pore channels serve as linear diffusion paths for rapid ionic transport into the bulk electrode and can also facilitate improved through-plane transport. As a result of this improved transport, the Li-ion concentration throughout the electrode volume is more homogeneous and cell polarization is reduced, leading to a higher accessible capacity and lower propensity for Li plating on thick graphite electrodes during fast charging.

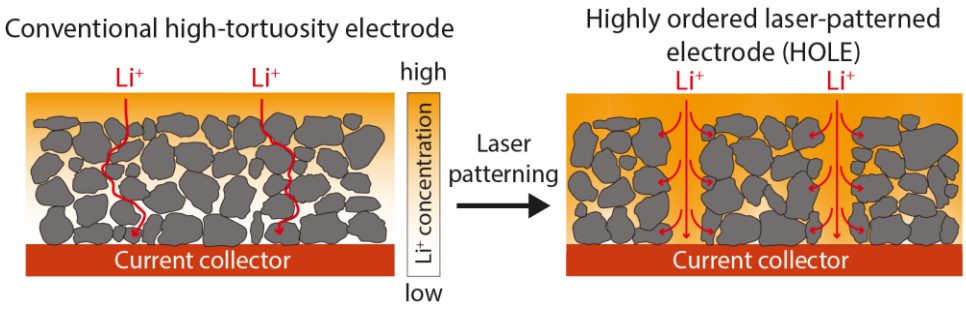

Figure 5.1. Schematic illustration of the conventional high-tortuosity graphite anode and HOLE design. Li-ion concentration gradients are reduced in the HOLE architecture due to the improved ionic transport in the vertical pore channels.

The proposed approach has three advantages over alternative methods. First, the laser patterning process is directly compatible with today's Li-ion battery manufacturing[142], by modifying graphite anodes after calendering. Therefore, the laser-patterning step can be directly integrated into existing roll-to-roll manufacturing lines. Second, this process has no impact on the cell volumetric energy density, as both the bulk porosity and thickness of graphite electrodes remain unchanged before/after patterning, and the cell capacity remains limited by the cathode since the N/P ratio is greater than 1. Third, the laser process can be used to precisely tune the geometric parameters of the HOLE architecture, such as hole diameter and spacing. This could be used to enable power performance and energy density optimization.

This work applies the HOLE design to industrially relevant cells (> 2 Ah multi-layer graphite-NMC pouch cells) and electrodes (natural graphite anodes with > 3 mAh/cm^2 capacity loading and 1.44 g/cm^3 electrode density). As a result of the HOLE architecture, we demonstrate > 97% and > 93% capacity retention over 100 cycles of 4C and 6C fast-charge cycling respectively,

compared to 69% and 59% for unpatterned electrodes under the same conditions. After 600 cycles, the capacity retention of the HOLE cell was 91% at 4C and 86% at 6C. Furthermore, the HOLE design allows for cells to access > 90% of the total cell capacity during fast charging. Systematic analysis of the electrochemical performance (capacity fade, Coulombic efficiency, voltage profile) and electrode morphology, along with electrochemical dynamic simulations, were performed to provide mechanistic insights into the efficacy of the HOLE architecture. The presented performances meet both the DOE and USABC goals for fast-charging batteries.

5.1 Results and Discussion

5.1.1 Preparation of HOLE graphite anodes

In order to realize Li-ion batteries with high energy density, anodes with high areal capacity and electrode density were used in this work. Natural graphite anodes were prepared using a pilot-scale roll-to-roll processing facility at the University of Michigan Battery Lab. A total areal mass loading of 9.48 mg/cm^2 (3.2 mAh/cm^2 capacity loading) was used as the baseline loading to study Li plating under fast-charge conditions. The calendered porosity was controlled to be 32% (1.44 g/cm^3 electrode density). It is noted that we intentionally avoided using low-loading and/or uncalendered anodes, which are less relevant to state-of-the-art batteries with high energy densities.[87]

HOLE architectures with aligned pore channels were fabricated by performing laser patterning on calendered anodes. A high-precision laser patterning platform was constructed to perform HOLE modifications on anodes for pouch cells. This is achieved by combining a pulsed laser source and a galvo-scanning optics system. To evaluate the fast-charge performance of the unpatterned graphite anodes (control) and HOLE anodes, multi-layer pouch cells were assembled. Control and HOLE graphite anodes were assembled with NMC-532 cathodes with N/P ratios fixed between 1.1-1.2. The pouch cells have a capacity of 2.2 Ah and were cycled between a 3-4.15 V voltage window.

5.1.2 Morphology analysis of HOLE graphite anodes

To examine the morphology of graphite anodes before/after laser patterning, SEM was performed. **Figure 5.2e-g** show the control (unpatterned) graphite anode. The natural graphite particles have an ellipsoidal shape with an average particle size of 8 μm. The cross-sectional image further shows the densely packed graphite particles throughout the thick anode.

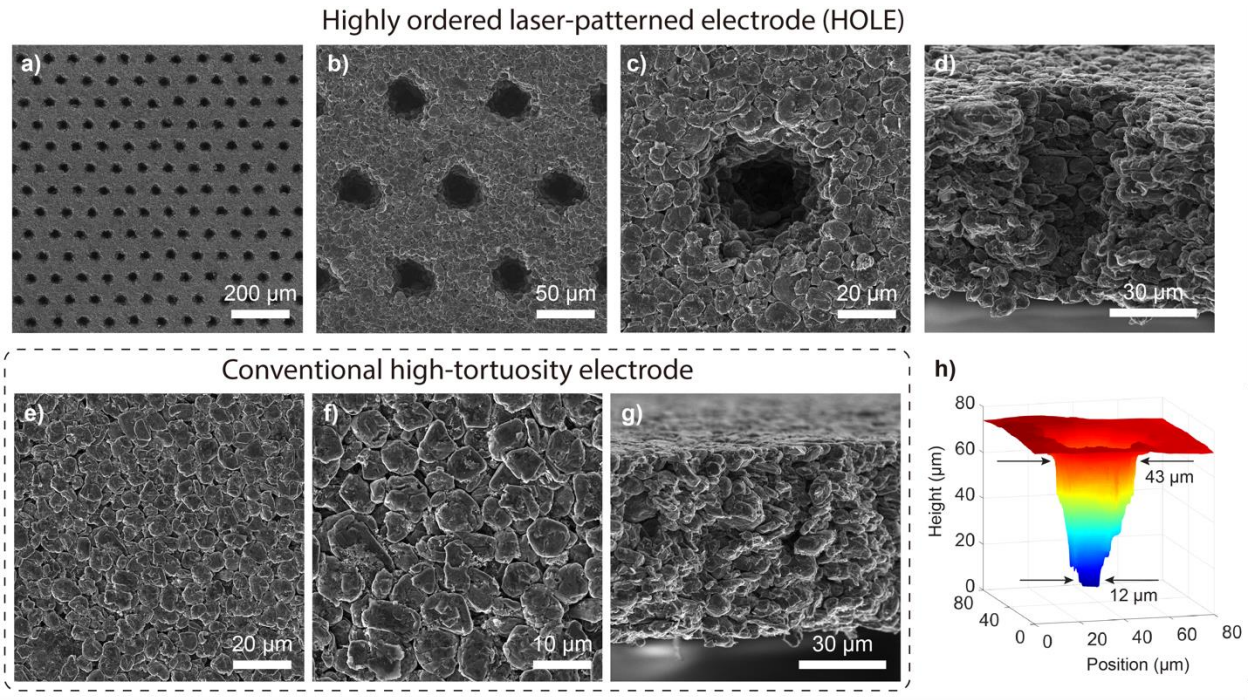

Figure 5.2. Top-down and cross-sectional SEM images of the (a-d) HOLE anode and (e-g) conventional high-tortuosity anode. (h) 3-D surface reconstructions from high-resolution optical microscope images showing the shape of tapered pore channels.

Figure 5.2a-d show the HOLE anode after laser-patterning from the same control anode. As shown in **Figure 5.2a-b**, uniform and close-packed hexagonal arrays of pore channels were formed. The electrode surface remained clean with no debris or residual particles after patterning. Higher magnification imaging (**Figure 5.2c-d**) demonstrates that laser ablation results in the sublimation of entire graphite particles rather than cutting through particles.[143,144] In addition, **Figure 5.2d** also shows that the pore channels are slightly tapered toward the bottom of the electrode, which results from the laser-graphite interactions. The average diameter of the channels was measured to be 42.7 ± 2.2 μm at the top and 12.4 ± 1.7 μm at the bottom of the electrodes. To

further verify this frustum shape of the pore channels, 3-D surface reconstructions were performed using a focal series of high-resolution optical microscopy images (**Figure 5.2h**).

Previous modeling of 3-D channels in graphite electrodes identified that for a fixed average porosity, a smaller spacing-to-thickness ratio leads to higher capacity.[85] In the HOLE architecture, a 43 μm/12 μm top/bottom diameter was chosen based on the resolution of the laser and optics system and the thickness of the electrode. Based on this resolution, an inter-hole center-to-center pitch of 85 μm was used so as to restrict the amount of removed material to 10.2% ± 0.12%, which was confirmed by weighing the electrodes on a high-precision digital scale before/after the laser patterning. We note that the selected HOLE geometry does not reduce the capacity or volumetric energy density of the battery, since the N/P ratio remains greater than 1.

5.1.3 Fast charging at 4C charge rate

To evaluate the fast-charge capability at 4C and 6C charge rates, a CC-CV charge protocol with a charge time cutoff was used, following DOE battery-testing guidelines.[145] **Figure 5.3** shows an example of the 6C fast-charge protocol. Pouch cells were first charged at a constant current (CC) 6 C-rate until reaching the upper voltage cutoff (4.15 V), then charged at constant voltage (CV) until a total charge time (CC+CV) of 10 minutes is reached. For the 4C charging protocol, the applied current was 4C and the total charge-time cutoff was 15 minutes. The discharge process in this study also followed a CC-CV protocol, where cells were first discharged CC at 0.5C rate, followed by CV hold at 3.0 V until the current reached a value < 0.1C to fully discharge the cells.

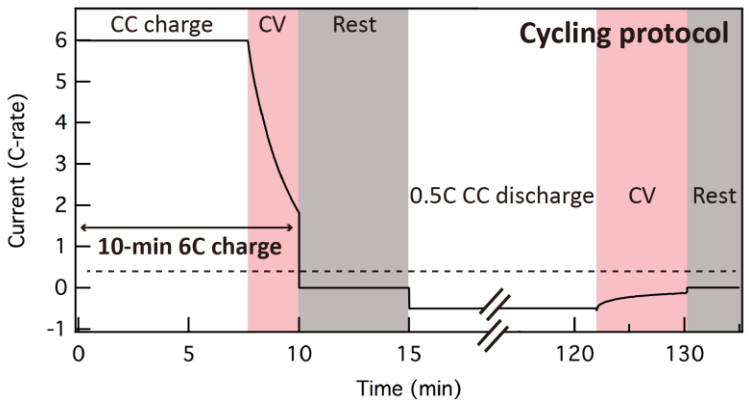

Figure 5.3. Cycling protocol for evaluating fast-charge performance at 6C charge rate.

Figure 5.4a shows the discharge capacity of the control and HOLE cells that were charged at 4C. The cells were first charged/discharged at a 0.5C rate for 3 cycles to measure the total cell capacity (2.2 Ah), followed by 100 cycles of 4C charge/0.5C discharge. In addition, 3 cycles of 0.5C charge/discharge were repeated after every 50 fast-charge cycles to quantify the capacity fade of the cells. The y-axis shows the cell capacity (normalized to the initial cell capacity) to facilitate a direct comparison.

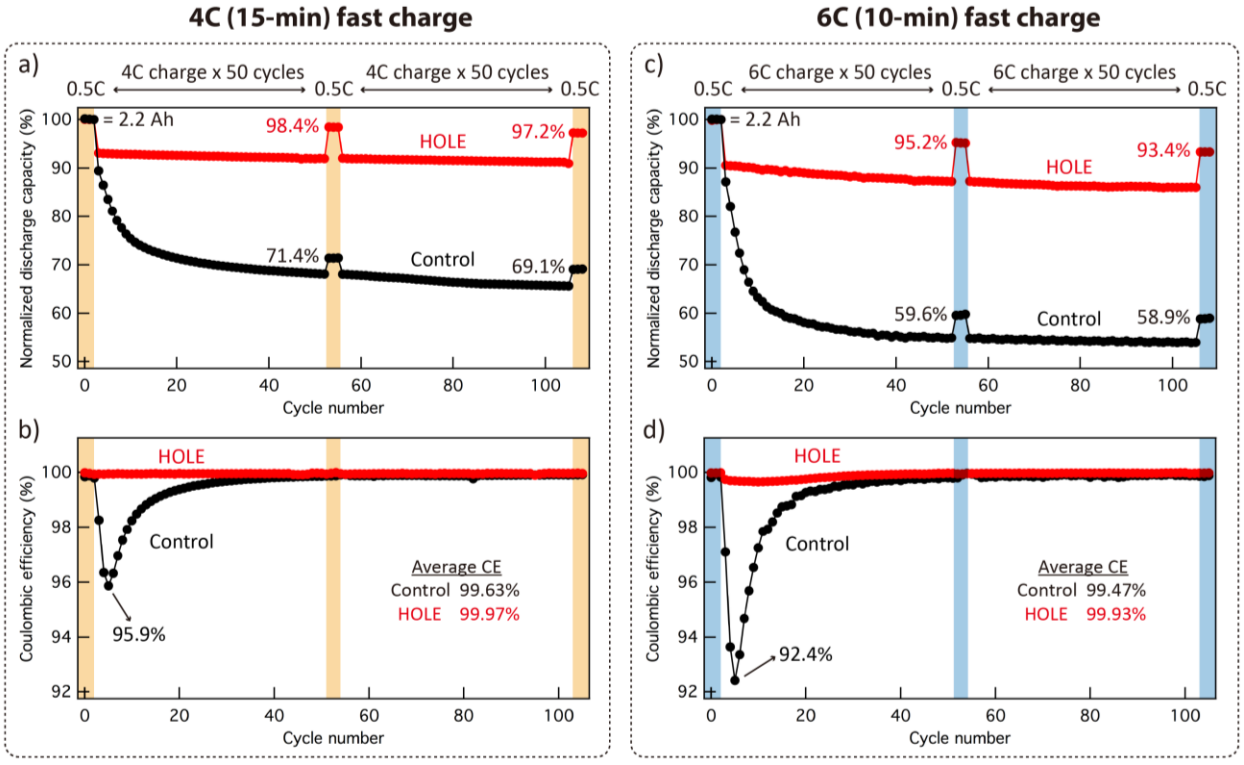

Figure 5.4. (a) Normalized discharge capacity and (b) Coulombic efficiency vs. cycle number under 4C fast-charge conditions. (c) Normalized discharge capacity and (d) Coulombic efficiency vs. cycle number under 6C fast-charge conditions.

As shown in **Figure 5.4a**, both the control and HOLE cells exhibit stable cycling at a 0.5C charge rate. However, upon fast charging at 4C, the control cell exhibits a significant capacity fade within the first 40 cycles, which can be attributed to irreversible Li plating (post-mortem analysis presented below). From cycle 40 to 100, the capacity reaches a plateau. By comparing the charge/discharge capacities at 0.5C, it is shown that the capacity retention is 69.1% after 100 fast-

charge cycles (capacity fade of 30.9%). This dramatic capacity fade during fast charging of thick electrodes is consistent with results reported by Argonne National Laboratory.[96]

Figure 5.4b shows the CE plotted vs. cycle number, providing further evidence that Li plating occurs during 4C charging of the control anode. The efficiency quickly drops to 95.9% within the first 3 cycles of 4C charging, and then slowly recovers back to > 99.5% after cycle 40. This initial decrease in CE can be attributed to Li plating during fast charging, which causes severe Li inventory loss over time. Similar capacity fade behaviors during fast charging have been reported by several previous studies.[79,90–92,96]

In contrast to the control, the HOLE cell shows a significantly improved capacity retention and CE during 4C charging. As shown in **Figure 5.4a**, stable 4C charging was achieved, allowing for 92% of the total cell capacity to be charged within 15 minutes (from 0% to 92% state-of-charge (SOC)). This large accessible capacity is maintained throughout the cycling, demonstrating that the HOLE anode design can effectively improve the fast-charge performance. The capacity retention of the HOLE cell is 97.2% after 100 cycles of 4C charging (capacity fade of 2.8%). In addition, **Figure 5.4b** shows a stark difference in efficiency when compared to the control cell, as the HOLE cell maintains an average CE of 99.97% throughout the course of the fast-charge test. Overall, we observe > 97% capacity retention after 100 cycles at a 4C charge rate with the HOLE design, compared to 69% capacity retention of unpatterned control electrodes that were fabricated from the same batch of calendared electrodes with identical process conditions.

5.1.4 Fast charging at 6C charge rate

To further show the effectiveness of the HOLE design, another batch of control and HOLE cells were cycled at a 6C charge rate (with a 10-min charge time cutoff). **Figure 5.4c** shows the cell capacity plot, where the control cell displays a more dramatic drop in capacity from 6C charging than was observed for 4C charging (**Figure 5.4a,c**). The capacity retention was 58.9% after 100 cycles of 6C charging (41.1% capacity fade). The CE plot also shows a similar dip during the initial fast-charge cycles, followed by a gradual recovery to > 99.5% after 40 cycles (**Figure 5.4d**).

Compared to the control, the HOLE cell shows a significantly improved rate performance (**Figure 5.4c-d**). Although mild capacity fade was observed during the initial fast-charge cycles, the HOLE cell was still able to access 90% of the total cell capacity within the 6C 10-min charge

(from 0% to 90% SOC). In addition, the HOLE cell shows a capacity retention of 93.4% after 100 fast-charge cycles (capacity fade of 6.6%). The average CE is 99.93% throughout the course of the test. Overall, we demonstrate the HOLE design can achieve > 93% capacity retention over 100 fast-charge cycles at 6C, compared to 59% capacity retention for unpatterned electrodes.

It is worth noting that since 10.2% of the anode material is removed during the laser patterning process, the HOLE graphite anodes have a slightly lower total electrode loading (8.51 mg/cm^2, 2.9 mAh/cm^2) than the control graphite anode (9.48 mg/cm^2, 3.2 mAh/cm^2). In addition, after accounting for the vacant pore channels, the HOLE anodes have a total porosity of 38.6% in comparison to the control (32.4% porosity). Therefore, to demonstrate the benefits of the 3-D electrode architecture, it is important to verify that the improved performance of the HOLE cells could not be achieved by unpatterned electrode with lower electrode loading and higher porosity. To demonstrate this, unpatterned graphite anodes with a similar electrode loading (8.12 mg/cm^2, 2.8 mAh/cm^2) and porosity (39.0%) to the HOLE anodes (and thus a comparable N/P ratio of the cells with the HOLE anodes) were fabricated and assembled into a pouch cell using the same NMC-532 cathodes. This pouch cell with low-loading/high-porosity unpatterned graphite anodes is labeled as "new control" in **Figure 5.5**.

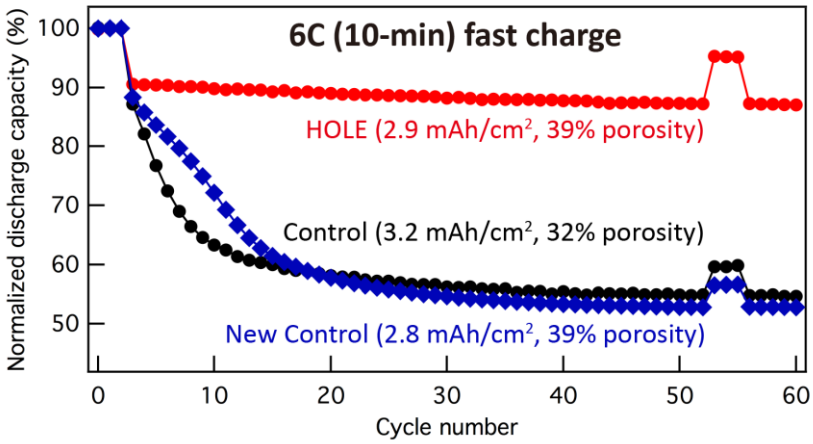

Figure 5.5. Comparison of the normalized discharge capacity vs. cycle number of the control, HOLE, and new control cells showing the capacity fade during 6C charging.

Figure 5.5 shows the capacity fade of all three of these cell configurations (control, HOLE, new control) under 6C fast-charge conditions. As shown, a similar trend in capacity fade is observed between the control and new control cells despite the lower electrode loading and higher

porosity. This result thus confirms that the improved fast-charge capability is enabled by the three-dimensional HOLE architecture and cannot be achieved by simply increasing the porosity of conventional high-tortuosity graphite anodes with similar loadings.

5.1.5 Voltage profile analysis

To provide mechanistic insight into the improved rate performance of the HOLE cells, the voltage profiles of cells charged at different C-rates are plotted in **Figure 5.6**. **Figure 5.6a** shows the first-cycle charge voltage trace at 0.5C, 1C, 4C, and 6C rates after formation cycles. When charging at 0.5C and 1C rates, both the control and HOLE cells exhibit a similar overall voltage shape, suggesting the ionic transport is not a limiting factor at these low charge rates.

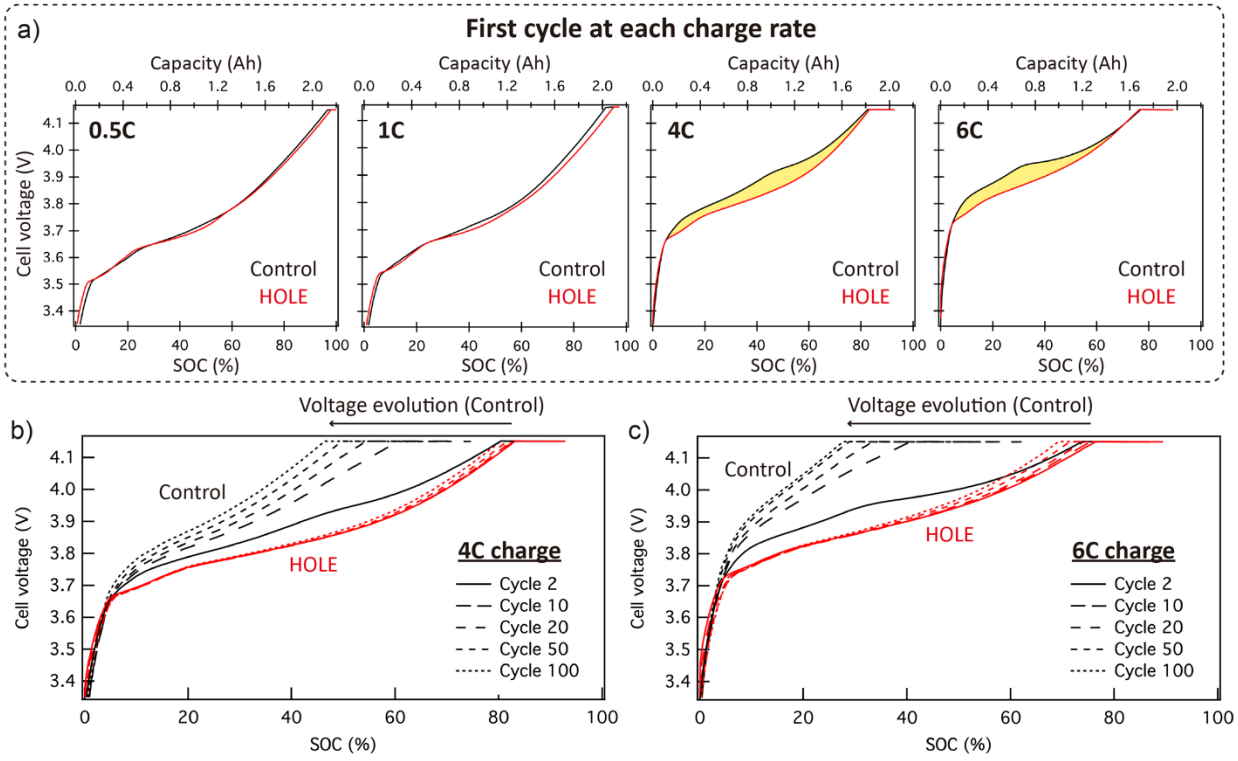

Figure 5.6. (a) Cell voltage profiles during the first charge cycle at 0.5C, 1C, 4C, and 6C rates after formation cycles. The cycle-to-cycle evolution of voltage traces occurring during (b) 4C and (c) 6C charging. The voltage profiles of the control and HOLE cells are depicted with black and red color, respectively.

During the first cycle of 4C and 6C charging, the control cell starts to exhibit increasing cell polarization compared to the HOLE cell (**Figure 5.6a**). At a 4C charge rate, the largest voltage difference is 70 mV at 45% SOC (control: 3.92 V and HOLE: 3.85 V). At the 6C charge rate, the overpotential differences become more prominent, where an 80-mV difference in voltage is observed at 30% SOC (control: 3.94 V and HOLE: 3.86 V).

Figure 5.6b-c show the voltage trace evolution of both cells from cycle 2 to 100 under 4C and 6C charging conditions. As shown in **Figure 5.6b** (4C charging), the voltage profile of the control cell changes dramatically throughout the cycling. The SOC at the end of the CC charge step (at 4.15 V) rapidly drops from 80% to 50% within the first 50 cycles. When cycling at a 6C charge rate (**Figure 5.6c**), the SOC at the end of the CC charge step for the control cell drops even more dramatically from 74% to 29%. On the contrary, the HOLE cell voltage exhibits a much more stable profile under both 4C and 6C fast-charge conditions. Overall, the voltage analysis demonstrates that the HOLE cell has lower cell polarizations and a stable voltage profile during extended fast-charge cycling.

5.1.6 Post-mortem morphology analysis

To confirm that the capacity fade during fast charging is due to Li plating, post-mortem SEM analysis was performed on the cycled graphite anodes of both the control and HOLE cells after 100 cycles of 6C charging (**Figure 5.4c**). Pouch cells were fully discharged to 3.0 V before disassembly. **Figure 5.7a** and **Figure 5.7f** show photographs of the cycled control and HOLE anodes. As expected, a considerable amount of Li plating is observed on the control graphite anodes, where Li dendrites cover the entire anode surface. Notably, the Li deposits maintain their metallic silver luster, even though the graphite anode was fully discharged before the cell teardown. This indicates that during cycling the plated Li dendrites can become electrically disconnected from the anode surface while still in the metallic Li phase, resulting in the formation of dead Li at the anode/separator interphase[8,42,79]. The irreversible dead Li formation and SEI growth on plated Li cause permanent Li inventory losses of the cell, resulting in the observed capacity fade.

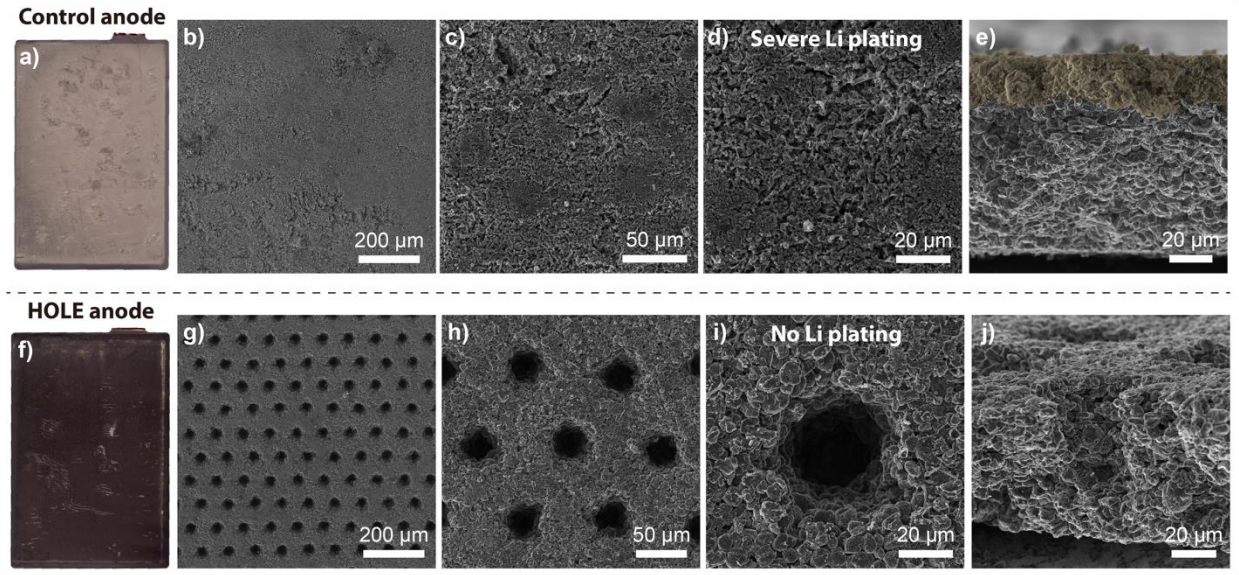

Figure 5.7. Photographs of (a) control and (f) HOLE graphite electrodes from pouch cell teardown after 100 cycles of 6C charging. SEM images further show the (b-e) severe Li plating on control anodes and (g-j) absence of Li plating on HOLE anodes.

SEM analysis (**Figure 5.7b-d**) further shows the extent of Li plating on the control graphite anode, where the entire surface is covered with dead Li and no underlying graphite particles can be observed from the top-down perspective. Cross-sectional SEM imaging (**Figure 5.7e**) shows a compact interphase of dead Li on top of the graphite anode. In contrast, the HOLE graphite anode cycled at 6C maintains a clean surface with minimal traces of Li plating (**Figure 5.7f** photograph). SEM images (**Figure 5.7g-i**) show that the HOLE architecture remains intact after fast-charge cycling, and the pore channels can be clearly observed in the images. Cross-section SEM analysis (**Figure 5.7j**) further confirms the absence of Li plating on the anode surface as well as along the inner surface of the pore channels.

5.1.7 Electrochemical dynamics simulations

To provide further insight into the mechanism for the observed improvement in performance of the thick graphite anodes with the HOLE architecture, a 3-D continuum-scale model based on porous electrode theory[146] was applied to simulate the electrochemical dynamics during charging. The model describes mass and charge transport in the solid graphite particle and liquid electrolyte phases, coupled with the electrochemical reaction that occurs at the solid/liquid

interface. We parameterized the model by matching the simulated anode voltage vs. capacity profiles of the control anodes at six different C-rates (0.1C, 0.5C, 1C, 2C, 4C, and 6C) using experimental results from three-electrode measurements. The same parameter set was then applied to simulate the three-electrode cell with the HOLE graphite anode, and the results matched well with the corresponding measurements. The parameterized model was then used to simulate the electrochemical performance of pouch cells during 4C fast charging.

Figure 5.8c compares the simulated voltage (vs. a Li reference) vs. time curves for the control and HOLE anodes during 4C charging. The simulation for each cell was terminated when the anode voltage reached 0 V. As expected, the HOLE anode was able to maintain a voltage above 0 V for a longer period of charging time than the control anode (364 s vs. 125 s). In other words, the polarization at the HOLE anode is lower than that in the control anode. This decrease in the polarization is facilitated by improved access of Li ions to graphite particles in the bulk of the HOLE anode through the channel design.

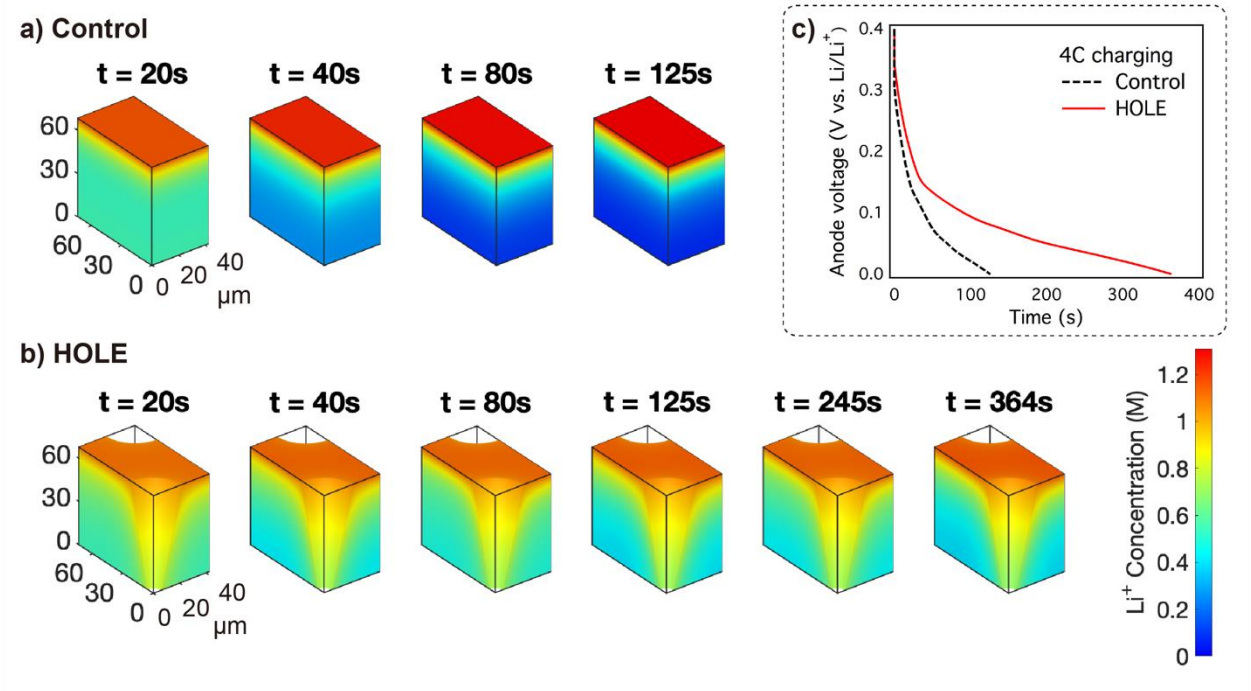

Figure 5.8. Evolution of Li-ion concentration in the electrolyte phase of the (a) control graphite anode at t = 20, 40, 80, and 125 s, (b) HOLE graphite anode at time t = 20, 40, 80, 125, 245, and 364 s during 4C charging. The color indicates the Li-ion concentration according to the color bar on the right. (c) Simulated voltage response of the anode in the control cell (dashed, black line), and in the HOLE cell (solid, red line).

Figure 5.8a and **Figure 5.8b** further compare the Li-ion concentration evolution in the electrolyte phase of the control and HOLE anodes. As shown in the figures, Li-ion concentration far from the separator/anode interface in the HOLE anode (**Figure 5.8b**) is higher than that in the control anode (**Figure 5.8a**) at all times. As a consequence of the improved Li-ion transport, a reduction in the local Li-ion concentration near the separator/anode interface can be seen in the HOLE anode compared to the control anode. The more homogenous concentration of Li ions in the HOLE anode enables a more uniform distribution of the local electrochemical reaction rate in the bulk of the HOLE anode as compared to the control anode. A more homogeneous reaction rate throughout the electrode bulk in the HOLE anode results in reduced local current density, and consequently lowers the driving force for Li plating at the separator/anode interface as compared to the control anode during fast charging.

5.1.8 Long-term fast-charge cycling

HOLE cells were further cycled at 4C and 6C charge rates over > 500 cycles to evaluate the long-term performance. **Figure 5.9a** shows the capacity retention during fast charging, where the capacity is normalized to the first-cycle fast-charge capacity in order to quantify the percentage of capacity retention during fast-charge cycling. The U.S. DOE target is also noted in the figure as a reference. For the HOLE cell fast-charged at 4C (15-min charge time), the capacity retention was 92% and 91% after 500 and 600 cycles, respectively. For 6C (10-min) fast charging, the HOLE cell demonstrated a capacity retention of 87% and 86% after 500 and 600 cycles, respectively.

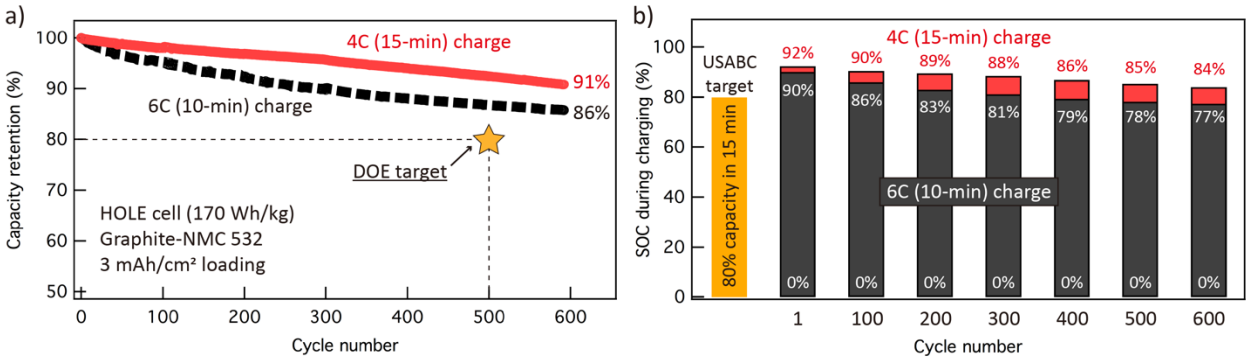

Figure 5.9. (a) Capacity retention of the 2.2 Ah HOLE cells during long-term fast-charge cycling at 4C (red solid curve) and 6C (black dashed curve). The DOE fast-charge target is labeled in the

figure as a reference. (b) Cell SOC during fast charging vs. cycle number showing the high accessible capacity of HOLE cells under 4C (red) and 6C (black) charge conditions. The USABC fast-charge target is also plotted as a reference.

In addition to the excellent capacity retention during fast charging, we also note that the HOLE design allows for cells to access > 90% of the total cell capacity during 4C (15-min) and 6C (10-min) charging due to improved ionic transport and lowered cell polarization. **Figure 5.9b** shows the SOC of the HOLE cells at the beginning/end of charging, from cycle 1 to cycle 600. Since the cells were fully discharged to 3.0 V every cycle, the SOC was 0% at the beginning of each fast-charge cycle. As shown in **Figure 5.9b**, during the initial 4C charge, the HOLE cell can be charged from 0% to 92% SOC within 15-minutes. After 600 cycles, 84% of the total capacity is still accessible at a 4C charge rate. The USABC goal for fast-charging EV batteries is to charge 80% of the cell capacity with a 15-minute charge time. Therefore, we demonstrated that the HOLE cells successfully meet the USABC fast-charge target, even after 600 fast-charge cycles.

For 6C (10-min) fast-charging, the HOLE cell can be charged to 90% SOC during the initial fast-charge cycle and 77% SOC at cycle 600 (**Figure 5.9b**). These numbers not only show the high accessible capacity during fast charging enabled by the HOLE design, but also demonstrate that the HOLE cells can be cycled under aggressive conditions (large SOC window) and still show excellent capacity retention during long-term fast-charge cycling (**Figure 5.9a**).

5.2 Conclusions

This work demonstrates efficient fast-charging of Li-ion batteries (> 4C charge rate), which is enabled by the HOLE architecture. High-loading graphite anodes (> 3 mAh/cm^2) and an industrially relevant cell format (> 2 Ah pouch cells) were used to show the feasibility of using HOLE anodes for high-energy-density Li-ion cells. The through-thickness, laser-ablated pore channels facilitate Li-ion transport into the bulk electrode, thus reducing concentration gradients during fast charging. Consequently, a higher accessible capacity and low propensity to Li plating was achieved. Detailed analysis of the electrochemical response and electrode morphology, coupled with continuum-scale modeling, were performed to provide further insight into the mechanism of improved transport. Using the HOLE architecture, we have observed > 97% and > 93% capacity retention over 100 cycles of 4C and 6C fast-charge cycling respectively, compared

to 69% and 59% for unpatterned electrodes. After 600 cycles of fast-charging, the capacity retention of the HOLE cells remained as high as 91% at 4C and 86% at 6C charge rates. Moreover, the HOLE design allows for cells to access > 90% of the total cell capacity during fast charging. The presented performances address both the DOE and USABC goals for fast-charging batteries.

The laser patterning approach demonstrated here is compatible with current Li-ion battery manufacturing, since graphite anodes are modified after calendering. Therefore, we envision that this process can be directly integrated into existing roll-to-roll manufacturing lines. By overcoming tradeoffs between energy density and power performance, the HOLE architecture can enable EV-scale batteries that can maintain long range, while simultaneously reducing charging time.

5.3 Materials and Methods

5.3.1 Electrode fabrication

Natural graphite (battery grade, SLC1506T, Superior Graphite) electrodes were prepared using a pilot-scale roll-to-roll processing facility at the University of Michigan Battery Lab. Natural graphite was first mixed with C65 conductive additive and CMC/SBR binder in a weight ratio of 94:1:5 in deionized water to make a homogeneous slurry. The resulting anode slurry was then casted onto copper foils (10 μm thick). A total areal mass loading of 9.48 mg/cm^2 (3.2 mAh/cm^2 capacity loading) was used as the baseline loading in this study. After casting, the graphite anode was dried and calendered to 32% porosity, corresponding to an electrode density of 1.44 g/cm^3. NMC-532 (battery grade, Toda America) was used as the cathode material. The cathode formulation was 92 wt.% NMC-532, 4 wt.% C65 conductive additive, and 4 wt.% PVDF binder. The cathode slurry was casted onto aluminum foils (15 μm thick) with a total areal mass loading of 16.58 mg/cm^2 and then calendered to 35% porosity.

5.3.2 Laser patterning

Laser patterning was performed on the calendered graphite anodes to prepare HOLE anodes. A high-precision laser patterning platform was designed and built by combining a pulsed laser source (Matrix 355-8-50, Coherent) and a galvo-scanning optics system (Thorlabs) through a data acquisition card (National Instruments). The pulsed laser source was operating at 8 watts

and 355 nm wavelength with a repetition rate of 50 kHz and a pulse duration of 10 ns. Close-packed hexagonal arrays of pore channels were made by synchronizing the galvo-scanning optics system with the laser source. 10 laser pulses were used at each site to create pore channels through the 9.48 mg/cm^2 baseline graphite anodes. To avoid re-deposition and contamination from the ablated graphite, cross-flowed inert gas was constantly passing along the electrode surface during the patterning process.

5.3.3 Pouch cell assembly

All fabricated electrodes were first baked in vacuum ovens at 80 ^{o}C overnight to remove any residual moisture prior to cell assembly. Pouch cells were assembled in a dry room (dew point of < -50 ^{o}C) at the University of Michigan Battery Lab. Each pouch cell was constructed of 7/8 cathode/anode double-sided electrodes with 12 μm polyethylene separators (ENTEK). Each electrode had an area of about 70 cm^2 on each side. 1M $LiPF_6$ in 3/7 v/v EC/EMC with 2 wt.% VC additive (SoulBrain MI) was used as the electrolyte. After electrolyte filling, cells were sealed in the dry room and allowed to rest for 12 hours to ensure full electrolyte infiltration into the electrodes. Subsequently, three formation cycles were performed at 0.1C current between 3.0-4.15 V voltage window. Afterwards, the cells were transferred back into the dry room to perform degassing to release any gas produced during the formation cycles and then re-sealed.

5.3.4 Electrochemical testing

Pouch cells were cycled in a temperature-controlled chamber at 30 ^{o}C using a Maccor 4000 series automated test system (Maccor Inc.). After formation cycles and degassing/re-sealing, cells were first charged/discharged at 0.5C current for 3 cycles to ensure the capacity was stable.

Three-electrode measurements were performed using a commercial electrochemical test cell (ECC-PAT-Core, EL-CELL GmbH). Graphite anode and NMC-532 cathode were used, along with a ring-shaped lithium metal reference electrode placed between the two electrodes. The separator was 220 μm FS-5P (Freudenberg Viledon FS 2226E + Lydall Solupor 5P09B). Electrochemical data was collected using a BioLogic VSP potentiostat system (Bio-Logic USA), which can measure the potential of the working electrode and counter electrode vs. reference electrode simultaneously.

5.3.5 Materials characterization

Post-mortem SEM analysis was performed to characterize Li plating during fast-charge cycling. Cycled pouch cells were first discharged to 3.0 V and transferred into an argon-filled glovebox (MBraun). Graphite electrodes were then carefully collected from the pouches and rinsed thoroughly with DMC several times to remove electrolyte residue. Subsequently, the electrodes were dried and stored in the glovebox antechamber under vacuum before transferred into SEM for imaging. SEM analysis was performed using a Tescan MIRA3 FEG SEM at the Michigan Center for Materials Characterization.

Chapter 6

Design of Graphite/Hard Carbon Hybrid Anodes for Li-ion Batteries

The large anode polarization during fast charging has been attributed to several physicochemical processes, including (1) ionic transport in the electrolyte phase, (2) reaction kinetics at the graphite/electrolyte interface, and (3) solid-state Li diffusion in graphite particles.[79,90–92] Consequently, previous research efforts have focused on enhancing ionic transport in porous electrodes by reducing electrode tortuosity[10,83,84], improving interfacial and transport kinetics through new electrolyte and/or additive design[26,147,148], increasing the cell temperature during charging[92], and applying coatings to the anode surface.[149]

Chapter 5 demonstrated that fast charging of Li-ion batteries using conventional planar graphite anodes remains challenging, particularly with high capacity loadings ($\geq$ 3 mAh/cm^2). In addition, developing scalable processing approaches that are directly compatible with existing Li-ion manufacturing with minimal additional cost and implementation time is also important to accelerate commercialization.

In contrast to graphite, which has long-range order in its crystallographic structure, hard carbon is defined as non-graphitizable carbon consisting of highly disordered carbon layers (**Figure 6.1**). During the lithiation process, Li can be inserted in between the disordered carbon sheet domains as well as in the micro-pores of the hard carbon structure.[150–152] When used as the anode material for batteries, hard carbon has the following characteristics: (1) low material density (1.6 g/cm^3) compared to graphite (2.2 g/cm^3), (2) sloping charge/discharge voltage profile between 0-1.2 V vs. Li/Li$^+$, (3) low initial Coulombic efficiency (< 80%), and (4) enhanced power performance.[13,19,151–153] While the improved rate performance is attractive for high-power applications[154], the higher redox potential, lower density, and poor initial Coulombic efficiency

have limited the adoption of hard carbon in high-energy-density battery systems.[13,155] Therefore, a tradeoff between the energy density and power performance is present (**Figure 6.1**).

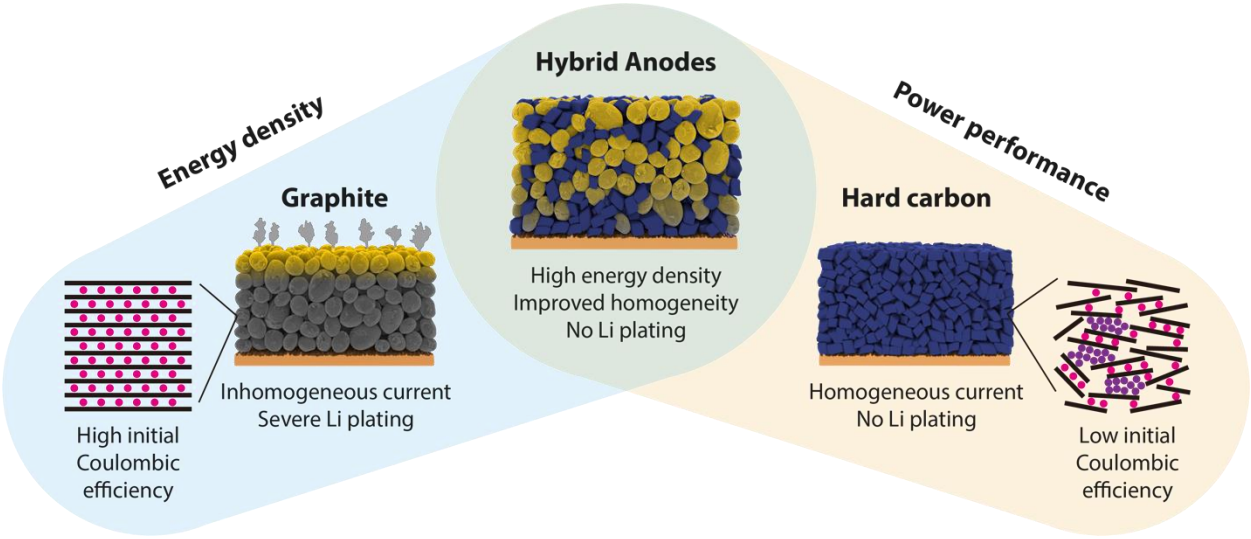

Figure 6.1. Schematic illustration of the energy/power density tradeoff between graphite and hard carbon. In this study, graphite/hard carbon hybrid anodes are shown to improve current homogeneity and reduce Li plating during fast charging, while maintaining high energy densities. Lithiated graphite and hard carbon particles are indicated by gold and blue colors, respectively.

In this work, we introduce a strategy to overcome this energy/power density tradeoff by fabricating uniform mixtures of graphite/hard carbon active material particles into a bulk hybrid anode. By doing so, it is possible to balance the desirable characteristics of both materials and rationally tune the electrode properties in a synergistic manner to improve current homogeneity and reduce Li plating during fast charging, while maintaining sufficiently-high cell energy densities (**Figure 6.1**).

Previous studies on the concept of graphite/hard carbon hybrid anodes have been largely limited to surface modifications of the active materials prior to electrode fabrication, such as coating hard carbon onto graphite particle surfaces to improve rate capability[156,157] or applying graphite micro-crystallites onto hard carbon particles to improve initial Coulombic efficiency and reversible capacity.[158] While mixing of varying carbonaceous materials have been studied for battery systems[159–161], the reported charge rates have not addressed the DOE and industry fast-charge targets (10-min charge time).

This work demonstrates hybrid anodes fabricated by mixing graphite and hard carbon to achieve fast-charging Li-ion batteries with energy density > 180 Wh/kg, using industrially relevant multi-layer pouch cells (> 1 Ah) and electrode capacity loadings (3 mAh/cm^2). Standard roll-to-roll slurry casting was performed to fabricate the hybrid anodes, demonstrating compatibility with existing Li-ion manufacturing. By tuning the blend ratio of graphite and hard carbon, it is shown that the battery performance can be systematically tuned to simultaneously achieve high energy density and fast charging. As a result of the optimized hybrid anode design, we demonstrate pouch cells with 87% and 82% specific energy retention after 500 cycles of 4C and 6C fast-charge cycling using hybrid anodes, compared to 61% and 48% for cells using graphite anodes under the same conditions. In addition, while the optimized hybrid cells show 10% lower initial specific energy compared to the graphite cells, the remaining specific energy after 500 cycles of fast charging is 27% larger at 4C and 53% larger at 6C.

Systematic electrochemical analysis was performed to demonstrate the efficacy of the hybrid anode design, and synchrotron tomography was employed to analyze the electrode microstructures. Continuum-scale electrochemical simulations were further performed to provide insights into the enhanced fast-charge performance, which is attributed to the improved homogeneity in reaction current distribution throughout the hybrid anode. The cell performance presented in this work addresses the DOE goal for fast-charging high-energy-density Li-ion batteries.

6.1 Results and Discussion

6.1.1 Fabrication of hybrid anodes

Graphite/hard carbon hybrid anodes were prepared using a pilot-scale roll-to-roll processing facility at the University of Michigan Battery Lab. Five graphite/hard carbon blend ratios were investigated in this study, namely, graphite/hard carbon = 100/0, 75/25, 50/50, 25/75, and 0/100 (weight ratios). The resulting hybrid anodes are described below as graphite, Gr-75, Gr-50, Gr-25, and hard carbon, respectively. A capacity loading of 3 mAh/cm^2 was controlled for all 5 types of anodes with a calendered porosity of 31-33%.

SEM was performed to examine the morphology of the prepared hybrid anodes. **Figure 6.2a** shows a top-down image of the graphite anode. The graphite particles have an ellipsoidal

shape with an average particle size of 7.8 µm. **Figure 6.2e** shows an image of the hard carbon anode. Compared to the graphite, hard carbon particles have a more isotropic shape. The hard carbon also displays a smaller average particle size of 3.3 µm. For Gr-75 (**Figure 6.2b**), Gr-50 (**Figure 6.2c**), and Gr-25 (**Figure 6.2d**) hybrid anodes, the SEM images show that both graphite and hard carbon particles were homogeneously distributed within the electrodes.

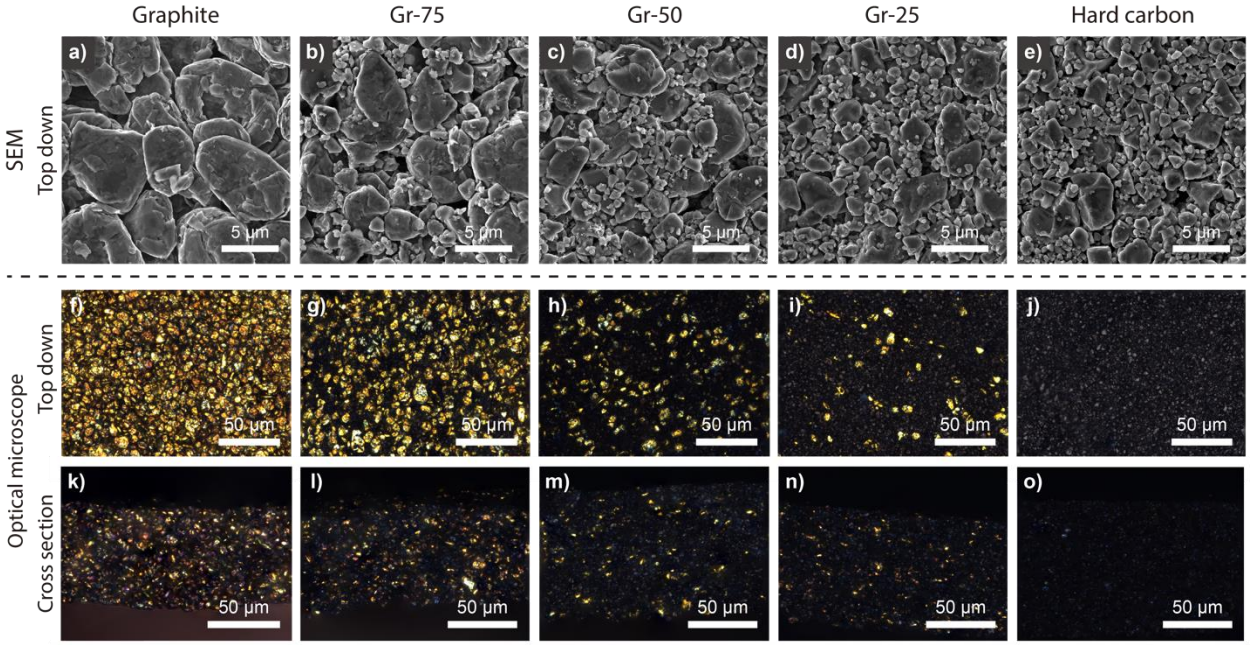

Figure 6.2. Top-down SEM images of the (a) graphite, (b) Gr-75, (c) Gr-50, (d) Gr-25, and (e) hard carbon anodes. Top-down and cross-sectional optical microscope images of the lithiated (f,k) graphite, (g,l) Gr-75, (h,m) Gr-50, (i,n) Gr-25, and (j,o) hard carbon electrodes, respectively.

To further confirm the homogeneous mixing of graphite and hard carbon, optical microscopy was performed. The anodes were lithiated at a C/50 rate, and then disassembled and imaged. At 100% state-of-charge, the color of graphite changes from grey to gold[162,163], whereas the color of hard carbon remains dark grey. Therefore, by inspecting the distribution of the gold graphite particles in the hybrid anodes, the homogeneous blend of graphite/hard carbon can be visualized (**Figure 6.2f-o**).

6.1.2 Synchrotron tomography

Synchrotron tomography was performed on the graphite, Gr-50, and hard carbon electrodes to analyze 3-D microstructures, following methods described in the previous studies.[164,165] **Figure 6.3a-c** show 3-D representations of the three electrodes obtained by segmenting the tomography data. The tomography data show variations in the porosity from 30% to 35%. In addition to the grey-scale value information provided by the tomographic imaging, the segmentation threshold was adjusted to yield a porosity of 31-33% to match the measured capacity loading and thickness values (**Figure 6.3d-f**).

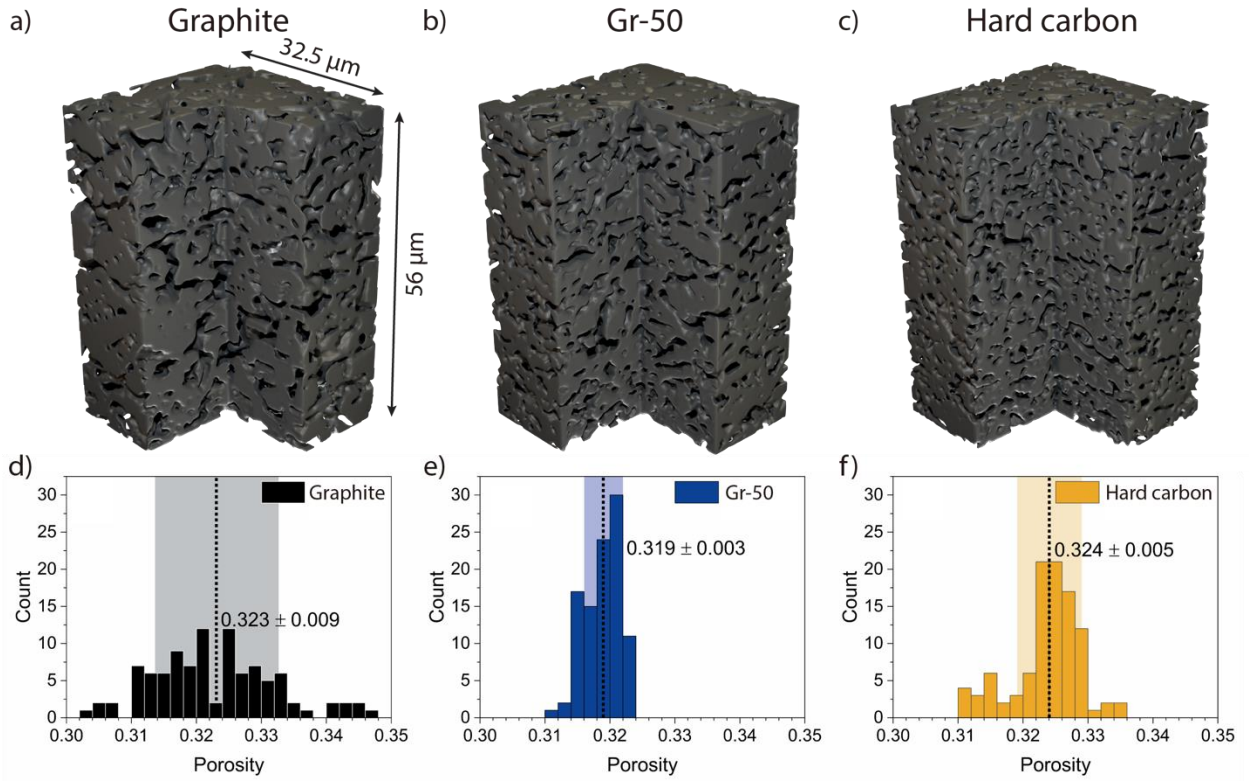

Figure 6.3. 3-D representations of the segmented tomography data with 32.5 µm × 32.5 µm × 56 µm edge length of the (a) graphite, (b) Gr-50, and (c) hard carbon electrodes. The solid particle phase is represented in grey. Porosity histograms of 100 cubic representative sub-volumes with an edge length of 56 µm of the (d) graphite, (e) Gr-50, and (f) hard carbon electrodes. The average porosity of all electrode segmentations is ~32%.

While the average porosity values are ~32% for all three electrodes after the adjustment, differences in the variation of local porosity can be identified. As shown in **Figure 6.3e**, the Gr-50 electrode has the most uniform porosity distribution shown by its narrow histogram, followed

by that of hard carbon (**Figure 6.3f**).[166] In contrast, the porosity histogram of the graphite electrode is significantly wider, ranging from 30%-35% (**Figure 6.3d**). These localized variations in electrode microstructures may impact the local current density within the electrodes.[38]

In addition, microstructural features such as particle and pore size can be identified, as shown in **Figure 6.3a-c**. The graphite electrode shows the largest pores with elongated shapes, whereas the hard carbon electrode has the smallest pores with a more circular shape. The average pore diameter reduces from 1.02 ± 0.03 μm for the graphite electrode to 0.72 ± 0.01 μm for the hard carbon electrode. The average pore diameter of the Gr-50 electrode (0.82 ± 0.01 μm) is closer to the value of the hard carbon electrode. It is noted that due to the limitation in resolution, pores smaller than 700 nm (3-4 voxels wide) cannot be reliably quantified.

Overall, the tomography analysis demonstrates that, while the graphite and hard carbon are uniformly blended throughout the bulk of the electrode, subtle differences in the local microstructures can be observed.

6.1.3 Voltage and initial Coulombic efficiency analysis

To characterize the voltage profile of the hybrid anodes, three-electrode measurements were performed using a Li metal reference electrode. **Figure 6.4a** shows anode potential vs. state-of-charge (SOC) profiles of all 5 anodes during charging at a C/10 rate. As shown, the graphite anode shows an initial drop in potential to 0.2V, followed by well-defined voltage plateaus. In contrast, the hard carbon anode displays a sloping voltage trace as the potential gradually decreases from 1.2 V to 0 V. For Gr-75, Gr-50, and Gr-25 hybrid anodes, the anode potentials are observed at intermediate values between the graphite and hard carbon voltage profiles.

Figure 6.4b shows a magnified view of the voltage profiles between 0-0.3 V vs. Li/Li^+. It can be clearly observed the graphite anode displays three characteristic plateaus at 0.2 V, 0.12 V, and 0.08 V, which can be attributed to transitions between staged phases during Li intercalation.[16,167] On the other hand, hard carbon does not exhibit any voltage plateau. The high-potential region of the sloping voltage profile has been associated with Li insertion into interlayer space between carbon layers, and the low-potential region has been attributed to Li storage in the micro-pores of hard carbon.[150]

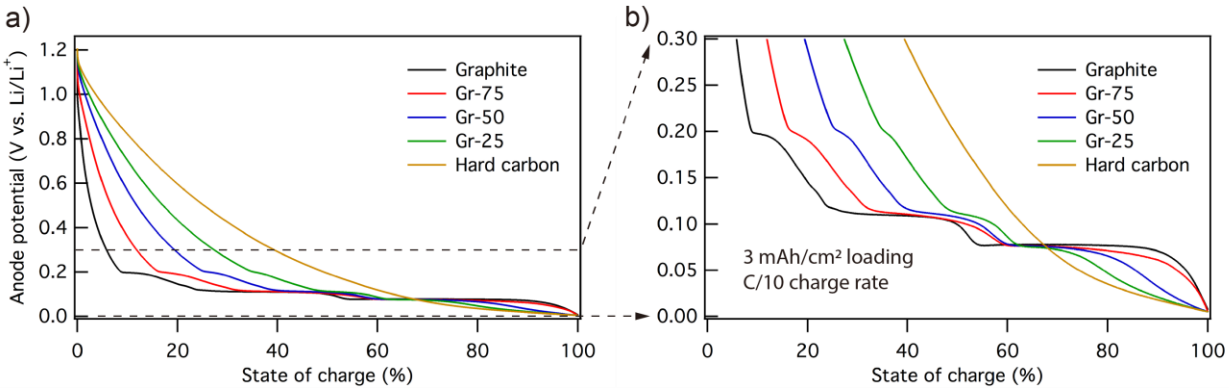

Figure 6.4. (a-b) Three-electrode measurements showing the anode potential (V vs. Li/Li^+) as a function of state-of-charge for graphite, Gr-75, Gr-50, Gr-25, and hard carbon.

For Gr-75, Gr-50, and Gr-25 hybrid anodes, the voltage traces display features from both graphite (voltage plateaus) and hard carbon (sloping potential), indicating that both materials are electrochemically active in the hybrid anodes during charging. With higher graphite content in the hybrid anodes, increasing width in voltage plateaus is observed, which is consistent with a larger fraction of the capacity provided by graphite. It is also noted that while the voltage plateaus associated with graphite occur at approximately the same average potential values regardless of the varying graphite/hard carbon blend ratios (**Figure 6.4b**), the slope of the plateaus increases with increasing hard carbon content. Furthermore, the onset of the plateaus is observed to be shifted to higher SOCs with increasing hard carbon content. This is consistent with the more positive potential of hard carbon at low SOC, which will cause hard carbon to preferentially lithiate during the early stages of charging the hybrid anodes. These effects, and their impact on fast charging, will be discussed further in the modeling section below.

To quantify the initial irreversible capacity of the hybrid anodes, initial Coulombic efficiency (ICE) during the first charge/discharge cycle was measured using a 3-electrode cell. **Figure 6.5a** shows the ICE vs. graphite content. The graphite anode displayed a high ICE of 88%, whereas the hard carbon anode ICE was only 76%. The significantly lower first-cycle efficiency of hard carbon has been attributed to the SEI formation, trapped Li in the micro-pore structure, and reactions between Li and surface functional groups.[13,153] This large irreversible capacity of hard carbon translates into an energy density penalty, which has restricted the use of hard carbon in state-of-the-art Li-ion batteries, compared to graphite. For Gr-75, Gr-50, and Gr-25 hybrid anodes, the corresponding ICE follows a linear relationship as a function of the graphite content

(**Figure 6.5a**), indicating that the ICE can be tuned by adjusting the blend ratios of graphite and hard carbon.

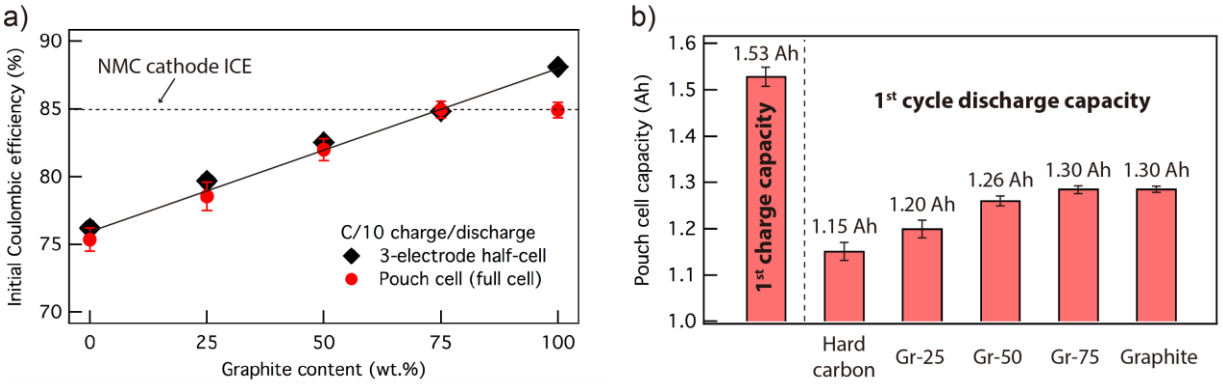

Figure 6.5. (a) Initial Coulombic efficiency vs. graphite content plot of the hybrid anodes in 3-electrode cell (black) and pouch cell (red) configurations. The ICE of NMC-532 cathode is also labeled in the plot. The charge/discharge rate was fixed at C/10. (b) Cell capacity plot showing the first-cycle charge and discharge capacity of the pouch cells.

The ICE was further measured in full cells, where multi-layer pouch cells (> 1 Ah) were fabricated. The hybrid anodes were assembled with NMC-532 cathodes (N/P ratio of 1.16 ± 0.1) to make 5 different types of pouch cells, namely, graphite, Gr-75, Gr-50, Gr-25, and hard carbon cells. Pouch cells were cycled at a C/10 rate to measure the charge/discharge capacity during the first cycle (**Figure 6.5b**). As shown, while the first-cycle charge capacity of all 5 pouch cells is ~1.53 Ah, differences in the subsequent discharge capacity are observed. The ICE of the pouch cells is calculated and plotted in **Figure 6.5a** to compare with 3-electrode cell results. As shown in the figure, the pouch cell ICEs agree well with the 3-electrode measurements, with the exception of the pure graphite cell.

The discrepancy between the 3-electrode and pouch cells using graphite anodes can be explained by the ICE of the cathode. Winter et al. have shown that the first-cycle irreversible capacity of NMC cathodes can be attributed to kinetic limitations and irreversible processes, resulting in an ICE of 83-86%.[28] Recently, Whittingham et al. also demonstrated the first-cycle capacity loss of NMC-811 is due to slow kinetics and surface changes in the materials during the charge process.[168] Therefore, it can be inferred that for anodes exhibiting higher ICE than NMC cathodes, the overall full cell capacity and ICE will be limited by the cathode. To verify this point, the ICE of the NMC-532 cathode was further measured (to be 85%) using the 3-electrode cell

setup and plotted in **Figure 6.5a** (dashed line). For this reason, the Gr-75 hybrid anode has the same full-cell ICE value as the pure graphite anode (**Figure 6.5a**), which demonstrates that hybrid anodes with relatively low hard carbon content will not suffer significantly from an ICE penalty.

To demonstrate stable cycling of the hybrid anode under standard conditions, all 5 types of pouch cells were charged/discharged at a 1C/1C rate between 2.7-4.2 V (**Figure 6.6**). All pouch cells exhibit similar aging rates with high capacity retention of 95-96% after 200 cycles. This result indicates that there is minimal difference in performance between the cells using different hybrid anodes during standard-rate cycling after the initial cell formation cycles.

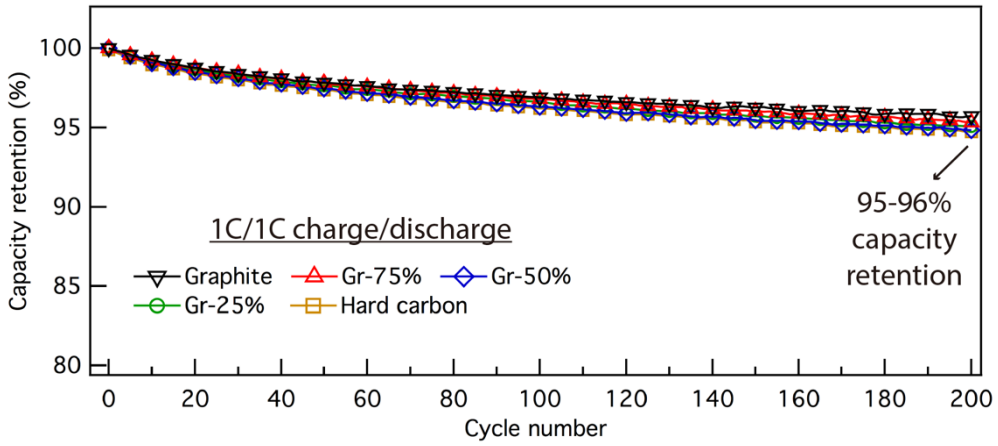

Figure 6.6. Normalized capacity vs. cycle number plot showing the capacity retention of all 5 types of pouch cells during 1C/1C charge/discharge cycling test.

6.1.4 Fast-charge cycling performance

To evaluate the fast-charge capability of the hybrid anodes, the same CC-CV charging protocol with a charging time cutoff was used (15 min for 4C and 10 min for 6C), as described in Chapter 5.[10,145] Pouch cells were cycled in a temperature-controlled chamber at 30 ºC.

Figure 6.7a shows the normalized cell capacity vs. cycle number plot during 4C (15-min) fast-charge cycling. The capacity shown here is the 1C discharge capacity after each 4C charge, in order to reflect Li inventory loss and the remaining cyclable capacity. The y-axis is normalized to the first 4C charge cycle to facilitate a comparison of capacity retention among all 5 types of pouch cells. The graphite cell exhibits significant capacity fade during the first 50 fast-charge cycles due to significant Li plating.[10,79,91,92,169] As cycling progresses, the capacity retention of the graphite

cell levels off at 67% after 100 cycles, as the significant Li inventory loss reduces the driving force for further Li plating.[10,90] The Gr-75 cell displays a similar trend with less capacity fade during fast-charge cycling, suggesting an improved rate performance in comparison to the graphite (**Figure 6.7a**). The capacity retention of the Gr-75 cell is 85% after 100 cycles of 4C fast charging.

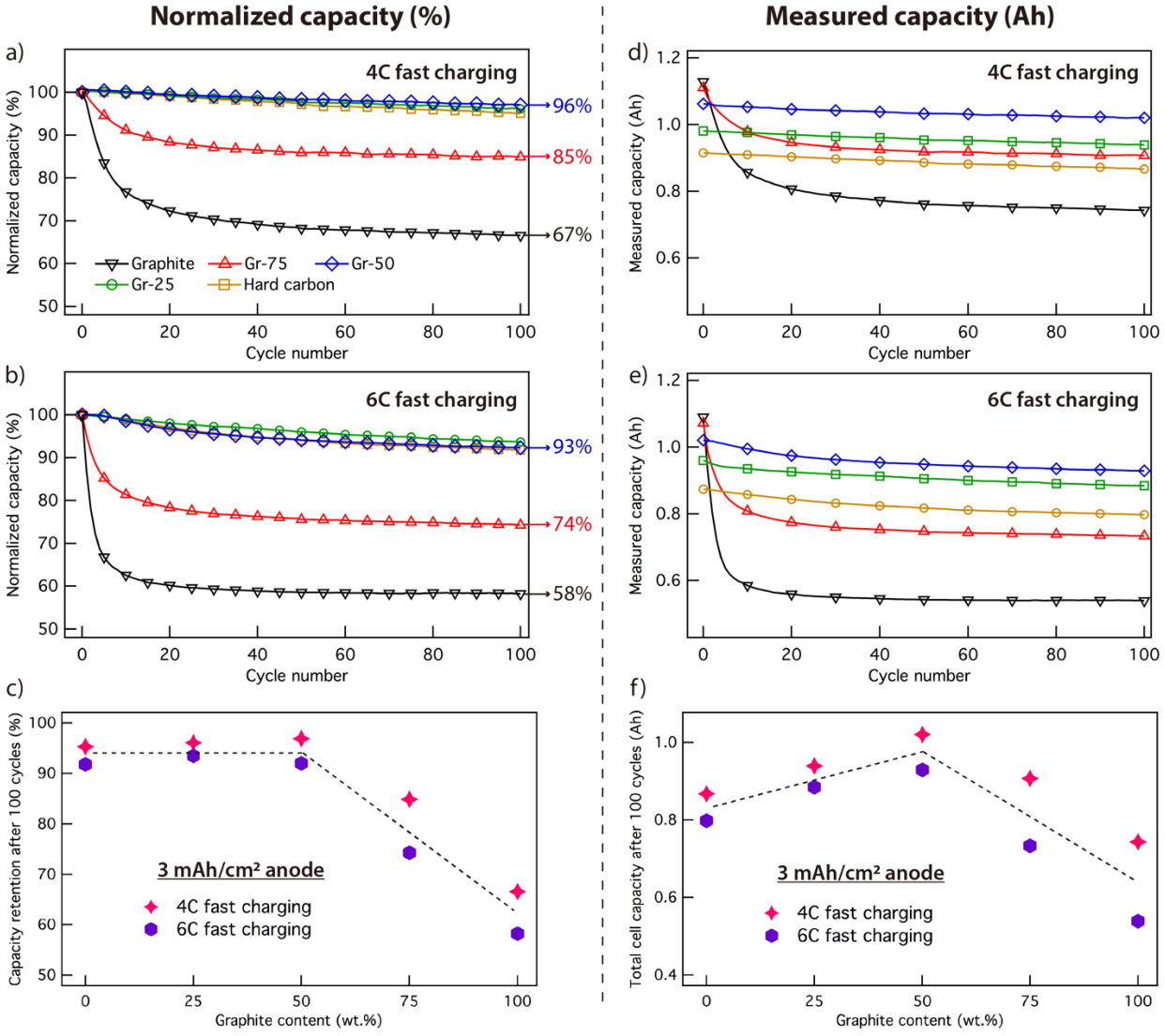

Figure 6.7. Normalized capacity vs. cycle number plots during (a) 4C and (b) 6C fast-charge cycling. (c) Summary of the capacity retention (%) after 100 cycles of 4C and 6C fast charging. Measured capacity vs. cycle number plots during (d) 4C and (e) 6C fast-charge cycling. (f) Summary of total cell capacity (Ah) after 100 cycles of 4C and 6C fast charging. The capacity shown here is the 1C discharge capacity after each charge half cycle.

In contrast, Gr-50, Gr-25, and hard carbon cells all exhibit stable 4C charging throughout the course of the test. The steep initial capacity drop observed in the graphite and Gr-75 cells is completely absent in these cells. As a result, the capacity retention of the Gr-50, Gr-25, and hard carbon cells after 100 cycles is approximately 96% (**Figure 6.7a**).

To further demonstrate the efficacy of the hybrid anode design, another batch of pouch cells were cycled at a 6C charge rate. As shown in **Figure 6.7b**, larger drops in capacity are observed for both the pure graphite and Gr-75 cells that 4C fast-charge cycling, with only 58% and 74% capacity retention after 100 cycles. The reduced capacity retention during 6C fast-charge cycling also corresponds to lower minimum Coulombic efficiency values when compared with 4C fast-charge cycling (**Figure 6.8**). This has been attributed to an increased amount of Li plating with increasing charge rates.[10] In contrast, the Gr-50, Gr-25, and hard carbon cells again exhibit stable cycling during 6C fast charging. The capacity retention is ~93% after 100 cycles (**Figure 6.7b**).

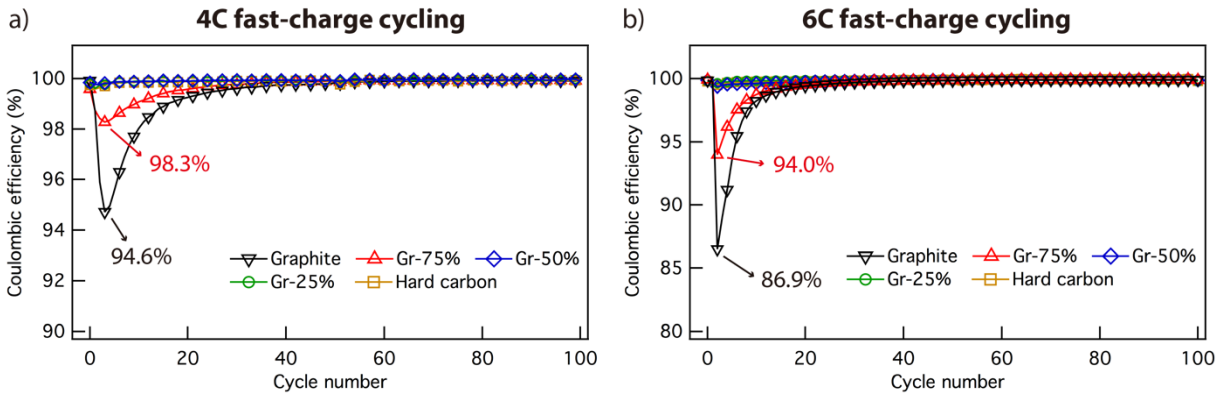

Figure 6.8. Coulombic efficiency vs. cycle number plots under (a) 4C and (b) 6C fast-charge conditions for the graphite, Gr-75, Gr-50, Gr-25, and hard carbon pouch cells.

Figure 6.7c summarizes the capacity retention of all 5 types of pouch cells after 100 cycles of 4C and 6C fast charging. As shown in the figure, for hybrid anodes with increasing (> 50 wt.%) graphite content, lower capacity retention is observed. For hybrid anodes with < 50 wt.% graphite content, the cells exhibit stable performance with minimal capacity fade during 4C and 6C fast charging (**Figure 6.7c**).

While the normalized cell capacity plots (**Figure 6.7a-c**) facilitate direct comparisons of capacity fade (%), the first-cycle irreversibility needs to be accounted for, in order to demonstrate

the total cell capacity. Therefore, **Figure 6.7d** and **Figure 6.7e** further plot the measured discharge capacity (Ah) vs. cycle number during 4C and 6C cycling. While the graphite and Gr-75 cells display higher cell capacity after the formation cycles, they suffer from significant capacity fade upon fast charging. On the contrary, the Gr-50, Gr-25, and hard carbon cells exhibit stable cycling at both C-rates. Overall, the Gr-50 cells show the highest total cell capacity among all 5 types of cells after 100 cycles of 4C and 6C charging. Additionally, voltage trace plots at various stages of cycling are provided in **Figure 6.9**, which demonstrate that a stable voltage profile is observed for graphite content ≤ 50%.

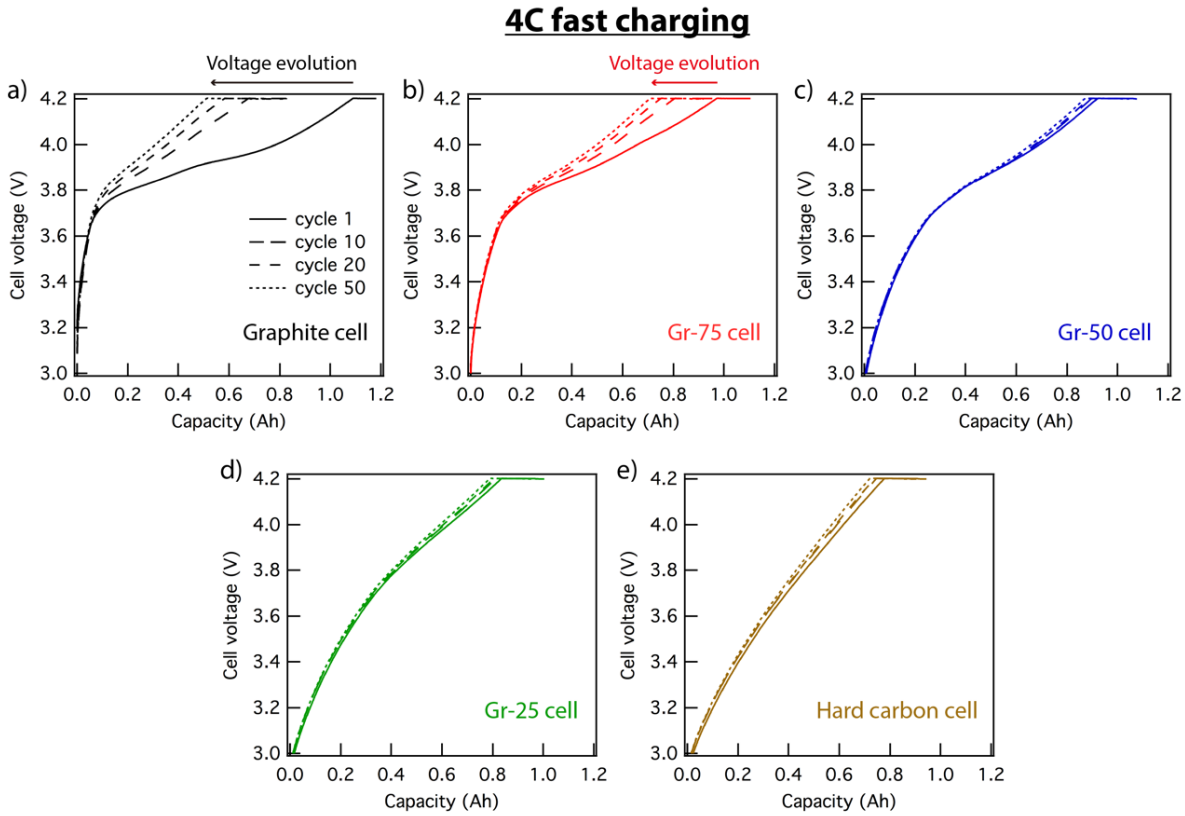

Figure 6.9. Cycle-to-cycle evolution of voltage traces occurring during 4C (15-min) fast-charge cycling of the graphite, Gr-75, Gr-50, Gr-25, and hard carbon pouch cells.

Figure 6.7f summarizes the total cell capacity of the pouch cells after 100 fast-charge cycles. Considering both ICE during cell formation and capacity fade during fast charging, it is demonstrated here that an optimal graphite/hard carbon blend ratio can be selected to maximize the accessible cell capacity during fast-charge cycling. For an anode loading of 3 mAh/cm^2 under

4C and 6C fast-charge conditions, our analysis indicates that the 50/50 graphite/hard carbon blend ratio provides the maximum performance within the set of ratios tested.

6.1.5 Post-mortem morphology analysis

To confirm that the capacity fade during fast-charge cycling is correlated with increased Li plating, post-mortem SEM analysis was performed on the pouch cells after 100 cycles of 4C charging. Cells were fully discharged before disassembly. Photographs of the cycled anodes are shown in **Figure 6.10a-e**. A considerable amount of Li plating is observed on both the graphite and Gr-75 anodes (**Figure 6.10a-b**). SEM images further show the extent of Li plating on the graphite and Gr-75 anodes, where the electrode surface is covered with dead Li, and no underlying active material particles can be observed from a top view (**Figure 6.10f-g**). Cross-sectional SEM images also show the Li plating (false-colored in yellow) on the anode surface (**Figure 6.10k-l**). An increase in the dead Li thickness is observed with increasing graphite content, which is consistent with the increased capacity fade during fast-charge cycling (**Figure 6.7a**).

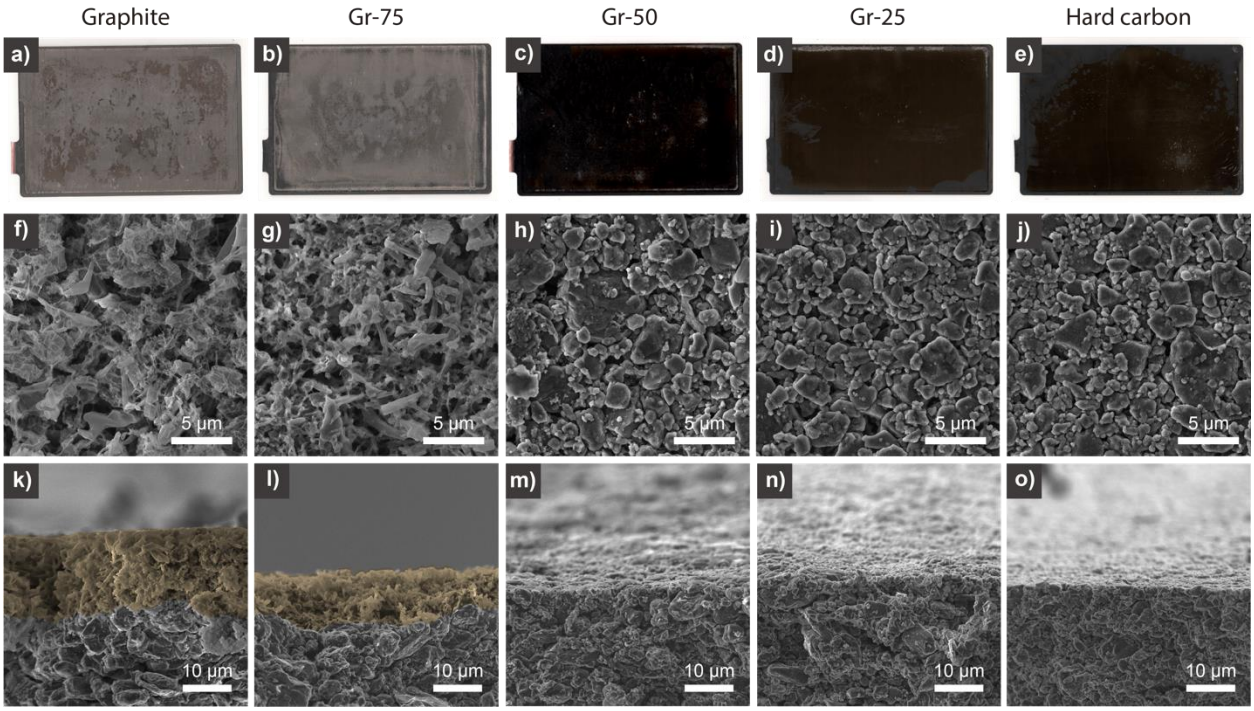

Figure 6.10. (a-e) Photographs of the cycled anodes from pouch cell teardown after 100 cycles of 4C fast charging. SEM analysis further show the (f-j) top-down and (k-o) cross-sectional images. Li plating on the graphite and Gr-75 anodes is false-colored in yellow in Figure k and l.

In contrast, the cycled Gr-50, Gr-25, and hard carbon anodes maintain a pristine surface, with no evidence of Li plating (**Figure 6.10c-e**). Both top-down (**Figure 6.10h-j**) and cross-sectional (**Figure 6.10m-o**) SEM images show the electrode surface and active particles remain clean and intact after extended fast-charge cycling. The post-mortem morphology is thus in a good agreement with the electrochemical performance (**Figure 6.7**).

6.1.6 Continuum-scale electrochemical simulations

To provide mechanistic insights for the observed improvement in rate performance of the hybrid anodes, continuum-scale simulations based on porous electrode theory[170,171] were conducted. In particular, we focused on the spatial variation in local reaction current density throughout the anode thickness, and the consequences of this heterogeneity on the propensity for Li plating. The model was parameterized by matching the simulated voltage vs. capacity curves with the corresponding three-electrode measurements for the three anodes at six different C rates.

Galvanostatic charging of the graphite, Gr-50, and hard carbon anodes at 4C and 6C charging were simulated, and the results for 4C are summarized in **Figure 6.11**. The simulations were terminated when the anode voltage (vs. Li metal reference) reached 0 V, below which Li plating is likely to occur. Thus, these simulations correspond to the initial portion of the CC charging step in the experiments. A comparison of the simulated voltage vs. time curves for the three anodes is shown in **Figure 6.11f**. The hard carbon anode maintains a voltage above 0 V for the longest time, followed by the Gr-50 and graphite anodes.

To explain the difference in the performance of the three anodes, we examined the evolution of the local reaction current density (**Figure 6.11a-e**), as defined by reaction current per unit volume within each anode. The reaction current density is obtained by multiplying the reaction flux at the surface of the active material particles, the surface area of the particles per unit volume of the electrode, and Faraday's constant.

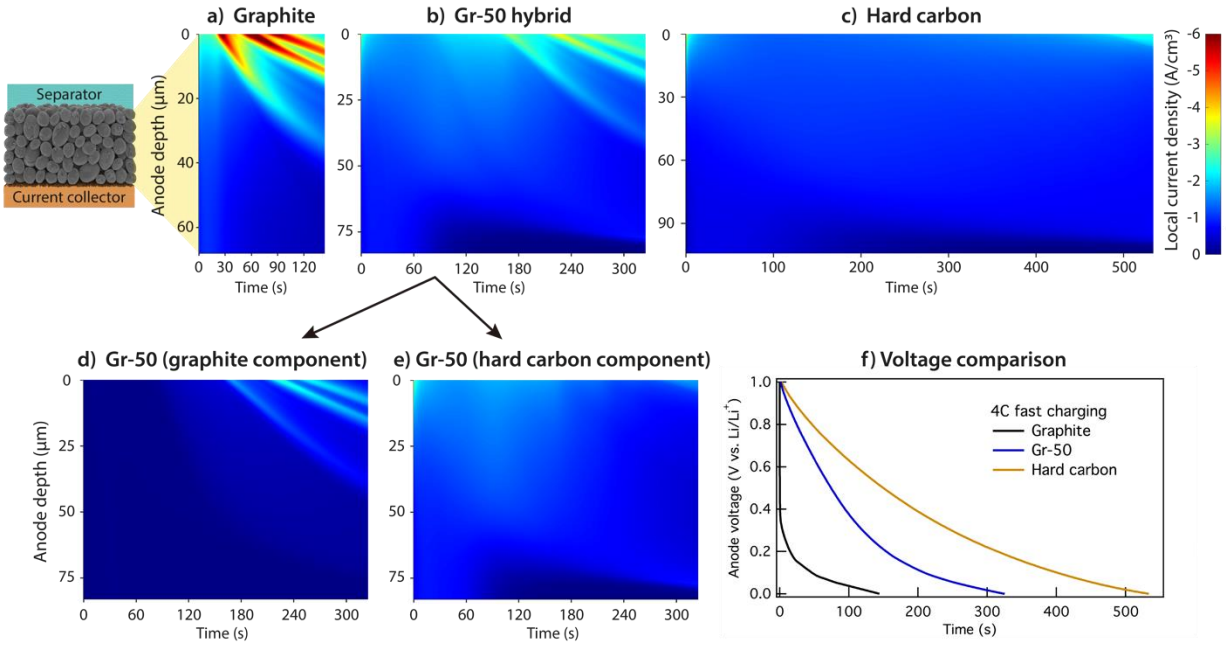

Figure 6.11. Evolution of the local reaction current density as a function of the position through the thickness of the (a) graphite, (b) Gr-50, and (c) hard carbon anodes during 4C charging. (d-e) Evolution of the local current density contribution by the graphite and hard carbon components in the Gr-50 anode. The maximum magnitude of the reaction current density on the color bar is limited to 6 A/cm^3 to enable a better visual comparison among the three anodes. (f) Comparison of the simulated voltage vs. time plots during 4C charging for the three anodes.

For the graphite anode (**Figure 6.11a**), it can be observed that the current density distribution becomes highly inhomogeneous after ~20 seconds of charging, with most of the reaction taking place in the region near the anode/separator interface. The peaks observed in the reaction current density arise because of the plateaus observed in the graphite open-circuit voltage (OCV) profile.[172] As mentioned earlier, a highly inhomogeneous current distribution results in a large anode overpotential, thereby resulting in an earlier termination of the simulation. Moreover, the high reaction current magnitude causes graphite particles near the anode/separator interface to lithiate much faster than the rest of the anode. When the surface of the graphite particles near the anode/separator interface becomes saturated with Li, it becomes susceptible to Li plating as the charging is continued.[173–175] Therefore, due to the inhomogeneous current density distribution, the graphite anode has a higher propensity for Li plating during fast charging.

In contrast, the distribution of the reaction current density is much more uniform in the hard carbon anode during 4C charging (**Figure 6.11c**). This results in a smaller overpotential in the anode, which allows it to maintain current at a potential higher than 0 V for a longer time.

Moreover, the homogeneous distribution lowers the local reaction current and thus reduces saturation of the particle surface near the anode/separator interface. This is consistent with the improved rate performance and absence of Li plating observed experimentally. The more homogeneous current density distribution in the hard carbon anode arises from the complex interplay between thermodynamics, reaction kinetics, and electrochemistry.[176] In particular, the sloping OCV profile can homogenize the current density distribution[172,177], while any transport limitations tend to increase the inhomogeneity. Due to its higher solid-state Li diffusivity, smaller particle size, sloping OCV profile, and lower electrode tortuosity, the hard carbon anode exhibits a more uniform current density distribution than the graphite anode.

By blending graphite and hard carbon, the resulting Gr-50 hybrid anode exhibits a significant improvement in the homogeneity of the current density distribution (**Figure 6.11b**), as compared to the graphite anode. To demonstrate that the hard carbon component within Gr-50 enables this improvement, we examined the evolution of the local current density for the graphite and hard carbon constituents of Gr-50 anode, as shown in **Figure 6.11d** and **Figure 6.11e**. Individually, the current density distribution follows the qualitative trend of the non-blend anodes. For the graphite component, most of the reaction takes place in the region near the anode/separator interface, while for the hard carbon component, the reaction is distributed more uniformly. Nonetheless, there exists a complex interplay between the two constituents, which is evident in the evolution of the integrated current for each individual component (**Figure 6.12**). The graphite component does not significantly contribute to the reaction until ~80 seconds, as the bulk of the component is electrochemically inactive in the voltage range during that time period, except for the region near the anode/separator interface. On the other hand, the hard carbon component contributes a large fraction of the current throughout the charging. Even towards the end of the simulation (when the anode voltage reaches 0 V), the hard carbon supplies 54% of the total current, which in turn reduces the load on the graphite component. In fact, the maximum surface current density of the graphite particles in the Gr-50 anode is 1.3 mA/cm^2, as compared to 1.6 mA/cm^2 for the pure graphite anode. Furthermore, these values occur at strikingly different times, 224 seconds for the Gr-50 anode vs. 61 seconds for the graphite anode.

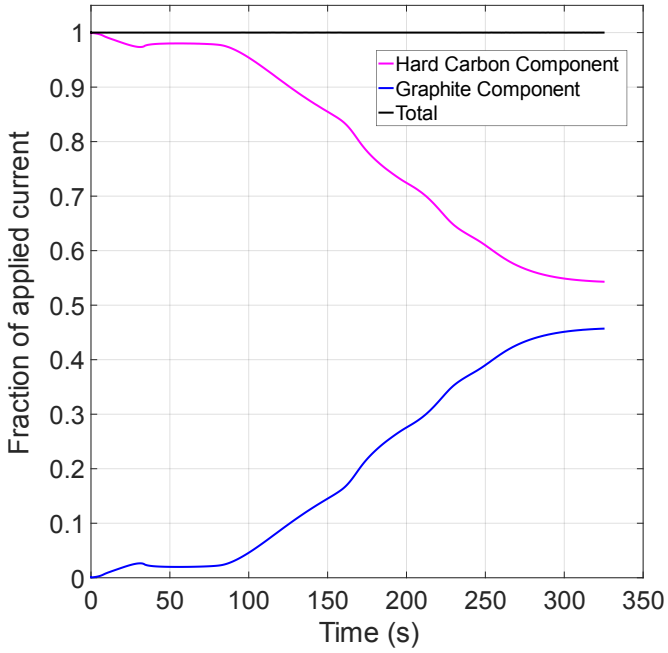

Figure 6.12. Fraction of the applied current contributed by the hard carbon (magenta) and the graphite (blue) components in the Gr-50 anode during 4C charging. The black curve represents the summation of the two components.

6.1.7 Energy density retention during long-term fast-charge cycling

To evaluate long-term cycling performance and energy density retention, pouch cells were cycled at 4C and 6C charge rates for 500 cycles. To measure the specific energy (gravimetric energy density) of the pouch cells, periodic capacity checks were performed after every 50 fast-charge cycles. In each capacity check, pouch cells were charged/discharged at a C/3 rate between 2.7-4.2 V to measure the capacity, voltage, and energy. **Figure 6.13** shows the stack specific energy of the pouch cells before fast-charge cycling and after 50, 200, and 500 cycles of fast charging. The stack specific energy accounts for the mass of all cell components except the pouch bag, excess electrolyte, and tab extensions. Stack specific energy is used because it is reduces dependency on the total cell capacity.[178] As shown in **Figure 6.13**, the graphite, Gr-75, Gr-50, Gr-25, and hard carbon cells have an initial stack specific energy of 202, 196, 180, 161, and 142 Wh/kg, respectively.

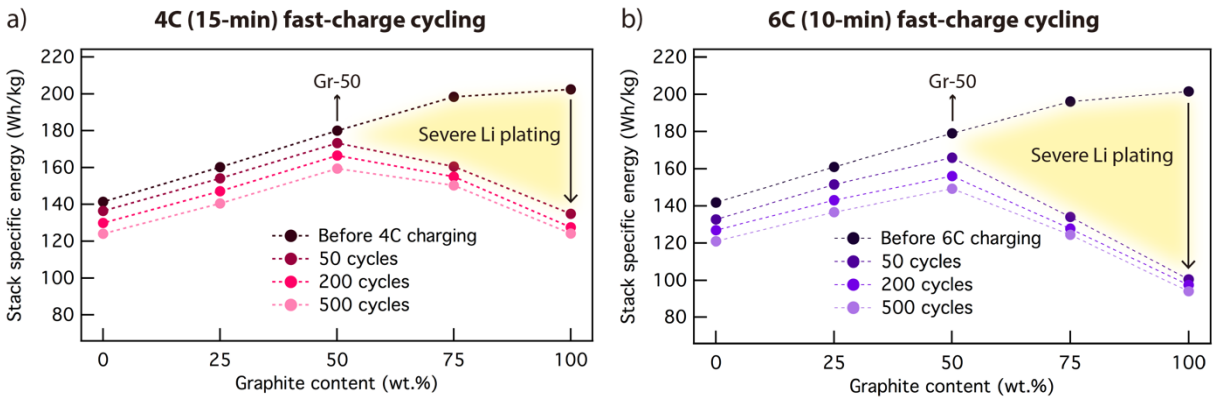

Figure 6.13. Stack specific energy vs. graphite content during (a) 4C (15-min) and (b) 6C (10-min) long-term fast-charge cycling. Specific energy before cycling and after 50, 200, and 500 cycles of fast charging is shown for the pouch cells with varying graphite content. Cell specific energy was measured at C/3 charge/discharge rates periodically throughout the fast-charging cycling.

Due to Li plating during fast charging, the specific energy of the graphite and Gr-75 cells plunge to 135 Wh/kg and 160 Wh/kg after only 50 cycles of 4C charging (**Figure 6.13a**). The specific energy loss is even more dramatic during 6C charging, as the graphite and Gr-75 cells maintain only 100 Wh/kg and 134 Wh/kg after 50 cycles (**Figure 6.13b**). In contrast, the Gr-50, Gr-25, and hard carbon cells demonstrate stable cycling at both 4C and 6C charge rates with minimal loss in specific energy. Among all 5 types of pouch cells, the Gr-50 cells maintain the highest specific energy throughout the 500 cycles of fast-charge cycling at both 4C and 6C charge rates.

It is therefore concluded that although high-specific-energy (> 200 Wh/kg) Li-ion batteries can be achieved using graphite anodes, significant Li loss upon fast charging quickly reduces the available energy density. Compared to the initial specific energy, the energy retention of the graphite cells is only 61% and 48% after 500 cycles of 4C and 6C charging, as shown in **Table 6.1-6.2**. In contrast, by rationally tuning the blend ratio of graphite/hard carbon in the hybrid anodes, the Gr-50 cells can achieve an initial specific energy of 180 Wh/kg, while maintaining an energy retention as high as 87% and 82% after 500 cycles of 4C and 6C fast-charge cycling (**Table 6.1-6.2**). Therefore, while the Gr-50 hybrid cells show 10% lower initial specific energy compared to graphite cells, the remaining specific energy after 500 cycles of fast charging is 27% larger in the hybrid cell at 4C and 53% larger at 6C (**Table 6.1-6.2**). This demonstrates that the hybrid anode strategy is effective in overcoming energy and power density tradeoffs in Li-ion batteries.

4C fast charging	Initial (Wh/kg)	After 500 cycles (Wh/kg)	Energy retention (%)
Graphite	202	124	61%
Gr-50	180	157	87%
Improvement (%)	-10%	+27%	

Table 6.1. Stack specific energy retention and improvement between the graphite and Gr-50 cells during 4C fast-charge cycling.

6C fast charging	Initial (Wh/kg)	After 500 cycles (Wh/kg)	Energy retention (%)
Graphite	202	97	48%
Gr-50	180	148	82%
Improvement (%)	-10%	+53%	

Table 6.2. Stack specific energy retention and improvement between the graphite and Gr-50 cells during 6C fast-charge cycling.

6.2 Conclusions

This work demonstrates hybrid anodes fabricated by mixing graphite and hard carbon to achieve fast-charging Li-ion batteries with high energy densities (>180 Wh/kg), using industrially relevant multi-layer pouch cells (> 1 Ah) and electrode capacity loadings (3 mAh/cm^2). By tuning the blend ratio of graphite/hard carbon, it is shown that hybrid anodes with improved current homogeneity and reduced Li plating during fast charging can be achieved, while maintaining sufficiently high energy densities. For a 3 mAh/cm^2 anode loading under 4C-6C charging conditions, our analysis indicates that the 50/50 graphite/hard carbon blend ratio provides the maximum performance within the set of ratios tested. With the Gr-50 anode, we have demonstrated pouch cells with 87% and 82% specific energy retention after 500 cycles of 4C and 6C fast-charge cycling, compared to 61% and 48% for cells using graphite anodes under the same conditions. In addition, while the Gr-50 cells show 10% lower initial specific energy compared to the graphite cells, the remaining specific energy after 500 cycles of fast charging is 27% larger at 4C and 53% larger at 6C. Therefore, the hybrid anode design significantly reduces tradeoffs between energy and power density.

Systematic electrochemical analysis was performed to demonstrate the efficacy of the hybrid anode design. Continuum-scale electrochemical simulations identified the origin of the enhanced fast-charge performance to be the improved homogeneity in reaction current distribution throughout the hybrid anode volume. Moreover, synchrotron tomography showed that while the graphite and hard carbon are uniformly blended throughout the bulk of the electrode, subtle differences in the local microstructures can be observed, which may further impact the local current density variation within the electrodes.

Importantly, standard mixing, roll-to-roll slurry casting, and calendaring was performed here to fabricate the hybrid anodes, demonstrating direct compatibility with existing Li-ion manufacturing. This is a significant advantage of the hybrid anode approach, as it does not require developing alternative processing methods or device architectures, which could result additional manufacturing costs and/or reduce throughput. By overcoming energy and power density tradeoffs in Li-ion batteries, the hybrid anode design provides a pathway toward efficient fast-charging of high-energy-density EV-scale batteries.

6.3 Materials and Methods

6.3.1 Electrode fabrication

Electrodes were prepared using a pilot-scale roll-to-roll processing facility at the University of Michigan Battery Lab. Battery-grade graphite (Superior Graphite) and hard carbon (Pred Materials International) were used as the active anode materials. Active materials were first mixed with CMC/SBR binder in a weight ratio of 94/3/3 in deionized water to make a homogeneous slurry. The resulting anode slurry was then casted onto 10 μm copper foils (Fukuda). The specific capacity of the graphite and hard carbon used in this work was measured (at a C/10 rate) to be 335 mAh/g and 275 mAh/g, respectively. Therefore, areal mass loadings were slightly adjusted for hybrid anodes with varying graphite/hard carbon blend ratio to obtain the same areal capacity loading of ~3 mAh/cm^2. After casting, the anodes were dried and calendered to a porosity of 31-33%. NMC-532 (Toda America) was used as the cathode material. The cathode formulation was 92 wt.% NMC-532, 4 wt.% C65 conductive additive, and 4 wt.% PVDF binder. The cathode slurry was casted onto 15 μm aluminum foils (Targray) with a total areal mass loading of 16.58 mg/cm^2 and calendered to a porosity of 34%.

6.3.2 Pouch cell assembly

Fabricated electrodes were first baked in vacuum ovens at 90^{o}C overnight to remove any residual moisture prior to pouch cell assembly. Pouch cells were assembled in a dry room (< -50 ^{o}C dew point) at the University of Michigan Battery Lab. Each pouch cell was constructed of 4/5 cathode/anode double-sided electrodes with 12 µm polyethylene separators (ENTEK). A N/P ratio of 1.16 was fixed for all five types of cells. The electrode area was ~70 cm^2 on each side. 1M $LiPF_6$ in 3/7 EC/EMC with 2% VC additive (SoulBrain MI) was used as the electrolyte. After electrolyte filling, cells were vacuum sealed and allowed to rest for 12 hours to ensure full electrolyte infiltration into the electrodes. Subsequently, formation cycles were performed at C/10 rate between 2.7-4.2 voltage window. Afterwards, the cells were transferred back into the dry room, degassed to release gases produced during the formation, and then re-sealed.

6.3.3 Pouch cell testing

Pouch cells were cycled in a temperature-controlled chamber at 30 ^{o}C using a Maccor 4000 series automated test system. To evaluate the fast-charge capability of the hybrid anodes, a CC-CV charging protocol with a charging time cutoff was used (15 min for 4C and 10 min for 6C). For 4C (15-min) fast charging, pouch cells were first charged at a constant current (CC) of 4C rate until reaching an upper voltage cutoff of 4.2V, and then charged at constant voltage (CV) until a total charging time (CC+CV) of 15 minutes was reached. For 6C (10-min) fast charging, the applied CC current was 6C rate and the total charging time was limited to 10 minutes. Throughout the course of cycling, the discharge rate was fixed at 1C with a voltage cutoff of 2.7 V without any CV hold.

It is noted that due to the varying ICE values, the hybrid pouch cells have different cell capacities after formation cycles. This can make the rate performance comparison difficult since the applied current (in C-rate) is proportional to the cell capacity. To facilitate a more direct comparison between all 5 types of pouch cells, here we define the applied current solely based on the capacity of the graphite cell after formation (1.3 Ah). In other words, during 4C and 6C fast charging, a current of 5.2 A and 7.8 A was applied on all pouch cells. We believe that this is a

valid comparison since all the anodes have the same areal capacity loading (3 mAh/cm^2). Therefore, the applied current density is the same with respect to the anodes during fast charging.

6.3.4 Three-electrode measurements

Three-electrode measurements were performed using a commercial electrochemical test cell (ECC-PAT-Core, EL-CELL). In this setup, the hybrid anodes were used as the working electrode and Li metal was used as the counter electrode. In addition, a ring-shaped Li metal was used a reference electrode to measure the potential of the hybrid anodes with respect to Li/Li$^+$. Electrochemical data was collected using a BioLogic VSP potentiostat (Bio-Logic USA), which can measure the potential of the working and counter electrodes vs. the reference electrode potential.

6.3.5 SEM characterization

Post-mortem SEM analysis was performed to characterize Li plating during fast-charge cycling. Cycled pouch cells were first fully discharged to 2.7V and then transferred into an argon-filled glovebox (MBraun). Electrodes were carefully collected from the pouches and rinsed thoroughly with DMC several times to remove any electrolyte residues. The cleaned electrodes were subsequently dried and stored in the glovebox antechamber under vacuum before transferred into SEM for imaging. SEM analysis was performed using a Tescan MIRA3 FEG SEM at the Michigan Center for Materials Characterization.

Chapter 7

Conclusions and Future Work

7.1 Conclusions

The work presented in this thesis has made several contributions to the battery community by first developing new fundamental understanding, and subsequently applying the gained knowledge to design novel electrode architectures for improved battery performance.

Chapter 3 demonstrated that voltage profiles of Li-metal batteries during extended cycling can be correlated to the accumulation of dead Li on the electrode surface in both half cells and full cells. Due to the poor reversibility of Li metal, dead Li continuously accumulates during cycling and creates a tortuous diffusion pathway that affects concentration gradients and impedes mass transport. These mass transport limitations drive the transition in voltage shape from peaking to arcing, along with increasing overpotential. GITT analysis revealed that the underlying reaction kinetics (dendrite growth and surface pitting) still occurs even when the shape of the voltage trace is dominated by mass transport limitations. In addition, the GITT voltage profile showed a significantly lower total overpotential compared to the uninterrupted voltage trace, indicating that mass transport is the reason for the increasing cell polarization at later cycles. Finally, dead Li accumulation was shown to directly cause capacity fade in full cells containing Li metal anodes. The increasing overpotential due to mass transport causes cells to reach cut-off voltages prior to the targeted cathode composition during charge/discharge. Cycling between limited voltage ranges hence results in a perceived capacity loss. This work underscores the need for reduced dead Li formation to enable long-term cycling of Li metal batteries.

Chapter 4 demonstrated a bottom-up fabrication process for a current collector composed of highly uniform and vertically aligned Cu pillars. It was shown that the geometry of the 3-D current collector has a significant impact on the Li morphology upon Li plating/stripping, which affects

the CE and cycle life. This emphasizes a critical need to rationally control the geometric parameters of 3-D current collectors in order to achieve a desirable Li morphology. Cu pillar arrays of 2 μm pillar diameter and an average pore spacing of 5 μm exhibit compact and uniform Li deposition and display improved performance compared to both larger and smaller diameters and spacing. This is attributed to a number of factors, including local current density, electric field focusing, ionic diffusion, and separator interactions, which in turn affect the nucleation density, average growth size and shape of deposits, and dead Li formation. An ultrathin layer (50 nm) of ALD ZnO was further applied to the Cu pillar arrays to tune the interfacial chemistry, which appeared to facilitate more homogeneous Li nucleation, resulting in larger and more densely-packed Li morphologies, as well as more reversible Li plating/stripping. This core-shell pillar architecture allows for the effects of geometry and surface chemistry to be decoupled and individually controlled to optimize the electrode performance in a synergistic manner. With the synergistic effect of the 3-D geometry and surface modification, the ALD coated 2 μm pillar arrays exhibited a record-high CE up to 99.4% under current densities of 1 mA/cm^2 and 2 mA/cm^2 and 99.5% under a current density of 0.5 mA/cm^2.

Chapter 5 employed a laser-patterning process to fabricate 3-D graphite anode architectures to achieve efficient fast-charging of Li-ion batteries. High-loading graphite anodes (> 3 mAh/cm^2) and an industrially relevant cell format (> 2 Ah pouch cells) were used to show the feasibility of using HOLE anodes for high-energy-density Li-ion cells. The through-thickness, laser-ablated pore channels facilitate Li-ion transport into the bulk electrode, thus reducing concentration gradients during fast charging. Consequently, a higher accessible capacity and low propensity for Li plating was achieved. A detailed analysis of the electrochemical response and electrode morphology, coupled with continuum-scale modeling, was performed to provide insight into the mechanism of improved transport. Using the HOLE architecture, we observed > 97% and > 93% capacity retention over 100 cycles of 4C and 6C fast-charge cycling respectively, compared to 69% and 59% for unpatterned electrodes. After 600 cycles of fast-charging, the capacity retention of the HOLE cells remained as high as 91% at 4C and 86% at 6C charge rates. Moreover, the HOLE design allows cells to access > 90% of the total cell capacity during fast charging. The presented performances in this work address both the DOE and USABC goals for fast-charging batteries.

Chapter 6 demonstrated a hybrid anode design for Li-ion batteries to address material and energy/power tradeoffs. Graphite exhibits high energy density but suffers from an inhomogeneous reaction current and irreversible Li plating when subjected to fast charging. On the other hand, hard carbon displays enhanced rate performance but limited energy density. By mixing graphite and hard carbon and tuning the associated blend ratio, it was shown that the use of hybrid anodes can lead to reduced Li plating during fast charging, while maintaining sufficiently high energy densities. For a 3 mAh/cm^2 anode loading under 4C-6C charging conditions, our analysis indicated that the 50/50 graphite/hard carbon blend ratio exhibits the best performance within the set of ratios tested. Continuum-scale electrochemical simulations identified the origins of the enhanced fast-charge performance, which were attributed to the improved homogeneity in reaction current distribution throughout the hybrid anode volume. With the Gr-50 anode, we demonstrated pouch cells with 87% and 82% specific energy retention after 500 cycles of 4C and 6C cycling, compared to 61% and 48% for cells using graphite anodes under the same fast-charge conditions. In addition, while the Gr-50 cells showed 10% lower initial specific energy compared to the graphite cells, the remaining specific energy after 500 cycles of fast charging was 27% larger at 4C and 53% larger at 6C. By overcoming energy and power density tradeoffs in Li-ion batteries, the hybrid anode design provides a scalable pathway toward efficient fast-charging of high-energy-density EV-scale batteries.

7.2 Future work

While the presented studies have already impacted and led to other work in the field, there are numerous opportunities to expand upon the understanding and results presented in this thesis.

Chapter 3 clearly demonstrated that dead Li accumulation has significant impacts on the voltage, capacity, and failure of Li metal batteries. There are many more scientifically interesting questions to answer on this topic, including:

(1) Can the understanding gained from this work be further applied to interpret voltage profiles of other battery systems containing metallic anodes (ex. sodium-, magnesium-, and zinc-metal batteries), and accurately evaluate the effectiveness of new methods to improve cell performance?

(2) While the dead Li layer has been shown to increase in thickness as cycling progresses, further quantification of the porosity and tortuosity values associated with this interphase and how they evolve dynamically during repeated cycling is of interest. This analysis will provide more accurate input parameters for electrochemical models to simulate reaction kinetics and mass transport, thereby predicting the cycle life and failure of Li metal batteries.

(3) The formation of dead Li has been attributed to physical and/or electrical isolation of metallic Li occurring during cycling. It will be valuable for future research efforts to develop the capability to pinpoint the failure points at nanoscale interfaces and identify their structural and/or chemical origins. This may entail employing advanced in-situ and/or *operando* characterization techniques (ex. X-ray tomography, atomic force microscopy, TEM, neutron imaging, etc.) to develop further insight into the coupled relations among electrochemistry, interfacial properties, and microstructural evolution of Li metal anodes.

Chapter 4 demonstrated that with the synergistic effect of the 3-D geometry and surface modification, the ALD-coated Cu pillar arrays achieved a record-high CE up to 99.5%. Nevertheless, to achieve commercially relevant performance metrics, the CE needs to be > 99.9%. Therefore, developing strategies to address the remaining ~ 0.5% is critical. Since the amount of dead Li has been significantly reduced using the ALD-coated Cu pillar arrays, the key to further improve CE may be to address the irreversible Li loss due to SEI formation. Particularly, the thickness, decomposition products, and stability of the SEI layer on Li surface become crucial. Recently, several research efforts have successfully developed advanced electrolytes that can achieve a ultrathin, compact, and stable SEI layer on Li metal surface.[59,179,180] Combining 3-D electrode architectures with newly developed electrolytes is promising and likely to further boost the CE.

In addition to CE, several other requirements still need to be met in order to make Li-metal batteries competitive and outperform state-of-the-art Li-ion technology. U.S. DOE has recently laid out ARPA-E IONICS goals, which target plating Li at > 3 mA/cm^2 current density and > 3 mAh/cm^2 per-cycle capacity, and passing > 80% of the total Li inventory per cycle.[123,181] As a comparison, the work presented in Chapter 4 demonstrated cycling at up to 2 mA/cm^2 and 2 mAh/cm^2, and passing 50% of the total Li in the cell. Furthermore, unlike coin cells used in lab testing, the cell parameters in a realistic commercial cell (ex. pouch cells) need to be restricted in order to deliver high energy density. These parameters include high electrode loading, thin Li

metal, and lean electrolyte loading.[182,183] Thus, there is a need in the Li-metal battery community to bridge the gap between lab-scale coin cells to practical large-format batteries.

Chapter 5 demonstrated efficient fast charging using laser-patterned graphite anodes. Near-term future work will be further demonstration of the effectiveness of the 3-D architecture on fast-charging other anode/cathode materials and battery systems where Li-ion mass transport through porous/tortuous electrodes is the rate limiting step. This includes other state-of-the-art anodes (ex. silicon/carbon composites) and cathodes (ex. NMC 811), as well as electrodes with even higher loadings (> 3 mAh/cm^2). The presented laser patterning approach is compatible with current Li-ion battery manufacturing and can be integrated into existing roll-to-roll manufacturing lines. In order to realize this integration, industrially relevant processing speed (> 10 m/min) needs to be achieved.

Chapter 6 demonstrated hybrid anodes with uniform mixtures of graphite and hard carbon to simultaneously achieve high energy density and fast charging. Continuum-scale electrochemical simulations identified the origin of the enhanced fast-charge performance to be the improved homogeneity in reaction current distribution throughout the hybrid anode volume. In the future, detailed modeling studies need to be performed to decouple the individual effects of OCV profile shape, solid-state diffusivity, particle size, and tortuosity on the improved power performance of the hybrid anodes.

Enabling fast-charging of Li-ion batteries remains an area of significant research and commercialization interest. The presented work in Chapter 5 and 6 essentially showed two different approaches to maximize the accessible capacity of anodes at potential values more positive than 0 V vs. Li/Li$^+$. This is preferred, as Li plating on graphite is the main failure mechanism for fast-charging of Li-ion batteries. However, scientifically important questions remain to be asked and answered, particularly at regions where the anode potential is < 0 V vs. Li/Li$^+$. These questions include:

(1) Where does Li plating occur on graphite anode surface and can it be correlated to localized surface inhomogeneities, such as chemical, microstructural, or electrochemical features?

(2) Are there electrochemical signatures in the voltage trace associated with metallic Li nucleation and growth on graphite surface during fast charging?

(3) What is the reversibility of Li plating on graphite? To what extent can the plated Li be recovered during cycling, including charge, rest, and discharge?

(4) How does the dead Li formation occur on the graphite surface and is this process more or less reversible than the dead Li formation on Li metal anodes?

Future research opportunities using *operando* optical microscopy can enable time synchronization of voltage traces and Li plating during fast charging and provide more detailed mechanistic understanding of the interaction between plated Li and graphite. In addition, developing a 3-electrode measurement capability in representative cell formats, such as pouch cells, is highly valuable and will allow for monitoring the dynamic evolution of anode/cathode voltages during fast-charge cycling. An improved fundamental understanding of the Li plating process on graphite surface will in turn enable researchers to design novel strategies (such as interface modification, electrolyte development, advanced charging protocols) to realize reversible Li plating in Li-ion batteries.

In summary, there are many exciting opportunities moving forward from the work included in this thesis. This presented work could aid in the development of not only the state-of-the-art Li-ion batteries, but also next-generation battery systems using Li metal anodes.

Bibliography

[1] S. Chu, A. Majumdar, *Nature* **2012**, *488*, 294.
[2] *https://www.eia.gov/energyexplained/us-energy-facts* **2020**.
[3] A. Hoekstra, *Joule* **2019**, *3*, 1412.
[4] M. Armand, J.-M. Tarascon, *Nature* **2008**, *451*, 652.
[5] N. Nitta, F. Wu, J. T. Lee, G. Yushin, *Mater. Today* **2015**, *18*, 252.
[6] *https://www.energy.gov/sites/prod/files/2014/02/f8/eveverywhere_blueprint.pdf* **2014**.
[7] USABC Goals for Low-Cost and Fast-Charge Advanced Batteries for EVs, **2020**.
[8] K.-H. Chen, K. N. Wood, E. Kazyak, W. S. LePage, A. L. Davis, A. J. Sanchez, N. P. Dasgupta, *J. Mater. Chem. A* **2017**, *5*, 11671.
[9] K.-H. Chen, A. J. Sanchez, E. Kazyak, A. L. Davis, N. P. Dasgupta, *Adv. Energy Mater.* **2019**, *9*, 1802534.
[10] K. Chen, M. J. Namkoong, V. Goel, C. Yang, S. Kazemiabnavi, S. M. Mortuza, E. Kazyak, J. Mazumder, K. Thornton, J. Sakamoto, N. P. Dasgupta, *J. Power Sources* **2020**, *471*, 228475.
[11] *https://www.nobelprize.org/prizes/chemistry/2019/press-release/* **2019**.
[12] Y. Nishi, *J. Power Sources* **2001**, *100*, 101.
[13] M. Winter, B. Barnett, K. Xu, *Chem. Rev.* **2018**, *118*, 11433.
[14] Y. Guo, R. B. Smith, Z. Yu, D. K. Efetov, J. Wang, P. Kim, M. Z. Bazant, L. E. Brus, *J. Phys. Chem. Lett.* **2016**, *7*, 2151.
[15] M. S. Dresselhaus, G. Dresselhaus, *Adv. Phys.* **2002**, *51*, 1.
[16] J. R. Dahn, *Phys. Rev. B* **1991**, *44*, 9170.
[17] X. Zeng, M. Li, D. Abd El-Hady, W. Alshitari, A. S. Al-Bogami, J. Lu, K. Amine, *Adv. Energy Mater.* **2019**, *9*, 1900161.
[18] C. Mao, M. Wood, L. David, S. J. An, Y. Sheng, Z. Du, H. M. Meyer, R. E. Ruther, D. L. Wood, *J. Electrochem. Soc.* **2018**, *165*, A1837.
[19] G. E. Blomgren, *J. Electrochem. Soc.* **2017**, *164*, A5019.
[20] Y. Ding, Z. P. Cano, A. Yu, J. Lu, Z. Chen, *Electrochem. Energy Rev.* **2019**, *2*, 1.
[21] G. Zheng, W. Zhang, X. Huang, *ChemistrySelect* **2018**, *3*, 11573.
[22] A. Manthiram, *Nat. Commun.* **2020**, *11*, 1.
[23] J. Choi, A. Manthiram, *J. Electrochem. Soc.* **2005**, *152*, A1714.
[24] S. J. An, J. Li, D. Mohanty, C. Daniel, B. J. Polzin, J. R. Croy, S. E. Trask, D. L. Wood, *J. Electrochem. Soc.* **2017**, *164*, A1195.
[25] K. Xu, *Chem. Rev.* **2004**, *104*, 4303.
[26] E. R. Logan, J. R. Dahn, *Trends Chem.* **2020**, *2*, 354.
[27] T. Liu, L. Lin, X. Bi, L. Tian, K. Yang, J. Liu, M. Li, Z. Chen, J. Lu, K. Amine, K. Xu, F. Pan, *Nat. Nanotechnol.* **2018**, *14*, 50.
[28] J. Kasnatscheew, M. Evertz, B. Streipert, R. Wagner, R. Klöpsch, B. Vortmann, H. Hahn, S. Nowak, M. Amereller, A. C. Gentschev, P. Lamp, M. Winter, *Phys. Chem. Chem. Phys.* **2016**, *18*, 3956.

[29] M.-T. Fonseca Rodrigues, V. A. Maroni, D. J. Gosztola, K. P. C. Yao, K. Kalaga, I. A. Shkrob, D. P. Abraham, *ACS Appl. Energy Mater.* **2019**, *2*, 873.
[30] S. J. An, J. Li, C. Daniel, D. Mohanty, S. Nagpure, D. L. Wood, *Carbon N. Y.* **2016**, *105*, 52.
[31] A. Yoshino, in *Lithium-Ion Batter.*, Elsevier, **2014**, pp. 1–20.
[32] S. E. Trask, Y. Li, J. J. Kubal, M. Bettge, B. J. Polzin, Y. Zhu, A. N. Jansen, D. P. Abraham, *J. Power Sources* **2014**, *259*, 233.
[33] P. V. Braun, J. B. Cook, *ACS Nano* **2018**, *12*, 3060.
[34] *Magn. Tape Prod. Coat. Tech. Coat. Tech.* **1965**.
[35] M. Ebner, D. W. Chung, R. E. García, V. Wood, *Adv. Energy Mater.* **2014**, *4*, 1.
[36] B. Vijayaraghavan, D. R. Ely, Y.-M. Chiang, R. García-García, R. E. García, *J. Electrochem. Soc.* **2012**, *159*, A548.
[37] I. V. Thorat, D. E. Stephenson, N. A. Zacharias, K. Zaghib, J. N. Harb, D. R. Wheeler, *J. Power Sources* **2009**, *188*, 592.
[38] D. Kehrwald, P. R. Shearing, N. P. Brandon, P. K. Sinha, S. J. Harris, *J. Electrochem. Soc.* **2011**, *158*, A1393.
[39] K. G. Gallagher, S. Goebel, T. Greszler, M. Mathias, W. Oelerich, D. Eroglu, V. Srinivasan, *Energy Environ. Sci.* **2014**, *7*, 1555.
[40] P. G. Bruce, L. J. Hardwick, K. M. Abraham, *MRS Bull.* **2011**, *36*, 506.
[41] X.-B. Cheng, J.-Q. Huang, Q. Zhang, *J. Electrochem. Soc.* **2018**, *165*, A6058.
[42] K. N. Wood, E. Kazyak, A. F. Chadwick, K.-H. Chen, J.-G. Zhang, K. Thornton, N. P. Dasgupta, *ACS Cent. Sci.* **2016**, *2*, 790.
[43] K. N. Wood, M. Noked, N. P. Dasgupta, *ACS Energy Lett.* **2017**, *2*, 664.
[44] G. Bieker, M. Winter, P. Bieker, *Phys. Chem. Chem. Phys.* **2015**, *17*, 8670.
[45] D. Aurbach, E. Zinigrad, H. Teller, P. Dan, *J. Electrochem. Soc.* **2000**, *147*, 1274.
[46] D. Aurbach, *J. Power Sources* **2000**, *89*, 206.
[47] A. J. Sanchez, E. Kazyak, Y. Chen, K. H. Chen, E. R. Pattison, N. P. Dasgupta, *ACS Energy Lett.* **2020**, *5*, 994.
[48] M. Rosso, C. Brissot, A. Teyssot, M. Dollé, L. Sannier, J. M. Tarascon, R. Bouchet, S. Lascaud, *Electrochim. Acta* **2006**, *51*, 5334.
[49] D. Aurbach, E. Zinigrad, Y. Cohen, H. Teller, *Solid State Ionics* **2002**, *148*, 405.
[50] K. Kerman, A. Luntz, V. Viswanathan, Y.-M. M. Chiang, Z. Chen, *J. Electrochem. Soc.* **2017**, *164*, A1731.
[51] J. Steiger, D. Kramer, R. Mönig, *J. Power Sources* **2014**, *261*, 112.
[52] H. J. Chang, A. J. Ilott, N. M. Trease, M. Mohammadi, A. Jerschow, C. P. Grey, *J. Am. Chem. Soc.* **2015**, *137*, 15209.
[53] J. Zheng, P. Yan, D. H. Mei, M. H. Engelhard, S. S. Cartmell, B. J. Polzin, C. M. Wang, J. G. Zhang, W. Xu, *Adv. Energy Mater.* **2016**, *6*, 1502151.
[54] C. Fang, J. Li, M. Zhang, Y. Zhang, F. Yang, J. Z. Lee, M. H. Lee, J. Alvarado, M. A. Schroeder, Y. Yang, B. Lu, N. Williams, M. Ceja, L. Yang, M. Cai, J. Gu, K. Xu, X. Wang, Y. S. Meng, *Nature* **2019**, *572*, 511.
[55] J. Steiger, G. Richter, M. Wenk, D. Kramer, R. Mönig, *Electrochem. commun.* **2015**, *50*, 11.
[56] J. Steiger, D. Kramer, R. Mönig, *Electrochim. Acta* **2014**, *136*, 529.
[57] I. Yoshimatsu, T. Hirai, J. Yamaki, *J. Electrochem. Soc.* **1988**, *135*, 2422.
[58] Z. Li, J. Huang, B. Yann Liaw, V. Metzler, J. Zhang, *J. Power Sources* **2014**, *254*, 168.

[59] S. Chen, J. Zheng, D. Mei, K. S. Han, M. H. Engelhard, W. Zhao, W. Xu, J. Liu, J. G. Zhang, *Adv. Mater.* **2018**, *1706102*, 1.
[60] J. Qian, W. A. Henderson, W. Xu, P. Bhattacharya, M. Engelhard, O. Borodin, J.-G. Zhang, *Nat. Commun.* **2015**, *6*, 6362.
[61] Y. Yamada, A. Yamada, *J. Electrochem. Soc.* **2015**, *162*, A2406.
[62] E. Markevich, G. Salitra, D. Aurbach, *ACS Energy Lett.* **2017**, *2*, 1337.
[63] E. Kazyak, K. N. Wood, N. P. Dasgupta, *Chem. Mater.* **2015**, *27*, 6457.
[64] A. C. Kozen, C. F. Lin, A. J. Pearse, M. A. Schroeder, X. Han, L. Hu, S. B. Lee, G. W. Rubloff, M. Noked, *ACS Nano* **2015**, *9*, 5884.
[65] L. Chen, K.-S. Chen, X. Chen, G. Ramirez, Z. Huang, N. R. Geise, H.-G. Steinrück, B. L. Fisher, R. Shahbazian-Yassar, M. F. Toney, M. C. Hersam, J. W. Elam, *ACS Appl. Mater. Interfaces* **2018**, *10*, 26972.
[66] L. Chen, J. G. Connell, A. Nie, Z. Huang, K. R. Zavadil, K. C. Klavetter, Y. Yuan, S. Sharifi-Asl, R. Shahbazian-Yassar, J. A. Libera, A. U. Mane, J. W. Elam, *J. Mater. Chem. A* **2017**, *5*, 12297.
[67] C. F. Lin, A. C. Kozen, M. Noked, C. Liu, G. W. Rubloff, *Adv. Mater. Interfaces* **2016**, *3*, 1.
[68] Y. Liu, Y. K. Tzeng, D. Lin, A. Pei, H. Lu, N. A. Melosh, Z. X. Shen, S. Chu, Y. Cui, *Joule* **2018**, 1.
[69] L. Liu, Y. X. Yin, J. Y. Li, N. W. Li, X. X. Zeng, H. Ye, Y. G. Guo, L. J. Wan, *Joule* **2017**, *1*, 563.
[70] C.-P. Yang, Y.-X. Yin, S.-F. Zhang, N.-W. Li, Y.-G. Guo, *Nat. Commun.* **2015**, *6*, 8058.
[71] S. Jin, Y. Jiang, H. Ji, Y. Yu, *Adv. Mater.* **2018**, *30*, 1802014.
[72] Q. Li, S. Zhu, Y. Lu, *Adv. Funct. Mater.* **2017**, 1606422.
[73] Q. Yun, Y.-B. He, W. Lv, Y. Zhao, B. Li, F. Kang, Q.-H. Yang, *Adv. Mater.* **2016**, *28*, 6932.
[74] Z. Liang, D. Lin, J. Zhao, Z. Lu, Y. Liu, C. Liu, Y. Lu, H. Wang, K. Yan, X. Tao, Y. Cui, *Proc. Natl. Acad. Sci.* **2016**, *113*, 2862.
[75] D. Lin, Y. Liu, Z. Liang, H.-W. W. Lee, J. Sun, H. Wang, K. Yan, J. Xie, Y. Cui, *Nat. Nanotechnol.* **2016**, *11*, 626.
[76] Y. Liu, D. Lin, Z. Liang, J. Zhao, K. Yan, Y. Cui, *Nat. Commun.* **2016**, *7*, 10992.
[77] J. Heine, S. Krüger, C. Hartnig, U. Wietelmann, M. Winter, P. Bieker, *Adv. Energy Mater.* **2014**, *4*, 1300815.
[78] S. Ahmed, I. Bloom, A. N. Jansen, T. Tanim, E. J. Dufek, A. Pesaran, A. Burnham, R. B. Carlson, F. Dias, K. Hardy, M. Keyser, C. Kreuzer, A. Markel, A. Meintz, C. Michelbacher, M. Mohanpurkar, P. A. Nelson, D. C. Robertson, D. Scoffield, M. Shirk, T. Stephens, R. Vijayagopal, J. Zhang, *J. Power Sources* **2017**, *367*, 250.
[79] K. G. Gallagher, S. E. Trask, C. Bauer, T. Woehrle, S. F. Lux, M. Tschech, P. Lamp, B. J. Polzin, S. Ha, B. Long, Q. Wu, W. Lu, D. W. Dees, A. N. Jansen, *J. Electrochem. Soc.* **2016**, *163*, A138.
[80] J. Billaud, F. Bouville, T. Magrini, C. Villevieille, A. R. Studart, *Nat. Energy* **2016**, *1*, 1.
[81] A. Burnham, E. J. Dufek, T. Stephens, J. Francfort, C. Michelbacher, R. B. Carlson, J. Zhang, R. Vijayagopal, F. Dias, M. Mohanpurkar, D. Scoffield, K. Hardy, M. Shirk, R. Hovsapian, S. Ahmed, I. Bloom, A. N. Jansen, M. Keyser, C. Kreuzer, A. Markel, A. Meintz, A. Pesaran, T. R. Tanim, *J. Power Sources* **2017**, *367*, 237.
[82] A. Meintz, J. Zhang, R. Vijayagopal, C. Kreutzer, S. Ahmed, I. Bloom, A. Burnham, R. B. Carlson, F. Dias, E. J. Dufek, J. Francfort, K. Hardy, A. N. Jansen, M. Keyser, A. Markel,

C. Michelbacher, M. Mohanpurkar, A. Pesaran, D. Scoffield, M. Shirk, T. Stephens, T. Tanim, *J. Power Sources* **2017**, *367*, 216.
[83] Y. Kim, A. Drews, R. Chandrasekaran, T. Miller, J. Sakamoto, *Ionics (Kiel).* **2018**, *24*, 2935.
[84] L. Li, R. M. Erb, J. Wang, J. Wang, Y. Chiang, *Adv. Energy Mater.* **2019**, *9*, 1802472.
[85] V. P. Nemani, S. J. Harris, K. C. Smith, *J. Electrochem. Soc.* **2015**, *162*, A1415.
[86] M. F. Lagadec, R. Zahn, V. Wood, *Nat. Energy* **2019**, *4*, 16.
[87] N. Kim, S. Chae, J. Ma, M. Ko, J. Cho, *Nat. Commun.* **2017**, *8*, 1.
[88] C. Heubner, M. Schneider, A. Michaelis, *Adv. Energy Mater.* **2020**, *10*, 1902523.
[89] D. H. Kim, S. Hwang, J. J. Cho, S. Yu, S. Kim, J. Jeon, K. H. Ahn, C. Lee, H. K. Song, H. Lee, *ACS Energy Lett.* **2019**, *4*, 1265.
[90] T. Waldmann, B. I. Hogg, M. Wohlfahrt-Mehrens, *J. Power Sources* **2018**, *384*, 107.
[91] A. M. Colclasure, A. R. Dunlop, S. E. Trask, B. J. Polzin, A. N. Jansen, K. Smith, *J. Electrochem. Soc.* **2019**, *166*, A1412.
[92] X. G. Yang, T. Liu, Y. Gao, S. Ge, Y. Leng, D. Wang, C.-Y. Y. Wang, *Joule* **2019**, *3*, 3002.
[93] X. G. Yang, C. Y. Wang, *J. Power Sources* **2018**, *402*, 489.
[94] A. S. Mussa, A. Liivat, F. Marzano, M. Klett, B. Philippe, C. Tengstedt, G. Lindbergh, K. Edström, R. W. Lindström, P. Svens, *J. Power Sources* **2019**, *422*, 175.
[95] J. Jones, M. C. Smart, F. C. Krause, B. V Ratnakumar, E. J. Brandon, *ECS Trans.* **2017**, *75*, 1.
[96] X-CEL: eXtreme Fast Charge Quarterly Report, **2019**.
[97] S. Choudhury, R. Mangal, A. Agrawal, L. A. Archer, *Nat. Commun.* **2015**, *6*, 10101.
[98] D. Lu, Y. Shao, T. Lozano, W. D. Bennett, G. L. Graff, B. Polzin, J. Zhang, M. H. Engelhard, N. T. Saenz, W. A. Henderson, P. Bhattacharya, J. Liu, J. Xiao, D. Lv, Y. Shao, T. Lozano, W. D. Bennett, G. L. Graff, B. Polzin, J. Zhang, M. H. Engelhard, N. T. Saenz, W. A. Henderson, P. Bhattacharya, J. Liu, J. Xiao, *Adv. Energy Mater.* **2015**, *5*, 1400993.
[99] B. L. Mehdi, A. Stevens, J. Qian, C. Park, W. Xu, W. A. Henderson, J.-G. Zhang, K. T. Mueller, N. D. Browning, *Sci. Rep.* **2016**, *6*, 34267.
[100] B. L. Mehdi, J. Qian, E. Nasybulin, C. Park, D. A. Welch, R. Faller, H. Mehta, W. A. Henderson, W. Xu, C. M. Wang, J. E. Evans, J. Liu, J. G. Zhang, K. T. Mueller, N. D. Browning, *Nano Lett.* **2015**, *15*, 2168.
[101] A. F. Chadwick, G. Vardar, S. DeWitt, A. E. S. Sleightholme, C. W. Monroe, D. J. Siegel, K. Thornton, *J. Electrochem. Soc.* **2016**, *163*, A1813.
[102] A. J. Bard, L. R. Faulkner, *Electrochemical Methods: Fundamentals and Applications, 2nd Ed.*, **2001**.
[103] C. Brissot, M. Rosso, J. N. Chazalviel, S. Lascaud, *J. Power Sources* **1999**, *81*, 925.
[104] W. Weppner, R. A. Huggins, *J. Electrochem. Soc.* **1977**, *124*, 1569.
[105] Y. Zhu, C. Wang, *J. Phys. Chem. C* **2010**, *114*, 2830.
[106] M. H. Ryou, Y. M. Lee, Y. Lee, M. Winter, P. Bieker, *Adv. Funct. Mater.* **2015**, *25*, 834.
[107] X.-Q. Zhang, X.-B. Cheng, X. Chen, C. Yan, Q. Zhang, *Adv. Funct. Mater.* **2017**, *27*, 1605989.
[108] K. Mizushima, P. Jones, P. Wiseman, J. Goodenough, *Solid State Ionics* **1981**, *3*, 171.
[109] B. Huang, Y. Jang, Y. Chiang, D. R. Sadoway, *J. Appl. Electrochem.* **1998**, *28*, 1365.
[110] G. G. Amatucci, J. M. Tarascon, L. C. Klein, *J. Electrochem. Soc.* **1996**, *143*, 1114.
[111] A. Sharafi, H. M. Meyer, J. Nanda, J. Wolfenstine, J. Sakamoto, *J. Power Sources* **2016**, *302*, 135.

[112] L. Kong, H. J. Peng, J. Q. Huang, Q. Zhang, *Nano Res.* **2017**, *10*, 4027.
[113] S.-H. Wang, Y.-X. Yin, T.-T. Zuo, W. Dong, J.-Y. Li, J.-L. Shi, C.-H. Zhang, N.-W. Li, C.-J. Li, Y.-G. Guo, *Adv. Mater.* **2017**, *29*, 1703729.
[114] C. Yang, Y. Yao, S. He, H. Xie, E. Hitz, L. Hu, *Adv. Mater.* **2017**, *29*, 1.
[115] C. Zhang, W. Lv, G. Zhou, Z. Huang, Y. Zhang, R. Lyu, H. Wu, Q. Yun, F. Kang, Q.-H. Yang, *Adv. Energy Mater.* **2018**, *8*, 1703404.
[116] L.-L. Lu, J. Ge, J.-N. Yang, S.-M. Chen, H.-B. Yao, F. Zhou, S.-H. Yu, *Nano Lett.* **2016**, *16*, 4431.
[117] D. Lin, Y. Liu, A. Pei, Y. Cui, *Nano Res.* **2017**, *2*, 1.
[118] M. T. Barako, S. Roy-Panzer, T. S. English, T. Kodama, M. Asheghi, T. W. Kenny, K. E. Goodson, *ACS Appl. Mater. Interfaces* **2015**, *7*, 19251.
[119] M. Motoyama, Y. Fukunaka, T. Sakka, Y. H. Ogata, S. Kikuchi, *J. Electroanal. Chem.* **2005**, *584*, 84.
[120] P. L. Taberna, S. Mitra, P. Poizot, P. Simon, J.-M. Tarascon, *Nat. Mater.* **2006**, *5*, 567.
[121] A. Pei, G. Zheng, F. Shi, Y. Li, Y. Cui, *Nano Lett.* **2017**, *17*, 1132.
[122] B. D. Adams, J. Zheng, X. Ren, W. Xu, J.-G. Zhang, *Adv. Energy Mater.* **2018**, *8*, 1702097.
[123] P. Albertus, S. Babinec, S. Litzelman, A. Newman, *Nat. Energy* **2017**, *3*, 16.
[124] K. Yan, Z. Lu, H.-W. Lee, F. Xiong, P.-C. Hsu, Y. Li, J. Zhao, S. Chu, Y. Cui, *Nat. Energy* **2016**, *1*, 16010.
[125] L. L. Lu, Y. Zhang, Z. Pan, H. Bin Yao, F. Zhou, S. H. Yu, *Energy Storage Mater.* **2017**, *9*, 31.
[126] S. Liu, X. Xia, Y. Zhong, S. Deng, Z. Yao, L. Zhang, X.-B. B. Cheng, X. Wang, Q. Zhang, J. Tu, *Adv. Energy Mater.* **2017**, *8*, 1702322.
[127] C. Jin, O. Sheng, J. Luo, H. Yuan, C. Fang, W. Zhang, H. Huang, Y. Gan, Y. Xia, C. Liang, J. Zhang, X. Tao, *Nano Energy* **2017**, *37*, 177.
[128] Y. Zhang, W. Luo, C. Wang, Y. Li, C. Chen, J. Song, J. Dai, E. M. Hitz, S. Xu, C. Yang, Y. Wang, L. Hu, *Proc. Natl. Acad. Sci.* **2017**, *114*, 3584.
[129] S. M. George, *Chem. Rev.* **2009**, *110*, 111.
[130] N. P. Dasgupta, H.-B.-R. Lee, S. F. Bent, P. S. Weiss, *Chem. Mater.* **2016**, *28*, 1943.
[131] Y. Zhao, K. Zheng, X. Sun, *Joule* **2018**, *2*, 2583.
[132] X. Meng, X.-Q. Yang, X. Sun, *Adv. Mater.* **2012**, *24*, 3589.
[133] A. Kushima, X. H. Liu, G. Zhu, Z. L. Wang, J. Y. Huang, J. Li, *Nano Lett.* **2011**, *11*, 4535.
[134] H. Asayesh-Ardakani, W. Yao, Y. Yuan, A. Nie, K. Amine, J. Lu, R. Shahbazian-Yassar, *Small Methods* **2017**, *1*, 1700202.
[135] C. Wang, Y. Gong, B. Liu, K. Fu, Y. Yao, E. Hitz, Y. Li, J. Dai, S. Xu, W. Luo, E. D. Wachsman, L. Hu, *Nano Lett.* **2017**, *17*, 565.
[136] X. Shen, D. Mu, S. Chen, R. Huang, F. Wu, *J. Mater. Chem. A* **2014**, *2*, 4309.
[137] X. H. Huang, X. H. Xia, Y. F. Yuan, F. Zhou, *Electrochim. Acta* **2011**, *56*, 4960.
[138] J. S. Sakamoto, B. Dunn, *J. Mater. Chem.* **2002**, *12*, 2859.
[139] C. J. Bae, C. K. Erdonmez, J. W. Halloran, Y. M. Chiang, *Adv. Mater.* **2013**, *25*, 1254.
[140] J. S. Sander, R. M. Erb, L. Li, A. Gurijala, Y. M. Chiang, *Nat. Energy* **2016**, *1*, 1.
[141] J. B. Habedank, J. Kriegler, M. F. Zaeh, *J. Electrochem. Soc.* **2019**, *166*, A3940.
[142] W. Pfleging, *Nanophotonics* **2018**, *7*, 549.
[143] D. Lee, R. Patwa, H. Herfurth, J. Mazumder, *J. Power Sources* **2013**, *240*, 368.
[144] D. Lee, R. Patwa, H. Herfurth, J. Mazumder, *J. Laser Appl.* **2016**, *28*, 022006.
[145] Battery Test Manual For Electric Vehicles, **2015**.

[146] J. Doyle, M., Fuller, T. F., Newman, M. Doyle, T. Fuller, J. Newman, J. Doyle, M., Fuller, T. F., Newman, *J. Electrochem. Soc.* **1993**, *140*, 1526.
[147] D. S. Hall, A. Eldesoky, E. R. Logan, E. M. Tonita, X. Ma, J. R. Dahn, *J. Electrochem. Soc.* **2018**, *165*, A2365.
[148] K. M. Diederichsen, E. J. McShane, B. D. McCloskey, *ACS Energy Lett.* **2017**, *2*, 2563.
[149] K. R. Tallman, B. Zhang, L. Wang, S. Yan, K. Thompson, X. Tong, J. Thieme, A. Kiss, A. C. Marschilok, K. J. Takeuchi, D. C. Bock, E. S. Takeuchi, *ACS Appl. Mater. Interfaces* **2019**, *11*, 46864.
[150] K. Kubota, S. Shimadzu, N. Yabuuchi, S. Tominaka, S. Shiraishi, M. Abreu-Sepulveda, A. Manivannan, K. Gotoh, M. Fukunishi, M. Dahbi, S. Komaba, *Chem. Mater.* **2020**, *32*, 2961.
[151] E. Buiel, J. R. Dahn, *Electrochim. Acta* **1999**, *45*, 121.
[152] D. A. Stevens, J. R. Dahn, *J. Electrochem. Soc.* **2001**, *148*, A803.
[153] E. Irisarri, A. Ponrouch, M. R. Palacin, *J. Electrochem. Soc.* **2015**, *162*, A2476.
[154] T. Horiba, T. Maeshima, T. Matsumura, M. Koseki, J. Arai, Y. Muranaka, *J. Power Sources* **2005**, *146*, 107.
[155] Y. Nishi, *Electrochem. Soc. Interface* **2016**, *25*, 71.
[156] C. Ge, J. Wang, Z. Fan, J. Zhang, Y. Qiao, **2018**, 34682.
[157] Y. G. Lim, J. W. Park, M. S. Park, D. Byun, J. S. Yu, Y. N. Jo, Y. J. Kim, *Bull. Korean Chem. Soc.* **2015**, *36*, 150.
[158] K. J. Kim, T. S. Lee, H. G. Kim, S. H. Lim, S. M. Lee, *Electrochim. Acta* **2014**, *135*, 27.
[159] K. Yanagida, A. Yanai, Y. Kida, A. Funahashi, T. Nohma, I. Yonezu, *J. Electrochem. Soc.* **2002**, *149*, A804.
[160] A. Kinoshita, K. Yanagida, A. Yanai, Y. Kida, A. Funahashi, T. Nohma, I. Yonezu, *J. Power Sources* **2001**, *102*, 283.
[161] R. Schmuch, R. Wagner, G. Hörpel, T. Placke, M. Winter, *Nat. Energy* **2018**, *3*, 267.
[162] S. J. Harris, A. Timmons, D. R. Baker, C. Monroe, *Chem. Phys. Lett.* **2010**, *485*, 265.
[163] Y. Qi, S. J. Harris, *J. Electrochem. Soc.* **2010**, *157*, A741.
[164] V. Wood, *Nat. Rev. Mater.* **2018**, *3*, 293.
[165] S. Müller, J. Eller, M. Ebner, C. Burns, J. Dahn, V. Wood, *J. Electrochem. Soc.* **2018**, *165*, A339.
[166] P. Pietsch, M. Ebner, F. Marone, M. Stampanoni, V. Wood, *Sustain. Energy Fuels* **2018**, *2*, 598.
[167] K. G. Gallagher, D. W. Dees, A. N. Jansen, D. P. Abraham, S.-H. Kang, *J. Electrochem. Soc.* **2012**, *159*, A2029.
[168] H. Zhou, F. Xin, B. Pei, M. S. Whittingham, *ACS Energy Lett.* **2019**, *4*, 1902.
[169] A. M. Colclasure, T. R. Tanim, A. N. Jansen, S. E. Trask, A. R. Dunlop, B. J. Polzin, I. Bloom, D. Robertson, L. R. Flores, M. Evans, E. J. Dufek, K. Smith, *Electrochim. Acta* **2020**, *337*, 135854.
[170] J. S. Newman, C. W. Tobias, *J. Electrochem. Soc.* **1962**, *109*, 1183.
[171] J. Newman, W. Tiedemann, *AIChe J.* **1975**, *21*, 25.
[172] M. Doyle, J. Newman, *J. Power Sources* **1995**, *54*, 46.
[173] M.-T. F. Rodrigues, K. Kalaga, S. E. Trask, D. W. Dees, I. A. Shkrob, D. P. Abraham, *J. Electrochem. Soc.* **2019**, *166*, A996.
[174] Q. Liu, C. Du, B. Shen, P. Zuo, X. Cheng, Y. Ma, G. Yin, Y. Gao, *RSC Adv.* **2016**, *6*, 88683.
[175] D. Tewari, Z. Liu, P. B. Balbuena, P. P. Mukherjee, *J. Phys. Chem. C* **2018**, *122*, 21097.
[176] T. F. Fuller, *J. Electrochem. Soc.* **1994**, *141*, 1.

[177] M. Doyle, T. F. Fuller, J. Newman, *Electrochim. Acta* **1994**, *39*, 2073.
[178] J. E. Harlow, X. Ma, J. Li, E. Logan, Y. Liu, N. Zhang, L. Ma, S. L. Glazier, M. M. E. Cormier, M. Genovese, S. Buteau, A. Cameron, J. E. Stark, J. R. Dahn, *J. Electrochem. Soc.* **2019**, *166*, A3031.
[179] X. Ren, S. Chen, H. Lee, D. Mei, M. H. Engelhard, S. D. Burton, W. Zhao, J. Zheng, Q. Li, M. S. Ding, M. Schroeder, J. Alvarado, K. Xu, Y. S. Meng, J. Liu, J.-G. Zhang, W. Xu, *Chem* **2018**, *4*, 1877.
[180] Y. Yang, D. M. Davies, Y. Yin, O. Borodin, J. Z. Lee, C. Fang, M. Olguin, Y. Zhang, E. S. Sablina, X. Wang, C. S. Rustomji, Y. S. Meng, *Joule* **2019**, 1.
[181] https://arpa-e.energy.gov/technologies/programs/ionics, **2016**.
[182] S. Chen, C. Niu, H. Lee, Q. Li, L. Yu, W. Xu, J.-G. Zhang, E. J. Dufek, M. S. Whittingham, S. Meng, J. Xiao, J. Liu, *Joule* **2019**, 1.
[183] J. Liu, Z. Bao, Y. Cui, E. J. Dufek, J. B. Goodenough, P. Khalifah, Q. Li, B. Y. Liaw, P. Liu, A. Manthiram, Y. S. Meng, V. R. Subramanian, M. F. Toney, V. V. Viswanathan, M. S. Whittingham, J. Xiao, W. Xu, J. Yang, X.-Q. Yang, J.-G. Zhang, *Nat. Energy* **2019**, *4*, 180.